

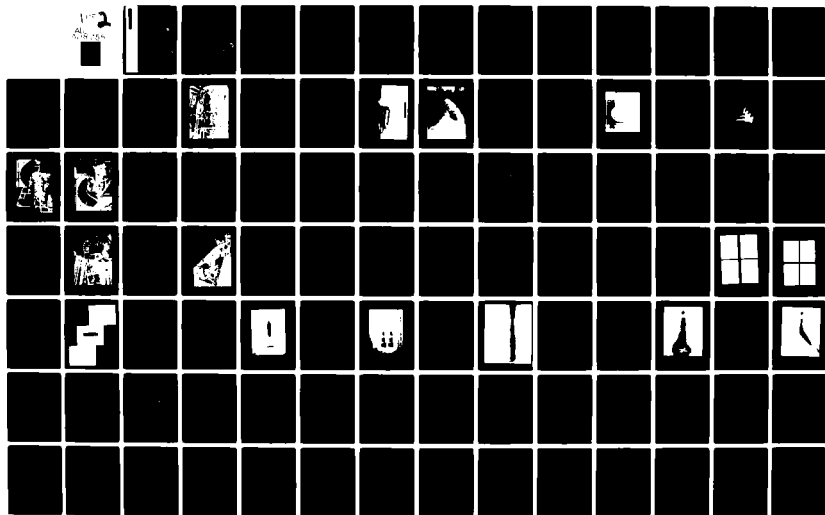
AD-A118 755

MISSION RESEARCH CORP ALBUQUERQUE NM
FX-25 AND FX-100 PROPAGATION EXPERIMENTS.(U)
JUL 82 C A EKDAHL, L A WRIGHT, T P HUGHES
AMRC-R-391

F/G 20/7

UNCLASSIFIED

F49620-81-C-0016
NL



AD A118755

AMRC-R-391

FX-25 and FX-100 PROPAGATION EXPERIMENTS

C. A. Ekdahl
L. A. Wright
T. P. Hughes
B. B. Godfrey

and

W. Bostick (AFWL)

July 1982

DTIC
ELECTED
SEP 1 1982
H

Prepared for:

Air Force Office of Scientific Research
Bolling Air Force Base
Washington, D. C. 20332

Under Contract:

F49620-81-C-0016

Prepared by:

MISSION RESEARCH CORPORATION
1720 Randolph Road S.E.
Albuquerque, New Mexico 87106

DISTRIBUTION STATEMENT A
Approved for public release
Distribution Unlimited

Research sponsored by the Air Force Office of Scientific Research (AFSC), under contract F49620-81-C-0016. The United States Government is authorized to reproduce and distribute reprints for governmental purposes notwithstanding any copyright notation herein.

This manuscript is submitted for publication with the understanding that the United States Government is authorized to reproduce and distribute reprints for governmental purposes.

Original contains color
plates: All DTIC reproductions
will be in black and
white

82 08 30 041

SECURITY CLASSIFICATION OF THIS PAGE (When Data Entered)

REPORT DOCUMENTATION PAGE		READ INSTRUCTIONS BEFORE COMPLETING FORM
1. REPORT NUMBER	2. GOVT ACCESSION NO. AD- A118755	3. RECIPIENT'S CATALOG NUMBER
4. TITLE (and Subtitle) FX-25 and FX-100 PROPAGATION EXPERIMENTS		5. TYPE OF REPORT & PERIOD COVERED Summary of Annual Report
7. AUTHOR(s) C. A. Ekdahl, L. A. Wright, T. P. Hughes, and B. B. Godfrey		6. PERFORMING ORG. REPORT NUMBER AMRC-R-391
9. PERFORMING ORGANIZATION NAME AND ADDRESS Air Force Office of Scientific Research Bolling Air Force Base Washington, DC 20332		8. CONTRACT OR GRANT NUMBER(s) F49620-81-C-0016
11. CONTROLLING OFFICE NAME AND ADDRESS Mission Research Corporation 1720 Randolph Road S.E. Albuquerque, New Mexico 87106		10. PROGRAM ELEMENT PROJECT, TASK AREA & WORK UNIT NUMBERS
14. MONITORING AGENCY NAME & ADDRESS (if different from Controlling Office)		12. REPORT DATE July 1982
		13. NUMBER OF PAGES
		15. SECURITY CLASS (of this report) Unclassified
		15a. DECLASSIFICATION DOWNGRADING SCHEDULE
16. DISTRIBUTION STATEMENT (of this Report) Approved for Public Release, Distribution Unlimited.		
17. DISTRIBUTION STATEMENT (of the abstract entered in Block 20, if different from Report)		
18. SUPPLEMENTARY NOTES		
19. KEY WORDS (Continue on reverse side if necessary and identify by block number) Relativistic electron beam propagation Relativistic electron beam diagnostics		
20. ABSTRACT (Continue on reverse side if necessary and identify by block number) A program of extensively diagnosed experiments to investigate the physics of intense relativistic electron-beam propagation in low-density air is in progress using beam generators at the Air Force Weapons Laboratory. The primary objectives of this research are the rate of erosion of the head of the beam, and to investigate resistive instabilities, such as the hose and hollowing modes, that limit the transport of beam energy over significant distances. The first year tasks of delineating the pressure range for maximum energy transport and measuring the temporal evolution of the current density profile		

DD FORM 1473 1 JAN 73 EDITION OF 1 NOV 65 IS OBSOLETE

SECURITY CLASSIFICATION OF THIS PAGE (When Data Entered)

DTIC
SELECTED
SEP 1 1982
H

of the beam produced by the FX-100 have been accomplished. Maximum energy transport (measured calorimetrically) of the FX-100 beam (~ 1.5 MeV, ~ 40 kA, ~ 120 ns) occurred at 0.3-0.5-Torr air pressure. This air-pressure window for maximum energy transport was defined by loss of the tail of the beam at high pressures and by erosion of the beam head at low pressures. Propagation in the window was characterized by a high degree of current neutralization ($\sim 80\%$ or more), by intense light emission, suggestive of strong avalanche breakdown, and by the onset of a virulent hollowing instability that resulted in as much as 80% of the beam current being carried in a thin annular shell at a radius about twice the Bennett radius characterizing the initially injected current distribution. Space- and time-resolved measurements of the current distribution with a fast-risetime subminiature charge collector array showed that the thin-shell hollowing instability developed late (~ 20 ns or more) into the beam pulse. Spectroscopic measurements of the visible emission suggest that the air near the axis of the beam may have been hotter and more highly ionized in this pressure regime, which may have resulted in a conductivity profile more centrally concentrated than that of the beam.

The appearance of a thin-shell hollowing instability in the pressure regime where avalanching provides an important contribution to the conductivity, which may have a profile more peaked than the beam, and where the current is highly neutralized is in qualitative agreement with existing theory and simulations. The observed delay in onset is not, but may result from imperfect air-chemistry modelling giving an erroneous delay for the buildup of an unstable conductivity profile. Propagation simulations performed in support of our experimental program showed many features consistent with the experimental results, including a high degree of current neutralization, rapid blowoff of the initially-injected beam head followed by a slower erosion, and a lack of instability early in the beam pulse. Linearized simulation suggest instability to thin-shell hollowing in the body of the beam.

The low-pressure air propagation experiments will be continued using the electron beam produced by a new accelerator (VISHNU) being constructed at the Air Force Weapons Laboratory. The VISHNU experiments will incorporate a low-pressure beam preparation cell. The rationale for this is based on our exploratory tests using the FX-25 that demonstrated the stabilization of the hose instability in full-density air by using a low-pressure beam-conditioning cell. VISHNU is design to have electron beam kinetic energy and current (~ 1.5 MeV, ~ 40 kA) close to that of the FX-100 to take advantage of our experience with that beam, but it will have a much shorter pulse length (~ 26 ns). Whether the thin-shell hollowing will be observed in the shorter-pulse experiments remains to be seen.

FX-25 and FX-100 PROPAGATION EXPERIMENTS

C. A. Ekdahl
L. A. Wright
T. P. Hughes
B. B. Godfrey

MISSION RESEARCH CORPORATION
1720 Randolph Road S.E.
Albuquerque, New Mexico 87106

ABSTRACT

A program of extensively diagnosed experiments to investigate the physics of intense relativistic electron-beam propagation in low-density air is in progress using beam generators at the Air Force Weapons Laboratory. The primary objectives of this research are to measure the rate of erosion of the head of the beam, and to investigate resistive instabilities, such as the hose and hollowing modes, that limit the transport of beam energy over significant distances.

The first year tasks of delineating the pressure range for maximum energy transport and measuring the temporal evolution of the current density profile of the beam produced by the FX-100

have been accomplished. Maximum energy transport (measured calorimetrically) of the FX-100 beam (~ 1.5 MeV, ~ 40 kA, ~ 120 ns) occurred at 0.3-0.5-Torr air pressure. This air-pressure window for maximum energy transport was defined by loss of the tail of the beam at high pressures and by erosion of the beam head at low pressures. Propagation in the window was characterized by a high degree of current neutralization ($\sim 80\%$ or more), by intense light emission, suggestive of strong avalanche breakdown, and by the onset of a virulent hollowing instability that resulted in as much as 80% of the beam current being carried in a thin annular shell at a radius about twice the Bennett radius characterizing the initially injected current distribution. Space- and time-resolved measurements of the current distribution with a fast-risetime subminiature charge collector array showed that the thin-shell hollowing instability developed late (~ 20 ns or more) into the beam pulse. Spectroscopic measurements of the visible emission suggest that the air near the axis of the beam may have been hotter and more highly ionized in this pressure regime, which may have resulted in a conductivity profile more centrally concentrated than that of the beam.

The appearance of a thin-shell hollowing instability in the pressure regime where avalanching provides an important contribution to the conductivity, which may have a profile more peaked than the beam, and where the current is highly neutralized is in qualitative agreement with existing theory and simulations.

The observed delay in onset is not, but may result from imperfect air-chemistry modelling giving an erroneous delay for the buildup of an unstable conductivity profile. Propagation simulations performed in support of our experimental program showed many features consistent with the experimental results, including a high degree of current neutralization, rapid blowoff of the initially-injected beam head followed by slower erosion, and a lack of instability early in the beam pulse. Linearized simulations suggest instability to thin-shell hollowing in the body of the beam.

The low-pressure air propagation experiments will be continued using the electron beam produced by a new accelerator (VISHNU) being constructed at the Air Force Weapons Laboratory. The VISHNU experiments will incorporate a low-pressure beam preparation cell. The rationale for this is based on our exploratory tests using the FX-25 that demonstrated the stabilization of the hose instability in full-density air by using a low-pressure beam-conditioning cell. VISHNU is designed to have electron beam kinetic energy and current (~1.5 MeV, ~40 kA) close to that of the FX-100 to take advantage of our experience with that beam, but it will have a much shorter pulselength (~26 ns). Whether the thin-shell hollowing will be observed in the shorter-pulse experiments remains to be seen.

111/1v



Accession for	
DTIC	GRA&I
DTIC TAB	Unannounced
Justification	
By	Distribution/
Dist	Availability Codes
A	Avail and/or
	Special

CONTENTS

	<u>Page</u>
I. INTRODUCTION	1
1. FX-25 Experiments	2
2. FX-100 Experiments	5
3. Theoretical Support	6
II. TECHNICAL DETAILS	7
1. FX-100 Accelerator	7
2. Field-Emission Diode	13
3. Low-Pressure Propagation Chamber	14
4. Data Acquisition	21
5. Diagnostics	22
6. Propagation Experiments	37
7. Simulations	38
III. EXPERIMENTAL RESULTS AND DISCUSSION	40
IV. PLANS FOR FUTURE EXPERIMENTS	61
1. VISHNU Accelerator	61
2. Beam Conditioning Cell	65
3. Propagation Chamber	66
V. SUMMARY	66
VI. REFERENCES	69
VII. ACKNOWLEDGEMENTS	70

CONTENTS

VIII. APPENDICES

- A. "Interim Report - Beam Propagation Experimental Study," (AMRC-N-167).
- B. "FX-100 Propagation Experiments - DARPA/Services Experimental Coordination Meeting," (AMRC-N-184).
- C. "Electron Beam Transport in a Small Aperture Faraday Cup," (AMRC-N-185).
- D. "Monte Carlo Electron Beam Transport in Air," (AMRC-N-186).
- E. "Particle Simulation of FX-100 Beam Propagation and Comparison with Experiment," (AMRC-N-187).
- F. "Optical Emission from Intense Relativistic Electron Beam Excited Air," (AMRC-R-326).

I. INTRODUCTION

Initial measurements of the hose-stable propagation pressure window and the beam current density distribution have been made using the beam produced by the FX-100 accelerator (1.5 MeV, 40 kA, and 120-ns pulsewidth). Many of the diagnostics for these measurements were developed using the beam from the FX-25 accelerator (1.5 MeV, 23 kA, and 20-ns pulsewidth).

The FX-100 was decommissioned in August 1981, and the propagation experiments will continue using the beam from an accelerator (VISHNU) presently under construction for this purpose. The VISHNU beam is designed to have the same kinetic energy and current as the FX-100 beam (~1.5 MeV and ~40 kA), but with a much shorter pulsewidth (~26 ns). Therefore, the transition to VISHNU should not involve a lengthy delay in the program, because we will be able to establish the propagation pressure window and current distribution evolution based on our experience with the FX-100 beam.

We present here a brief account of the experiments performed and results obtained in the first year of this research. Following this we give the particulars of the FX-100 experiments and results, and the technical specification of the VISHNU accelerator. Details of the FX-25 experiments are to be found in App. A.

1. FX-25 Experiments

In February, 1981 the AFWL FX-25 was made available to us for the development of diagnostics and exploratory propagation experiments. The diagnostic effort focused on the development of arrays of subminiature charge collectors for measurements of the beam spatial distribution. We performed low-pressure experiments to investigate the propagation window using a new diode designed to launch the beam with initial conditions much closer to the expected low-pressure equilibrium than in previous experiments. Finally, experiments were performed to investigate the effect on the hose instability in full-density air of using a low-pressure beam preparation cell.

The low-pressure propagation experiments were performed in a 5-cm diameter, 3-m long conducting drift tube. Most FX-25 propagation experiments in the past have used diodes that generated a hollow, non-equilibrium beam that violently pinched immediately after injection. We used a graphite Rogowski-surface cathode and 25- μ m titanium-foil anode that produced a centrally concentrated beam with a 1.7-cm e-folding radius in order to avoid shock excitation of large amplitude waves by injection of a pathological current distribution. At the 1.6-Torr air pressure for maximum energy transport the beam evolved to a Bennett-like beam profile with a Bennett radius $a \sim 0.5$ cm. Time resolved measurements with the Faraday cup array showed that energy transport was limited by erosion of the beam nose at lower pressures, and by loss of the beam tail at higher pressures.

In order to test the possibility of stabilizing the hose in full density air, the beam was extracted through a 25- μ m Kapton foil at the end of the drift tube. The rationale for these experiments with a beam conditioning cell is as

follows. The resistive hose instability on a self pinched beam is the result of the negative energy mode associated with the betatron wave. Although the betatron wavelength for electrons with different turning radii is different, the growth of the instability can often be associated with a betatron wavelength characteristic of the beam envelope. For a Bennett pinch the characteristic betatron wavelength is $\lambda_B \sim 2\pi a(I_A/2I_n)^{1/2}$, where 'a' is the Bennett radius, $I_A = \gamma\beta mc^3/e = 17\gamma\beta$ (kA) is the Alfven limiting current, and I_n is the net current that generates the pinch magnetic fields. Prior to these experiments, all high intensity beams extracted directly into full-density air were observed to become hose unstable within less than $\sim 4 \lambda_B$. In most, if not all, of these prior experiments the injection conditions were not an equilibrium for the full-density air, which resulted in the excitation of a large amplitude betatron wave at injection as the beam rapidly readjusted to a new equilibrium. Using a long conditioning cell can avoid this by establishing, at low pressure, an equilibrium close to that expected in full density air while the beam is wall-stabilized by the drift tube. If the tube is long compared with λ_B , then coherent waves excited at injection into the cell will have a chance to damp by phase mixing before injection into air. If the transition to air is made in a way that does not involve a significant change in λ_B , then it may be possible to avoid excitation of the large amplitude waves and subsequent hose instability. Consideration of the parameters defining the betatron wavelength suggests that another aid in stabilization of resistive instabilities would be to minimize the net current. This might be accomplished by sharpening the beam pulse and relying on the increase in induction fields to rapidly break down the air to increase the

conductivity and thereby reduce the return current. This suggests using conditioning-cell pressures below the propagation window, where pulse sharpening by nose erosion is significant.

We performed the experiments using only a minimal set of diagnostics including net current measurements (in the cell and outside) and open-shutter pictures to observe the full-density hose instability. We varied the cell air pressure from above the 1.6 Torr pressure for maximum energy transport to well below this value. A marked stabilization of the hose was observed at drift-tube pressures below 1 Torr. This appeared to be a threshold effect in the sense that there was a very narrow range of pressures (0.7-0.8 Torr) below which the beam was markedly more stable. The full-density propagation was limited to less than ~ 6 betatron wavelengths by the presence of a shield wall. Whether the stabilization resulted from pulse-sharpening in the drift tube, profile broadening at the lower pressure, or equilibration and betatron phase mixing is unclear at this time. However, the fact that there was no threshold in the pulse sharpening in the drift tube that corresponded to the observed threshold for full-density hose stabilization is suggestive that, although pulse sharpening and the increased return current fraction that results from the enhanced conductivity can be contributory, it is not the major effect. Net current measurements were inconclusive, but they were suggestive that there was no large disparity between internal and external net currents when the beam was stabilized.

2. FX-100 Experiments

Propagation experiments with the FX-100 accelerator commenced in April, 1981 after extensive repairs and modifications. These experiments continued into August, when the FX-100 was decommissioned and removed in order to provide space for the development of the first RADLAC II module. Low-pressure air-propagation experiments were performed to delineate the propagation window and to measure the beam-current distribution in the hose-stable propagation regime.

A graphite Rogowski-surface cathode produced a beam that was injected into the 20-cm diameter conducting drift tube through a 25- μ m titanium-foil anode. The injected beam had a 3-cm Bennett radius. As in our FX-25 experiments the propagation window was defined by beam-nose erosion at low pressures and by loss of the beam tail at high pressures, observed now with streak photography so well as with Faraday cups. Maximum energy transport through 5 meters of drift tube occurred at 0.5-Torr pressure. Near this peak in the window we discovered that much of the current was frequently carried in an annular "halo" that apparently developed as the result of a hollowing instability with an onset late in the beam pulse.

Measurements of light emitted by the beam excited and ionized air showed the presence of singly-ionized atomic nitrogen near the axis, at radii much less than the beam Bennett radius, in the pressure range characterized by the hollowing instability. This may be indicative of a hotter, more highly ionized (and, therefore, more conductive) gas near the axis. This condition is theoretically conducive to the development of a hollowing instability.

The appearance of the hollowing instability in the pressure regime where avalanching provides an important contribution to the conductivity, and where the beam was observed to be highly current neutralized, is in qualitative agreement with theory and simulation. The long delay before onset is not yet fully understood, but may result from the time delay to form a peaked conductivity profile, an imperfect chemistry model in the codes that predict rapid onset, a pathological change in diode characteristics, or some combination of these.

3. Theoretical Support

Throughout the course of the experiments theoretical and computational support in the design of diagnostics and the interpretation of the data was provided by several MRC theorists. The details of these studies are to be found in Appendices C, D, and F in particular. In addition, particle simulations with the MRC codes KMRAD and CPROP provided major insights into the physics of the beam-nose erosion and instabilities observed in the FX-100 experiments.

The beam propagation simulation code CPROP showed large return currents (~80%) when avalanching was included in the conductivity model. In the experiments the return current fraction was 80-90% in the propagation window. At pressures greater than ~0.5 Torr, avalanching causes the conductivity to concentrate on axis, which can drive a beam hollowing instability. The erosion of the beam seen in the simulations was not inconsistent with the observations. The linearized simulation code KMRAD was used to search for $m=0$ instabilities such as observed experimentally. A short-transverse wavelength instability was

instability was observed even with an unpeaked conductivity profile. This mode had a group velocity much less than the beam velocity and may be the source of the fine structure seen experimentally. The details of these studies may be found in Appendix E.

II. TECHNICAL DETAILS

1. FX-100 Accelerator

The FX-100 accelerator was a gas-insulated coaxial transmission line that was DC charged with a Van de Graaff belt-charging system, and then was discharged into the field-emission diode with a single output switch. The insulating gas was 10% SF₆ in nitrogen, which was pressurized to ~200 psi in order to provide the required insulation strength. The energy storage transmission line impedance was 43 Ω , and it had a 34 ns one-way electrical transit time. The triggered gas output switch was followed by a 4.2-ns long, 233- Ω stacked-ring envelope and a 3.8-ns long, 160- Ω vacuum transmission line. The last stage of the vacuum line consisted of a short (~1 ns) length with lower impedance (~80- Ω) to reduce shank emission losses. This final section of vacuum coax was terminated with the 55- Ω field-emitting diode consisting of a graphite cathode and titanium foil anode through which the electron beam was injected into the low-pressure propagation chamber (Fig. 1).

The high-impedance envelope and vacuum transmission line of the FX-100 dominated the output impedance regardless of the diode impedance, and produced a diode current waveform with oscillations at a frequency characteristic of the ~70-ns down-and-back time of the charged energy-storage transmission line

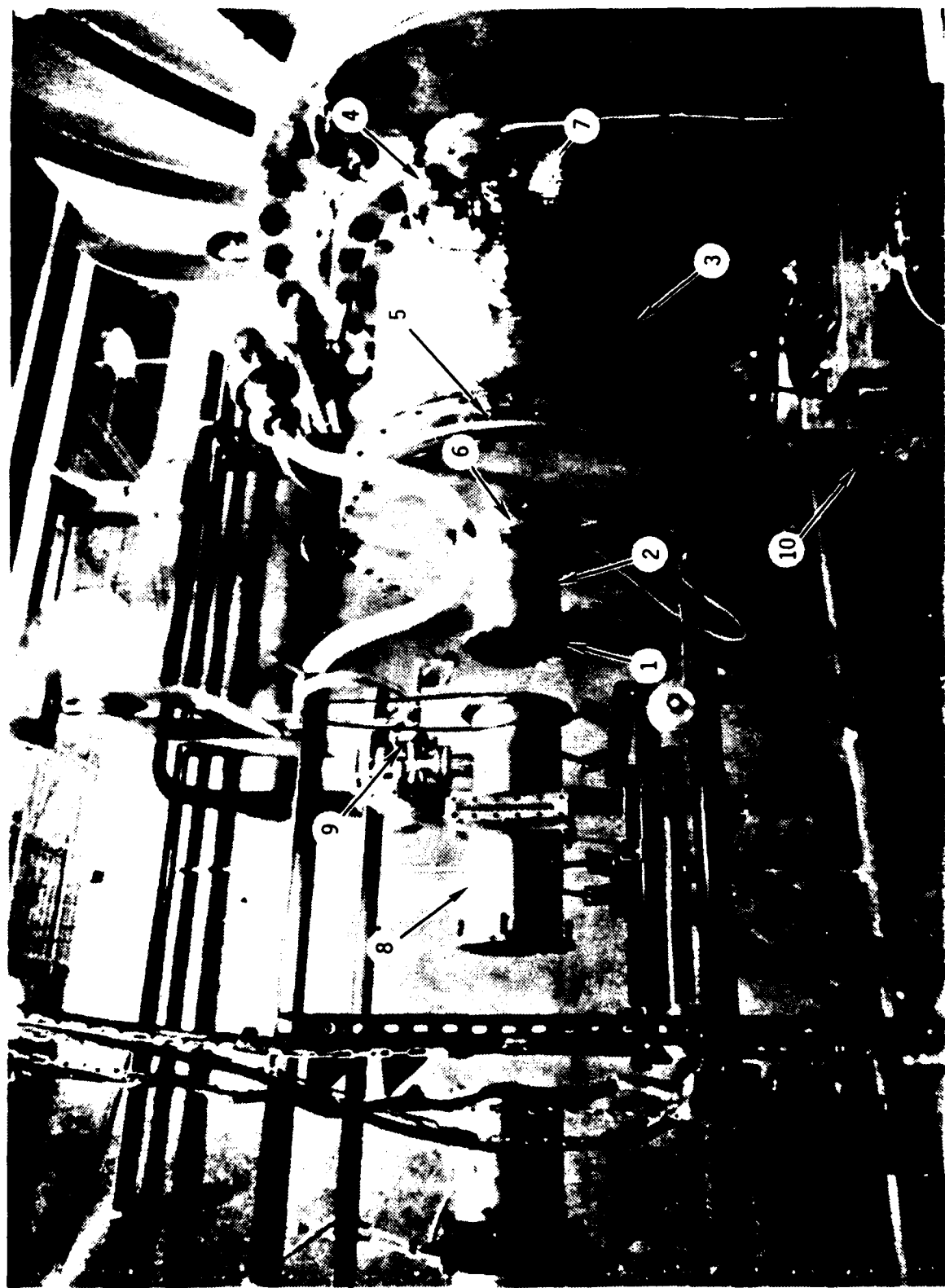


Figure 1. Output section of FX-100 Van de Graaff e-beam generator. (1) Anode foil; (2) Final (80-100) vacuum transmission line; (3) 160- Ω vacuum transmission line; (4) Diode vacuum gauge; (5) 2-m Ω resistive shunt diode current monitor; (6) Rogowski belt diode current monitor; (7) Capacitive voltage monitor (behind vacuum tee); (8) Two sections of propagation experiment low-pressure drift tube; (9) Propagation experiment gas manifold; (10) Diode

(Fig. 2). The transmission-line stored energy was eventually extracted from the diode in a pulse with ~ 120 ns width. Although it can be argued that this output pulseshape was not ideal for propagation experiments there was insufficient time to allow for the rather substantial (but straightforward) modifications to the FX-100 that would have resulted in a more closely matched output.

Indeed, a considerable effort was expended to bring the FX-100 up to a performance level suitable for these experiments. A series of high-voltage insulation failures in the Van de Graaff charge-belt insulator stack late in calendar 1980 resulted in the incapability of charging the intermediate coax to the required operating voltage. During the lengthy repair of the damage resulting from these failures we implemented a simple modification to the insulator protection spark gaps that prevented a recurrence of this failure mode during the course of the propagation experiments.

An additional technical problem was the output-switch trigger system. It was not sufficiently reliable for the required reproducibility of beam parameters. We corrected the trigger problem by designing and installing a pneumatically operated field-distortion trigger pin. The trigger-pin actuating unit is shown in Fig. 3, and Fig. 4 shows the trigger as installed in the gas-insulated output switch. This trigger pin was designed to be actuated by the pressure differential between two dielectric gas lines run to the exterior of the FX-100 tank. This design avoids a high-voltage discharge through the dielectric lines by maintaining the dry-nitrogen working-gas pressure at greater than the ~ 200 -psi tank pressure. This unit provided reliable

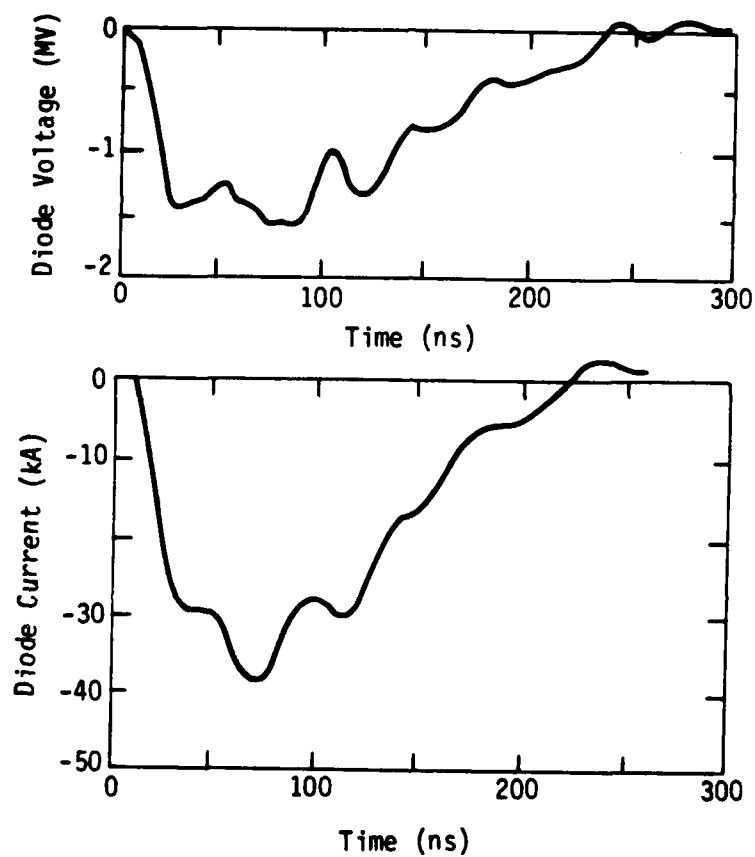


Figure 2. FX-100 diode voltage and current. The gas-insulated coax was charged to 4.2 MV in order to produce this output. This charge voltage remained unchanged during the course of the propagation experiments.

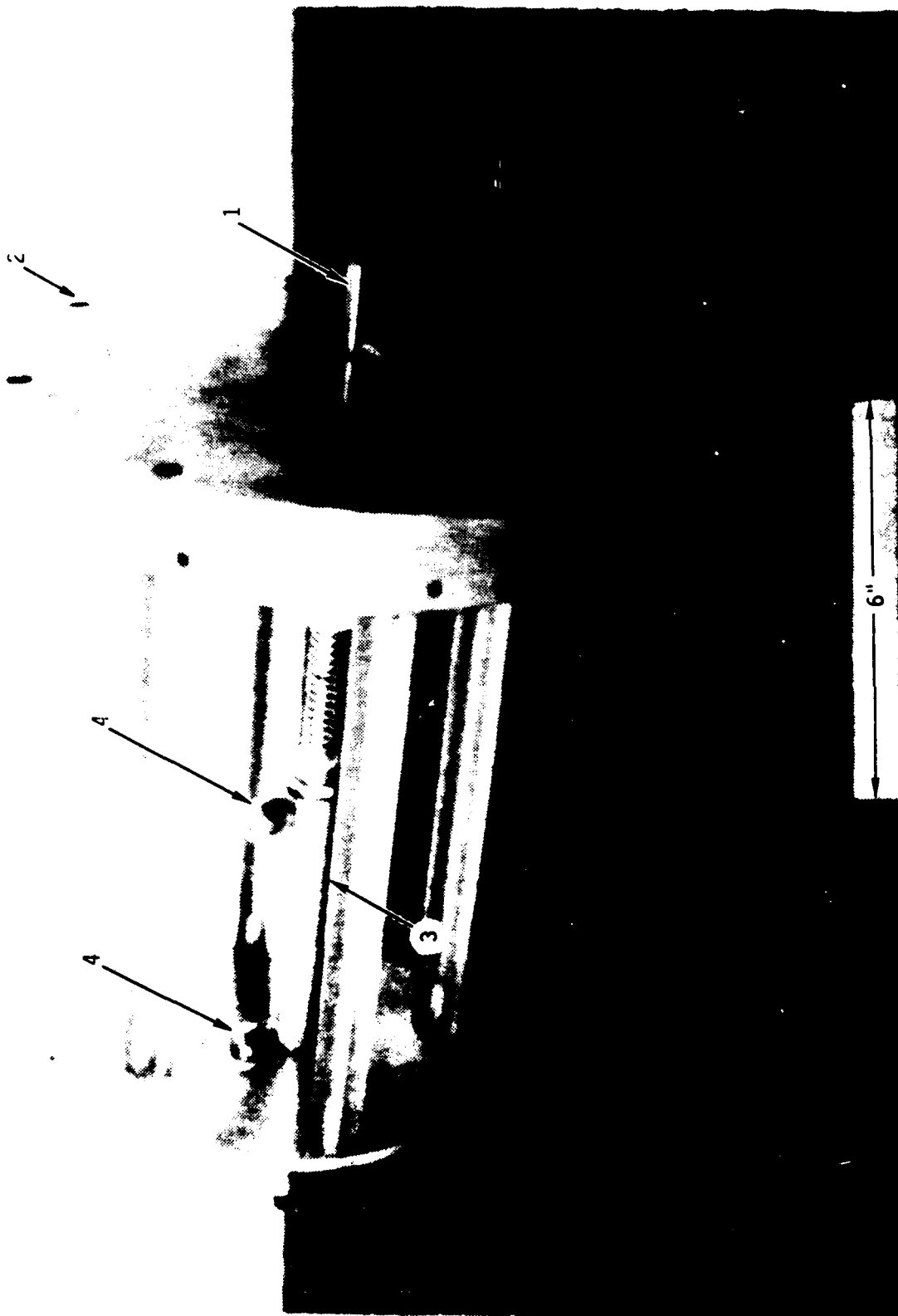


Figure 3. Pneumatic trigger for FX-100 output switch. (1) Field distorting trigger pin (partially extended); (2) Mounting flange; (3) Double-throw pneumatic cylinder; (4) High-pressure nitrogen gas lines. Trigger pin is retracted by maintaining pressure differential on high pressure N₂ lines. Reversing the differential extends the pin, distorts the fields in the gap and initiates the gap spark. Maintaining N₂ pressure in the dielectric lines



Figure 4. Pneumatic trigger installed on FX-100. (1) Trigger pin (partially extended); (2) Mounting flange; (3) Output switch end of coaxial energy-storage transmission line.

triggering of the output switch and highly reproducible voltage and current pulses for the remainder of the operational lifetime of the FX-100.

The FX-100 was decommissioned in mid-August, 1981 in order to provide space for the development of the RADLAC accelerator. During the ~4-month period that it was available after making the aforementioned repairs and modifications we fired over 500 shots in the execution of the low-pressure air propagation experiments.

2. Field-Emission Diode

We designed the diode used in the FX-100 propagation experiments to produce an electron beam with a radial current distribution close to that expected for a propagating beam equilibrium. That is, the desired current distribution was a Bennett pinch, which would have a current density $j(r)=j(0)[1 + r^2/a^2]^{-2}$, where 'a' is the Bennett radius. In order to achieve a distribution that closely approximated this ideal we used a smoothly-polished graphite cathode that had a surface shape congruent to one of the static vacuum equipotential surfaces of a charged disk. Such a Rogowski surface has little static field enhancement resulting from charge concentration. This electrostatic solution is obviously not self-consistent in the presence of space-charge and magnetic fields of the intense beam produced. However, experience has shown that the field-emission from a smooth Rogowski surface can be readily controlled by selectively roughening small areas in order to provide microscopic field enhancement early in the voltage pulse.

By roughening a small circular region in the center of our FX-100 cathode (shown in Fig. 5) we were able to produce Bennett-like extracted current distributions as illustrated by Fig. 6 and Fig. 7. Figure 6 shows the diode geometry and the current distribution measured 1.3-cm from the titanium foil anode at the time of maximum diode current. From this figure it is clear that the beam-electron scatter resulting from the foil can provide an additional means for increasing the Bennett radius, if so desired. Because we wanted the smallest possible beam radius we used the thinnest foils that survived the beam (25- μ m) in all of the propagation experiments. With these anodes the Bennett radius of the extracted beam was ~ 3 cm (Fig. 6).

From Fig. 7, which shows the temporal and spatial evolution of the beam current profile, it is evident that the beam produced by our diode had a Bennett-like radial distribution during most of the beam pulse. It is also clear that there was very little evidence of shank emission current at large radii, except possibly at very early and very late times.

3. Low-Pressure Propagation Chamber

The low-pressure air propagation experiments were performed with the electron beam injected directly into the 20-cm diameter stainless-steel propagation chamber through the 25- μ m titanium-foil anode. This diameter was initially deemed large enough to insure that wall effects would not dominate the 3-cm radius beam propagation, but in retrospect it appears that the chamber should have been larger. The propagation chamber, or "drift tube", consisted of many individual 25-cm long segments bolted together with 'O'-ring sealed

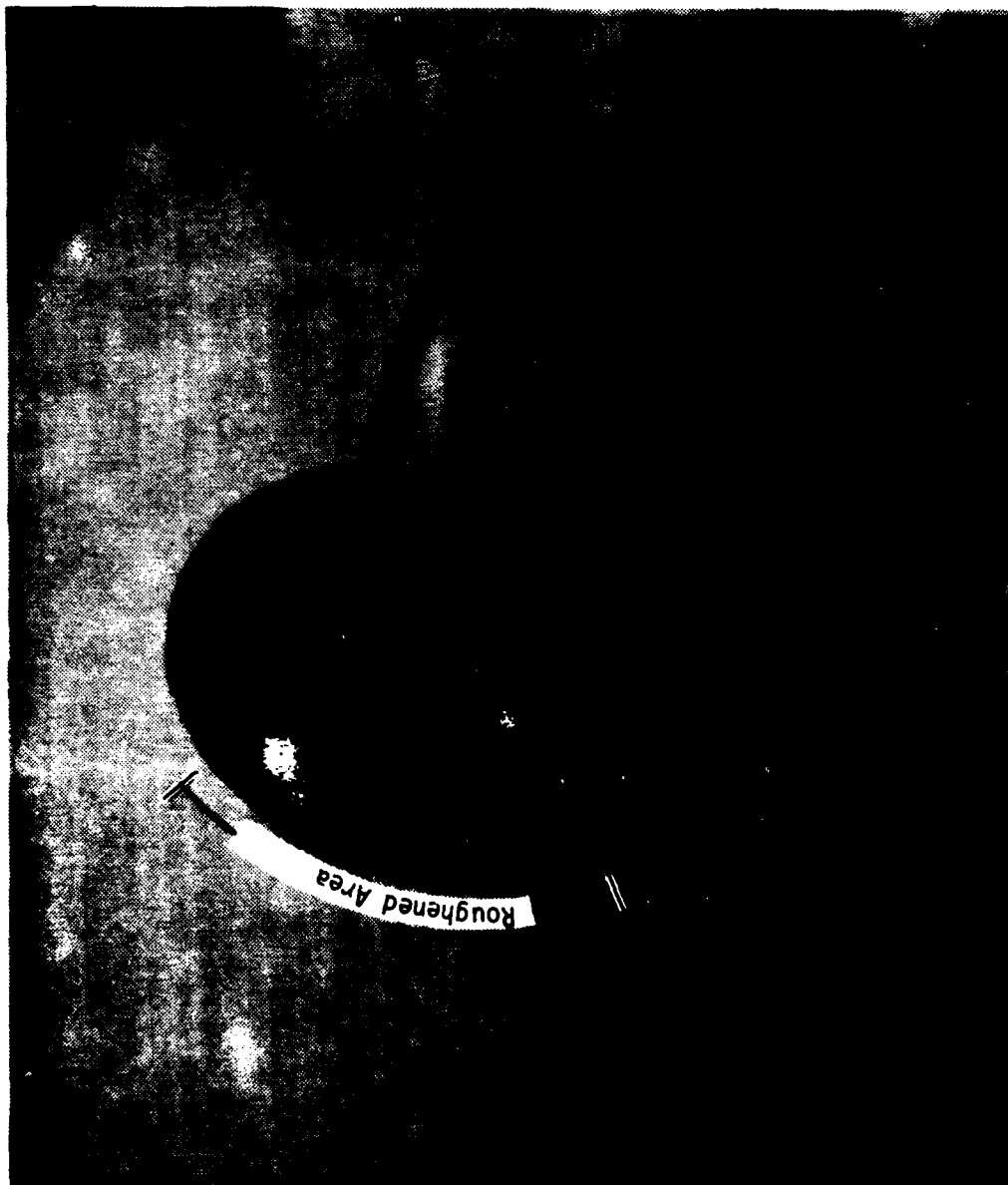


Figure 5. 5-cm diameter polished graphite Rogowski-surface cathode used in FX-100 beam propagation experiments. The central 4-cm diameter area that was roughened to enhance emission is delineated for clarity.

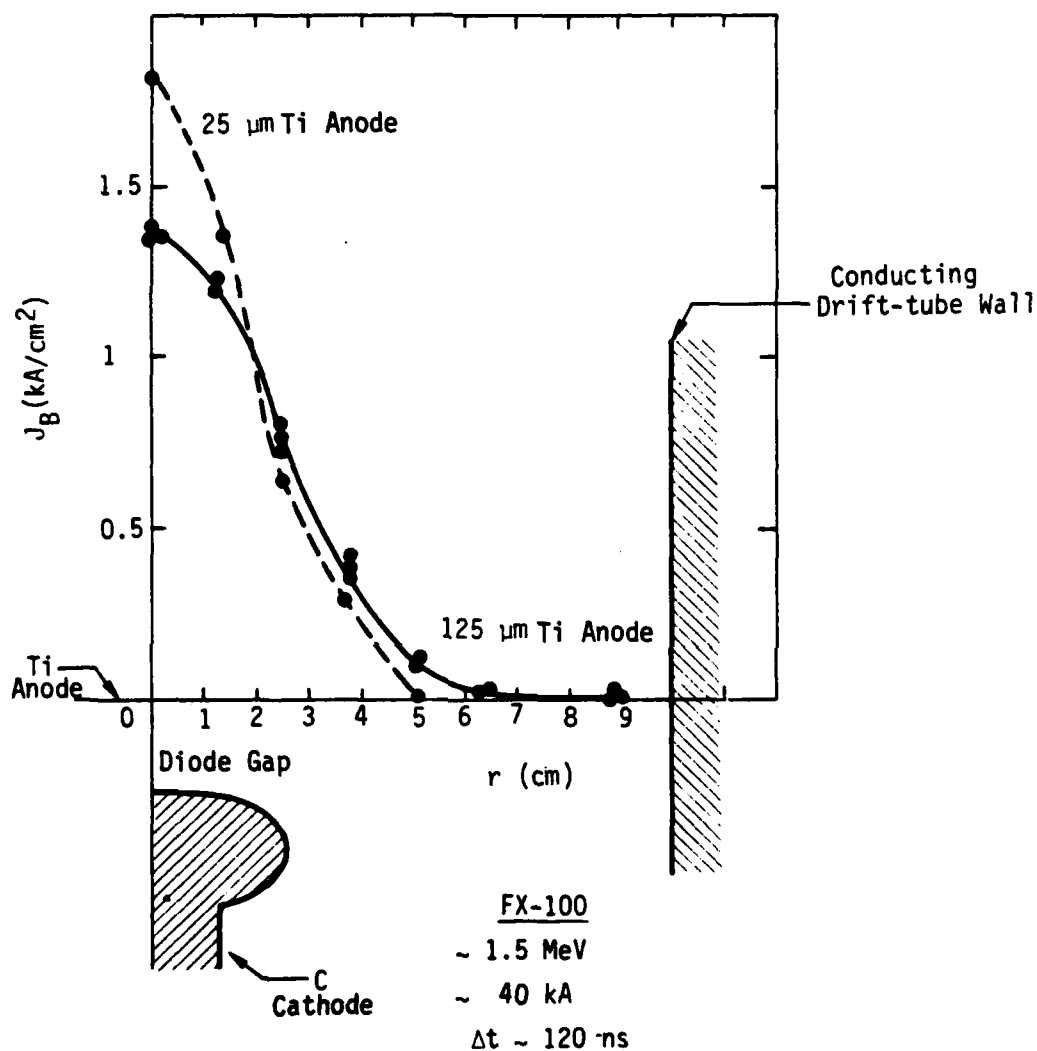


Figure 6. Multiple Faraday collector array measurements of FX-100 beam current density distribution in vacuum 1.3 cm from the anode foil. Distribution for two different foil thicknesses are shown. However, all propagation experiments were performed using 25-μm Ti foil anodes.

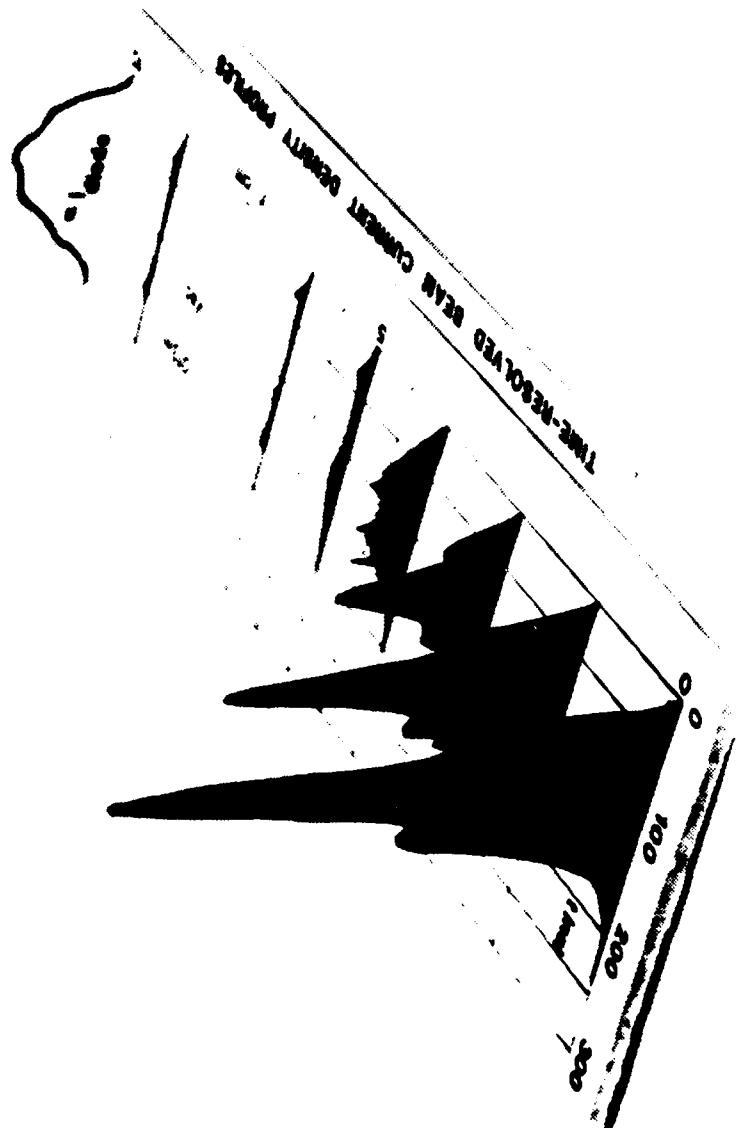


Figure 7. Time-resolved beam current density, profile measured 1.3 cm from 25- μ m Ti anode foil in vacuum.

flanges. Several sections of the drift tube are shown in Fig. 1, and the maximum available length of assembled drift tube (> 5 m) is shown in Fig. 8 and Fig. 9. This modular design afforded a great amount of flexibility in the axial location of diagnostics for the propagation experiments.

The air pressure in the propagation chamber was controlled with a pumping manifold and adjustable leak (Fig. 1), and was monitored with a Granville-Philips Pirani gauge that was calibrated with an oil manometer. The minimum pressure attainable with this system was ~ 0.1 Torr, which was low enough to cover the pressure range of interest.

Some of the experiments (eg., multiple exposure spectroscopy) required high repetition rate firing of the FX-100 (~ 3 -5 minute turn-around per shot). For these experiments the slow leak valve was positioned at the extremity of the drift tube to insure adequate mixing and flushing of possible air-chemistry by-products between the shots. There was no measurable pressure gradient in the tube in this configuration.

For most experiments the turn-around time was sufficiently long that air-chemistry by-products could mix and be evacuated even with the leak valve located near the pumping port. In any event, we detected no effect in our data that could be traced to the accumulation of chemistry by-products.

In order to ascertain the significance of the small amount of water vapour present in the low-humidity ambient air used for most experiments, a limited number of experiments were performed using dried air and pure nitrogen. Except that the red oxygen line emission was not observed in the pure N_2 experiments there was no discernable effects evident in the measurements.

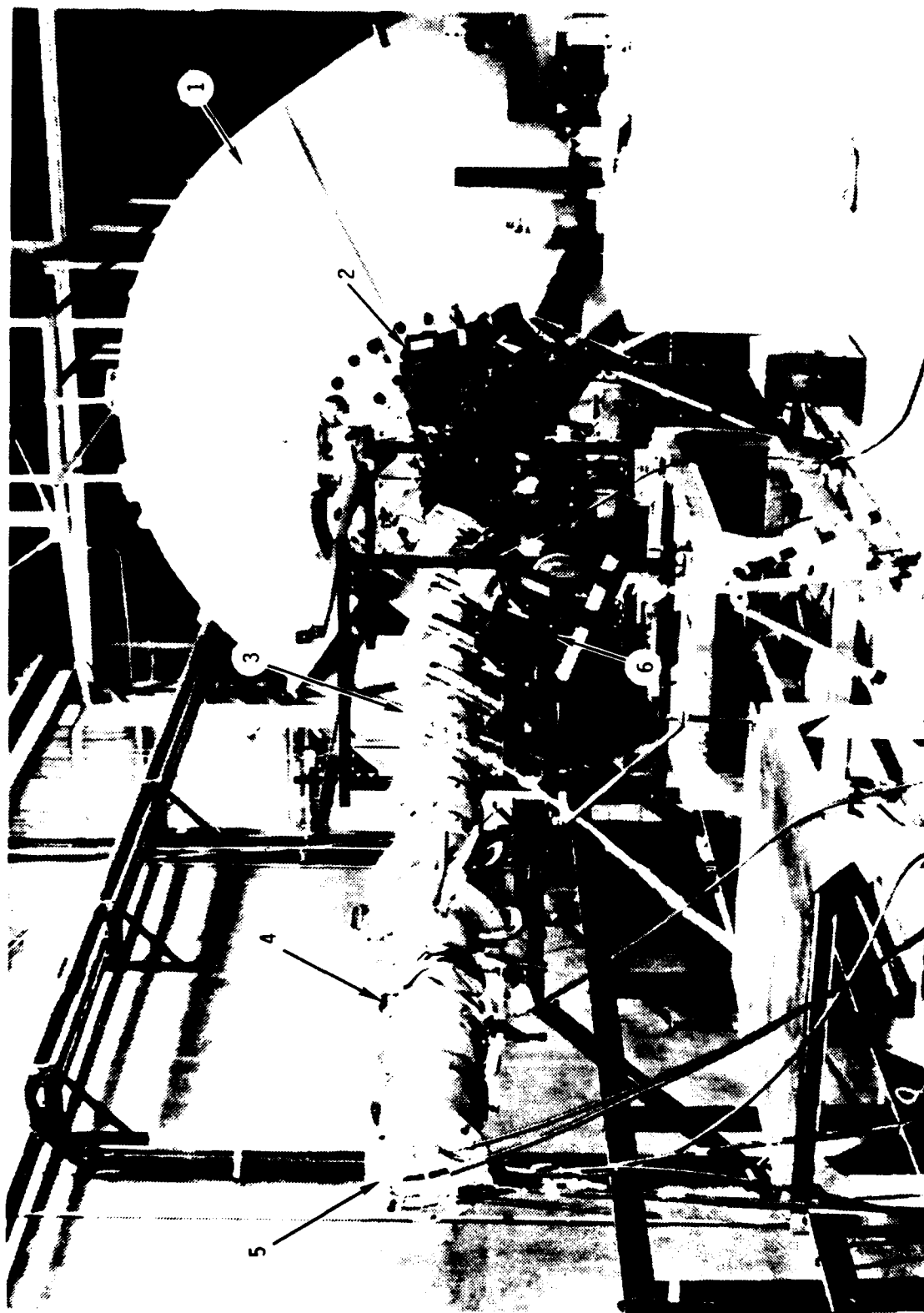


Figure 8. Assembled FX-100 low-pressure air propagation experiment. (Total length > 5 m.) (1) FX-100 tank; (2) Open-shutter camera; (3) 20-cm diameter stainless-steel drift tube; (4) Inductive current monitor; (5) Signal cables for charge collector array and carbon calorimeter; and (6) Open-shutter camera.

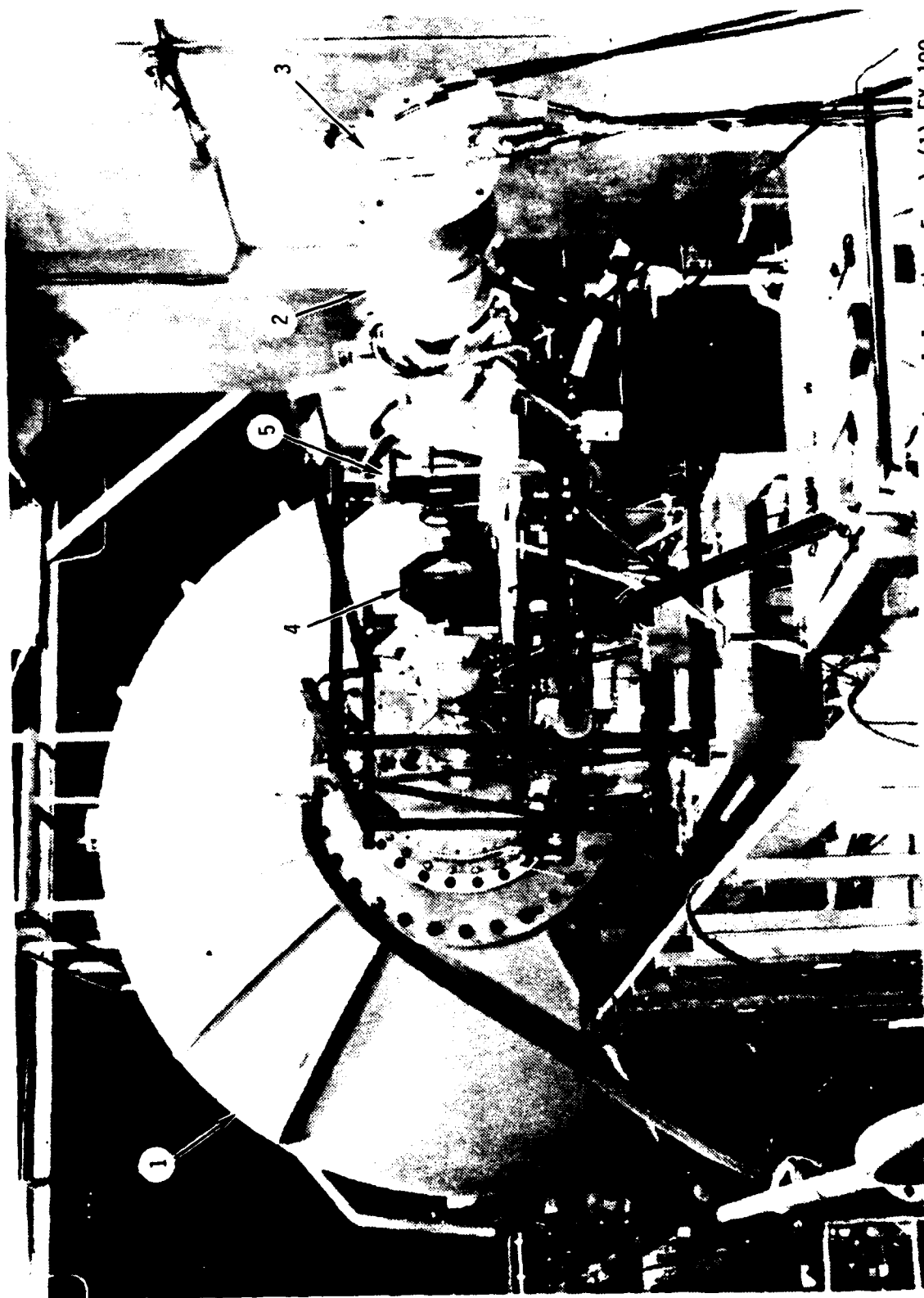


Figure 9. Assembled FX-100 low-pressure air propagation experiment. (Total length > 5 m.) (1) FX-100 tank; (2) Inductive current monitor; (3) Signal cables for array of charge collectors and carbon calorimeter; (4) First turning mirror for streak-camera optical delay path; (5) Viewing window.

4. Data Acquisition

Data acquisition for the propagation experiments was originally limited by the number of signal cables installed between the screen room and the experimental area. During the course of the experiments more cables were installed until eventually it was possible to record 12 channels of time-resolved data, at which point we exhausted the available oscilloscopes. In addition, we recorded time-integrated data, such as calorimetric measurements of the beam energy deposited in a target at the extremity of the drift tube.

All time-resolved data was recorded using Tektronix 7704 oscilloscopes with 7A11 preamplifiers. The bandwidth of this preamp-oscilloscope combination is ~ 150 MHz, which limited the measurable signal risetimes to ~ 2.5 ns in the absence of signal-cable dispersion.

The battery of oscilloscopes was triggered with a signal derived from the light emitted by the FX-100 gas output switch. We constructed a simple system consisting of a biased EGG SGD-040A solid state photodiode detector that triggered a PATCO PA-006 avalanche transistor pulse generator. This compact, battery-powered system provided a high-level (~ 300 V) low-jitter trigger pulse with a fast risetime. Attenuation of this signal in the screen room to a level compatible with the oscilloscopes resulted in a noise-free and reliable trigger. The delay between the onset of light emission from the output switch and the FX-100 electron beam was sufficient to record the entire beam history using 50-ns/division oscilloscope sweep speeds.

The oscilloscope trigger signal was also used to generate a timing fiducial marker in the screen room, which consisted of the differentiated and clipped output of a triggered delay generator. This marker, when added to each data signal at the oscilloscope, provided an accurate means for comparing data obtained on different diagnostic channels after accounting for the different signal cable delays. These cable delays were measured to an accuracy of ~ 2 ns using time-domain reflectometry techniques.

This data acquisition system allowed a resolution and comparison of photographically recorded oscilloscope traces to within ~ 2 -4 ns, which is comparable to the limitation on the signal risetime from the signal cable dispersion and oscilloscope-preamplifier bandwidths.

5. Diagnostics

Diode Voltage and Current Monitors Interpretation of the experimental data obtained with other diagnostics requires accurate and precise monitoring of the accelerating diode voltage and diode current during the course of the propagation experiments. The diode monitors used for the FX-100 low-pressure propagation experiments are described in this section.

The voltage monitors installed on the FX-100 were found to give irreproducible signals, probably because of electrical noise and electron impact effects. We replaced them with a dielectric protected capacitive detector that gave a signal proportional to the rate of change of the diode voltage (V-dot probe).¹ This probe is a small (~ 2 -cm diameter) copper disk positioned just inside of the outer conductor of the vacuum transmission line.

It is completely encapsulated in epoxy to avoid problems with unwanted signals resulting from low-energy electrons generated by UV irradiation, Compton currents, etc.

The probe capacitively couples to the transmission line voltage and can be represented by the equivalent circuit shown in Fig. 10.

When the load resistance is matched to the signal cable impedance ($R_2 = Z_0$) the output signal, $V_2(t)$, is related to the transmission line voltage waveform, $V_1(t)$, by the differential equation:

$$\frac{dV_2}{dt} + \frac{V_2}{RC} = \frac{R_2 C_1}{RC} \frac{dV_1}{dt} \quad , \quad (1)$$

where $R = R_1 + R_2$ and $C = C_1 + C_2$. Clearly there are two possible modes of operation depending on the value of RC . If RC is much less than the fastest rate of change of the signal ($RC \ll \tau$), the second term on the left side of Eq. 1 dominates, and the output signal, V_2 , is proportional to the derivative of the transmission line waveform;

$$V_2 = R_2 C_1 \frac{dV_1}{dt} \quad . \quad (2)$$

This is referred to as the "V-dot" mode of operation, and the signal requires further integration to obtain the input voltage waveform, V_1 .

On the other hand, if RC is much greater than the longest time of interest, the first term on the left side of Eq. 1 dominates, and the probe

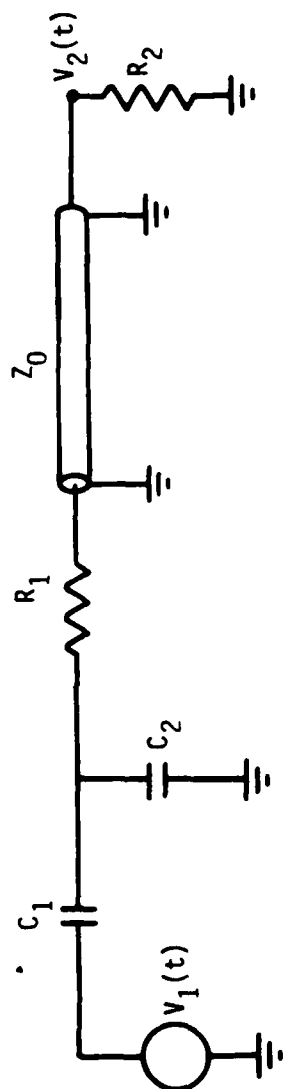


Figure 10. Equivalent circuit of FX-100 diode-voltage capacitive monitor.

acts as a capacitive voltage divider^{2,3} with the output signal, V_2 , directly proportional to the transmission line voltage, V_1 ;

$$V_2 = \frac{R_2 C_1}{RC} V_1 \quad . \quad (3)$$

It is clear that a large series resistor, R_1 , or additional integrating capacitance, C_2 , would be required for the voltage division mode of operation. Because of the high level of electromagnetic noise in the experimental area, the V-dot mode of operation was chosen instead for the FX-100 probes. In this mode, the high signal level was transmitted to the screen room and integrated there with a passive integrator having $RC \sim 2 \mu s$ with the result that unwanted electromagnetic noise picked up by the signal cables was highly attenuated. In addition to this inherent noise immunity and their compact construction, advantages of V-dot capacitive monitors over resistive dividers for the FX-100 experiments are that they do not distort the fields in the region of measurements, they are immune to surface tracking and breakdown, they do not shunt the load with a lower impedance, and they require no balancing of resistive and capacitive elements or complicated voltage-grading structures.

The V-dot probe was located in the vacuum transmission line within ~ 0.5 m of the diode anode-cathode gap. It was found that inductive correction for the final short section of transmission line between the monitor and the gap was unnecessary for these experiments. This V-dot probe provided a highly reliable and reproducible monitor of the diode accelerating voltage on each shot.

We monitored the diode current with a Rogowski belt^{4,5} supplied by the AFWL. Several of these were made available for the propagation experiments. The Rogowski loop in these current monitors was embedded in an annular groove in a flange that could be inserted at any point in the drift tube. The loop used as a diode-current monitor was positioned on the section of drift tube that we used to form the final vacuum transmission line segment. That is, the current was monitored in the vacuum transmission line within 25-cm of the diode anode-cathode gap (see Fig. 1).

Typical FX-100 diode current and voltage waveforms at the charging voltage used for these experiments are shown in Fig. 2.

Inductive Current Shunts One of our primary research objectives is a study of the beam-head erosion process, which can lead to rapid net-current risetimes in the drift tube. For these measurements we designed and constructed inductive shunt¹ net-current detectors that had substantially faster response times than the available Rogowski loops.

The inductive-shunt current monitors consisted of epoxy-filled annular channels machined in an aluminum flange that was inserted between two sections of the drift tube. As can be seen in Fig. 11, the return current flowing on the drift-tube inner surface was forced to flow around the inside surface of the annular channel. A voltage was thus induced across the insulating gap by the time-varying magnetic field in the annular channel. In the limit of time-scales short compared with the magnetic diffusion time into the aluminum shunt, the voltage appearing around the channel is purely inductive and can be

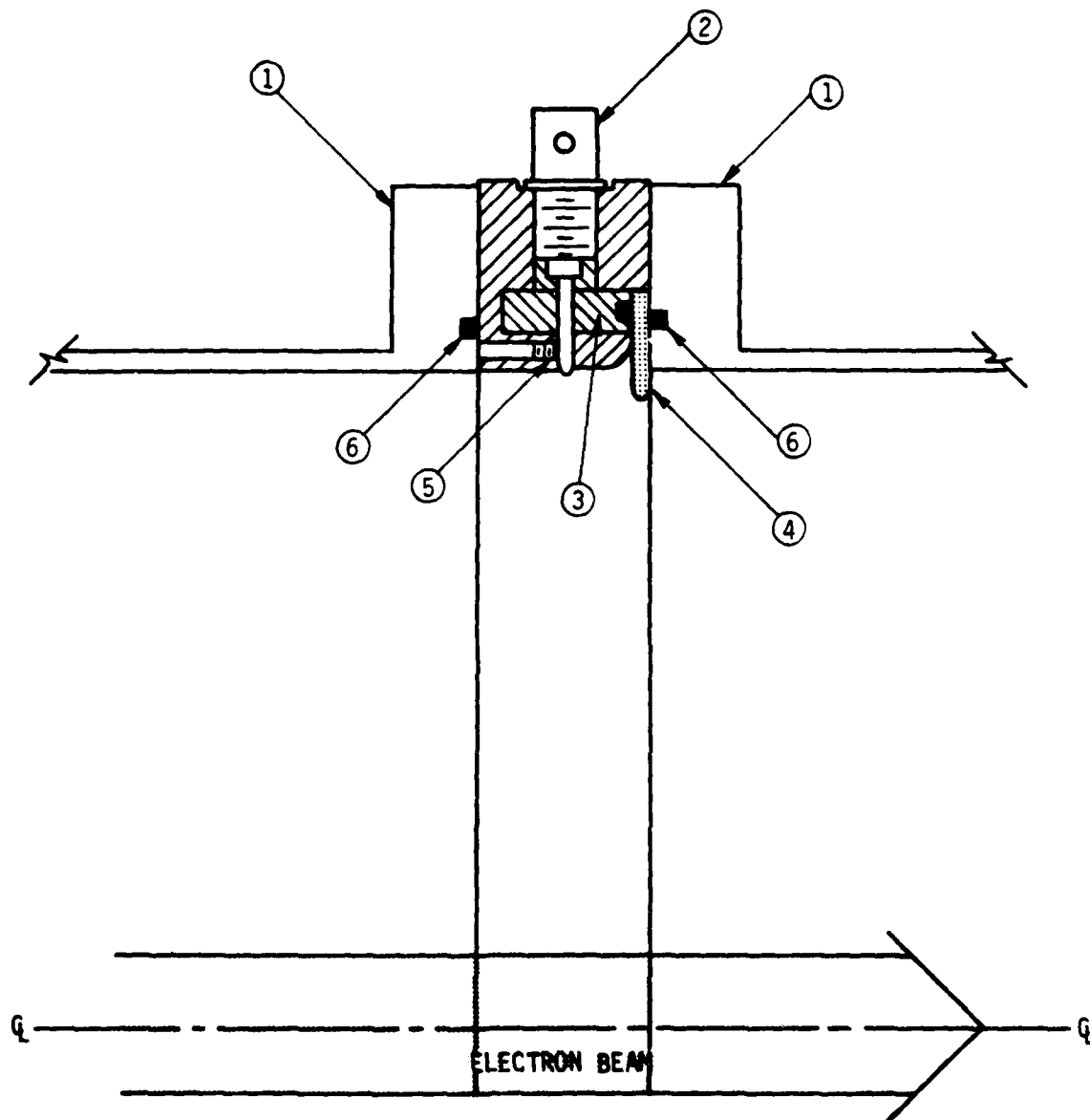


Figure 11. Fast-risetime inductive-shunt current monitor installed between two sections of drift tube (1). (2) is BNC signal-output. (3) is epoxy filled annular channel. (4) is polyethylene insulating gasket. (5) is set screw to provide electrical contact for detector pin. (6) are 'O' ring vacuum seals.

detected by completing a flux loop as shown in Fig. 11. The inductive component of the voltage that appears at the pick-up point is given by;

$$V = - \frac{d\phi}{dt} = - \frac{\mu_0}{2\pi} \frac{dI}{dt} \int \frac{drdz}{r} \quad , \quad (4)$$

Substituting the inductance, L , for the FX-100 shunt geometry into this equation gives

$$V = - \frac{\mu_0 w}{2\pi} \ln \frac{r_o}{r_i} \frac{dI}{dt} \quad , \quad (5)$$

where r_o is the outer radius of the channel, r_i is the inner radius, and w is the channel depth below the pickup termination.

An advantage of this type of current monitor is that it provides a simple penetration of the conducting drift tube that results in a well-shielded coaxial signal-transmission geometry. In addition, the narrow insulating gap is a wave guide beyond cutoff for low-frequency modes other than the TEM mode that is excited by the time-varying axial current, and thus provides shielding from unwanted electromagnetic noise. Furthermore, although a single voltage pickup is sufficient for an azimuthally symmetric system such as a coaxial transmission line, asymmetric current channels can be accurately measured by summing the signals from several voltage pick-ups separated by equal increments of angle. In this respect, the inductive-shunt monitor can be thought of as the well-shielded limit of a Rogowski belt^{4,5} current monitor. Finally, the achievable risetime of an inductive-shunt monitor is substantially faster than

for a Rogowski coil because the output signals are summed in parallel rather than in series, thus significantly reducing the inductance and L/R risetime.

For the FX-100 propagation experiments the eight output signals from each shunt were summed in a transformer signal adder that limited the had the capability for summing subnanosecond signals. These net current monitors positioned at various axial positions during the different phases of the program. They provided reliable, low-noise measurements of the net current in the drift tube.

Subminiature Faraday-Cup Array An array of fast-response Faraday charge collectors was developed to measure the time-resolved current distribution. The data from this array provided a picture of the evolution of the radial current profile at a particular axial location without relying on shot-to-shot reproducibility, which is certain to be poor in any experiment involving instabilities. Each detector in the array consisted of a length of Uniform Tubes Co. UT-47 rigid coaxial transmission line that was embedded in a massive graphite block, as shown in Fig. 1, Appendix A. and also Fig. 1, Appendix C. The initial radial spacing of the detectors was chosen to be 1.25 cm. However, our early discovery of significant beam current carried outside of the Bennett radius caused us to modify the array by increasing the detector density at large radii. The collectors were shielded from the ionized-gas electrons and low-energy secondaries by a thin graphite sheet in the original array developed during the FX-25 experiments. The array that we constructed for the FX-100 propagation experiments used a 125- μ m thick titanium foil plasma shield that was insulated from the collectors with 25- μ m thick Kapton dielectric foil. Of

all dielectric materials that we have experimented with, Kapton (a polyimide) exhibits the most resistance to the intense beam irradiation. Although we replaced the shielding and insulating foils on a regular basis as a precaution, we had few problems with insulator breakdown in this array.

Electron scattering in the array materials results in an energy-sensitive effective collection area. The reason for this is that the more energetic electrons have a higher probability of scattering into the collector because of their greater depth of penetration. We studied this effect by using the Monte Carlo radiation transport code CYLTRAN to obtain the energy sensitivity of the effective collection area. Details of this study are reported in Appendix C. The energy sensitivity appears to be modest over a wide range of energies around the peak energy of the FX-100 beam, but the collection area for these high-energy electrons is significantly (factor of ~ 2) enhanced over the geometrical area. As a consequence, such a detector cannot be readily adapted to measurements of net current because of the vastly different sensitivities to beam and plasma currents.

The developmental experiments using the FX-25 beam demonstrated that the risetime for these coaxial collectors driving a matched and properly terminated signal cable was limited only by the cable dispersion and oscilloscopes. In those experiments 1-ns risetimes were observed. The combination of the high level signal generated by these collectors and the unbroken coaxially-shielded construction resulted in a high signal-to-noise ratio on the oscillograms. The injected current distribution shown in Fig. 2 was obtained with this array, and many examples of stable and hollowing-mode unstable current profiles are included in the various appendices.

Carbon Calorimetry The graphite block containing the array of Faraday collectors was also used as a beam calorimeter by measuring its temperature rise with a thermistor. Because carbon calorimetry integrates over time, space, and the beam-energy distribution, it is impossible to distinguish beam-electron energy losses from loss of transported charge without simultaneous, precise measurements of beam current. The carbon calorimeter is quite simple to field in this kind of experiment, and it is the traditional diagnostic for definition of the propagation pressure window. Our use of a thermistor sensor simplified the measurements. The thermistor was found to be insensitive to radiation, and when calibrated, it was found to have a linear response over the restricted temperature range of this application.

Incorporation of the charge-collector array into the calorimeter block enabled us to simultaneously determine the beam energy transport and the temporal evolution of the radial current profile at any given axial location. A limited number of measurements were made with the calorimeter in vacuum, and isolated from the ionized-gas channel by a titanium foil. The results of these measurements indicated that the energy deposited on the calorimeter from the plasma was not a significant fraction of the beam energy.

These calorimetric measurements of beam energy transported through the drift tube filled with air at different pressures were used to establish the pressure window for maximum transport shown in Fig. 15.

Radiochromic Foil Dosimetry Blue cellophane is one of the most widely used radiochromic film dosimeters.⁶ Blue cellophane exposed to an intense electron beam such as generated by the FX-100 exhibits effects ranging from bleaching of

the organic dye through destruction of the film. Although the sandwich structure of the film to some extent discriminates against bleaching resulting from low-energy secondaries and plasma electrons, a sufficiently large low-energy current can produce misleading damage because of the reduced electron range. A means of separating the beam and plasma channel radial structures by comparing bleaching foil records with X-ray pinhole camera pictures of the beam electron bremsstrahlung from a wire mesh was suggested in the proposal for these experiments. We chose instead to employ a more simple method, we shielded the blue cellophane from low-energy electrons with thin metal foils. Typically, we used 25- μ m thick titanium-foil shields, which will stop electrons with less than \sim 180-keV kinetic energy.

Shielded blue-cellophane film dosimeters were used on many of the low-pressure propagation shots to obtain time-integrated records of the beam radial profile at various axial locations in the drift tube. An example of the beam profile record obtained using this technique is shown in Fig. 18, Appendix B.

Thermoluminescent Dosimetry Lithium fluoride thermoluminescent dosimeters (TLDs) were on a limited number of shots to verify the beam current profiles measured with the subminiature Faraday cup array. Exposure of an array of dosimeters to the gamma dose produced by the beam striking a thick target provided a more quantitative record of the time-integrated beam profile than that produced by blue-cellophane film dosimetry because the linear response range of the blue-cellophane film was almost always exceeded for the high current density FX-100 beam.

Open Shutter Photography Time-integrated open-shutter photographs of the beam and ionized-channel excited air emission were obtained at viewing ports located at axial positions close to the diode (shown in Fig. 12) and 4.5-m from the diode. The symmetry properties of the drift tube were not disrupted by the ports because a return-current carrying screen was incorporated in each. The exposures with these cameras were recorded with Polaroid Type 58 (ASA 75 speed) color film.

Because of the overexposure resulting from weak, but persistent, light, and the time-integration of motion of the beam or channel or both, open-shutter photography must be thought of as an easily-fielded "early warning" diagnostic to identify effects that require further, more careful, spectral or temporal resolution. A discussion of many of the issues involved in interpretation of the data obtained in this experiment with optical emission diagnostics is contained in Appendix F.

A point not covered in that appendix is the following. As shown in the appendix, the excitation of the upper level of the radiative transitions by the low-energy plasma electrons is $\sim (kT_e)^{1/2} (1 + kT_e/E_0) \exp(-kT_e/E_0)$, where T_e is the temperature of the cold electrons, and E_0 is the threshold of the excitation cross-section, $E_0 \gg kT_e$. The radiation is, therefore, very sensitive to the population of the high-energy tail of the electron distribution. It is well known that high electric fields can significantly distort the tail of the distribution. For example, a modest E/p of about 100 V/cm/Torr can increase the effective temperature of the tail of the distribution by a factor of 5 or more. As a consequence, the visible emission can be vastly different from regions having the same gas temperature and plasma

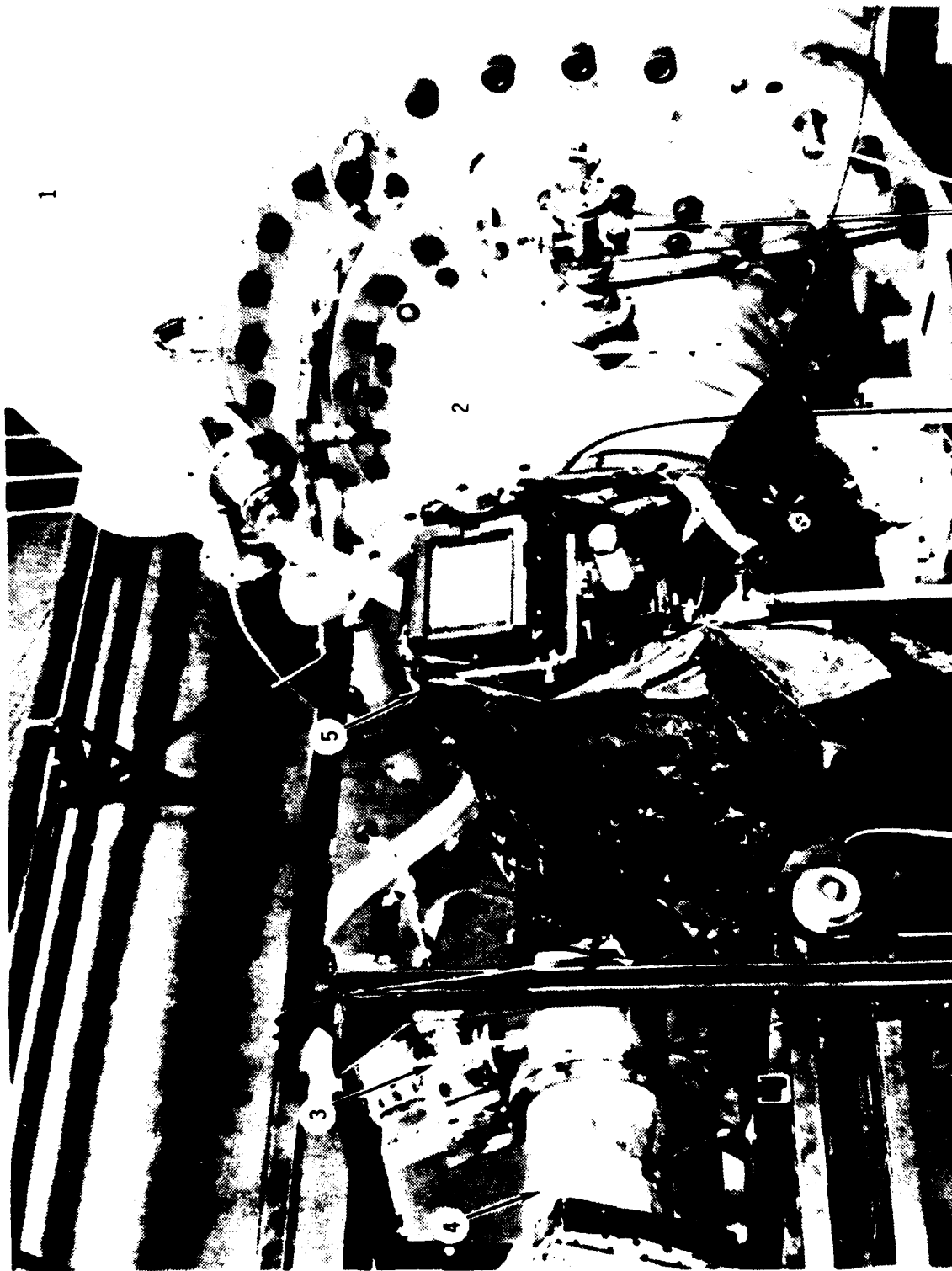


Figure 12. Open-shutter camera positioned at port closest to FX-100 diode. (1) FX-100 tank; (2) Vacuum transmission line; (3) Drift tube pumping manifold; (4) Drift tube; (5) Open-shutter camera.

electron density, but having different widely disparing values of E/p . This may be the cause of some of the more spectacular effects seen in both open-shutter and time-resolved photographs.

Examples of FX-100 open shutter photographs are shown in Fig. 19 and Fig. 24.

Fast Time-Resolved Photography An Imacon 790 image-converter camera on loan from Los Alamos National Laboratory was used to obtain streak and framing photographs of the emission from the beam and plasma channel. These observations were made through the same port at 4.5 m that was used for open-shutter photography on other shots. In order to record the head of the beam it was necessary to delay the light by folding the optical path and locating the Imacon camera next to the FX-100 output switch. The camera trigger was derived directly from the light from the FX-100 switch. This arrangement, shown in Fig. 13, provided sufficient delay of the beam light that the internal triggering delay of camera did not prevent recording the beam head. A 1200-mm Questar collection lens at the camera provided adequate magnification and light intensity that intermediate relay lenses were unnecessary. Streak photographs obtained with this system are shown in Fig. 17 and Fig. 18, and a framing sequence is shown in Fig. 23.

Spectroscopy Time-integrated spectra were obtained at a single pressure (0.35 Torr) using as a dispersing instrument a Jarell-Ash 1/2-m Fastie-Ebert spectrometer supplied by the AFWL. The grating used had 1200 grooves/mm and

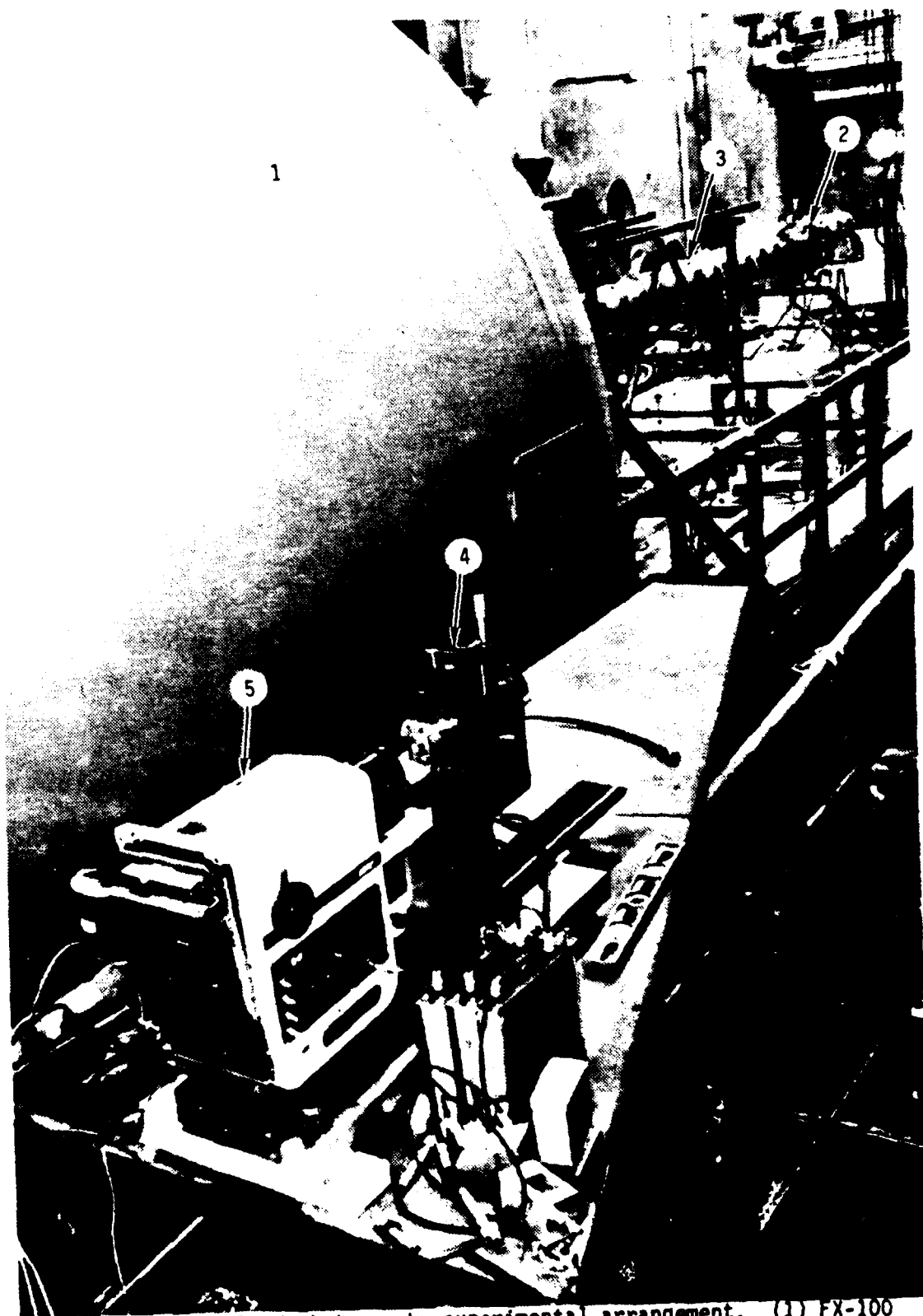


Figure 13. Time-resolved photography experimental arrangement. (1) FX-100 tank; (2) Beam viewing port and first turning mirror (final mirror is out of view); (3) Drift tube; (4) Questar 1200-mm f.l. optics; (5) Imacon 790 image converter camera.

was blazed at 5500 Å. A color-corrected 85-mm camera lens was used to image the beam channel on the input slit in order to provide spatial resolution of the emitted light. All spectra were obtained at the 4.5-m port position. The port material was acrylic, which limited the spectra to the wavelength range above ~3500 Å, although it is doubtful if the Polaroid Type 57 (ASA 3000 speed) film that we used would have had adequate sensitivity below this cutoff. An example of a densitometer scan of a spatially resolved, time-integrated spectrum obtained with this system is shown in Fig. 20.

6. Propagation Experiments

The FX-100 low-pressure air propagation experiments were performed in several different experimental runs, each with the specific diagnostics needed to address a limited set of particular issues. This strategy was necessary because of the limited number of data channels that were available for our use. Furthermore, the impending demise of the FX-100 generator was always foremost in our thinking, and in many cases we hurried through an experimental run more rapidly than we would have liked, in order that we could complete all the baseline measurements before the accelerator was decommissioned.

Our first set of experimental runs was designed to delineate the stable-propagation pressure window with carbon calorimetry, while at the same time accumulating measurements of the spatial current distribution with the charge-collector array. Other diagnostics fielded to provide corroboration of the current distribution included radiochromic-film dosimetry, TLD arrays, and openshutter photography. Because of our discovery of the unexpected "halo" of current surrounding the central beam, we devoted a number of shots to extensive

investigations into its cause. These included the use of a series of carbon collimators at the anode foil in order to eliminate the possibility that shank emission in the diode was causing the halo current. It was not.

Because the propagation pressure window is also delineated by a minimum in the net current,⁷ we devoted a limited number of shots to measurements of net and beam currents at various axial positions. The importance of the channel conductivity and the possibility of using visible light emitted to obtain information about this parameter led us to design an extensive series of runs devoted to optical diagnostics, for example, spectroscopy and time-resolved streak and framing photography. Finally, a limited test of a compact magnetic beta-spectrometer designed and constructed at Los Alamos Scientific Laboratory was made in order to test the feasibility of using this design in the second year low-pressure propagation experiments.

The diagnostics used and pressures surveyed in these experiments is tabulated in Appendix B. These experiments produced a large bank of data, all of which has not been fully analyzed. The analysis of these data continues as an ongoing project.

7. Simulations

Under a separate contract a linearized, three-dimensional, fully electromagnetic particle-in-cell code (KMRAD) was written to investigate resistive instabilities. KMRAD was used to predict instability growth and convention rates in the beam body for the parameters of the FX-100 experiments. Under yet another contract MRC developed a propagation code, CPROP, based on the two-dimensional, relativistic, electromagnetic, particle-in-cell beam

simulation code. CPROP is being used to investigate the physics of the hollowing instability, including the effects of nose blowoff at injection, ohmic energy losses, conductivity generation, and return current formation. This code treats blowoff, ohmic losses, beam hollowing, and return currents by direct self-consistent numerical integration of the Maxwell equations and the single particle relativistic equations of motion. Conductivity has been based on models developed at Lawrence Livermore National Laboratory. Improved models more appropriate for the low-pressure experiments at AFWL are now being developed at MRC for DARPA and will be added to CPROP in due course. Details of the comparisons between KMRAD and CPROP simulations and the experiments are to be found in Appendix E.

III. EXPERIMENTAL RESULTS AND DISCUSSION

In both the FX-25 and FX-100 experiments the energy deposited in a calorimeter at the end of the drift tube was used to define the propagation window in pressure. This measurement integrates over both particle energy and current and is not necessarily indicative of electron kinetic energy loss. For example, we found in our experiments that the low and high pressure limits of the propagation window were largely determined by loss of particles from the beam, rather than by beam-electron kinetic energy loss. In Fig. 14 is shown the beam-current density measured on axis at the end of the FX-25 drift tube at different pressures. Here one can clearly see the definition of the propagation window at high pressures through the loss of the beam tail, and at low pressures through the erosion of the beam head. The current history measured at the diode can be overlaid on these data as an envelope, but has been omitted for clarity. It is also evident that there is a regime of pressure in which both nose-erosion and tail-loss are simultaneously limiting the beam charge transport through the 3-m drift tube. The propagation window for the FX-100 is shown in Fig. 15. Two measurements of net current for pressures on either side of the window "center" for the FX-100 beam are shown in Fig. 16. It appears that nose-erosion was not so significant for this beam as for the FX-25, however, it must be remembered that the FX-100 pulsewidth was ~6 times that of the FX-25 to begin with, and, therefore, the loss of calorimetrically measured transported energy resulting from equivalent erosion of transported charge would not be so large a fraction of the total in the FX-100 experiments as in the FX-25 experiments. The fact that erosion of the FX-100 beam did not play so large a role as for the FX-25 beam resulted in the

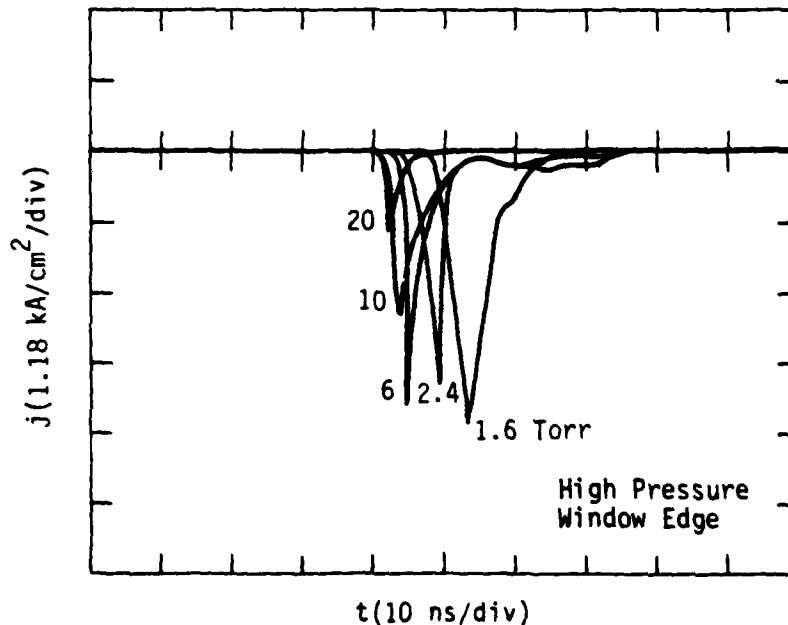
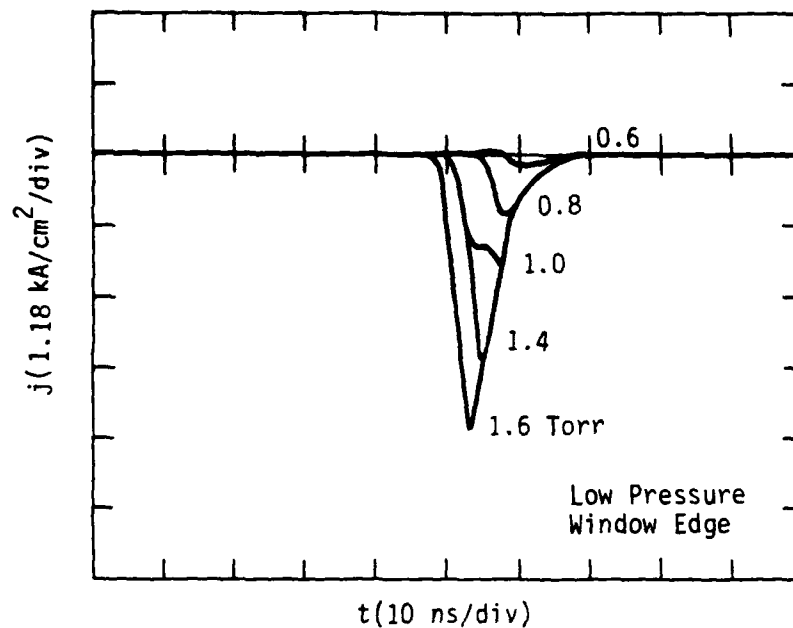


Figure 14. FX-25 beam current density on axis for different pressures. Maximum energy transport was at 1.6 Torr. The current density near the diode had a waveform that approximated the envelope of these signals. The erosion of the beam nose is clearly evident at pressures below 1.6 Torr (upper). At higher pressures both nose erosion and tail loss resulting from hosing are evident (lower).

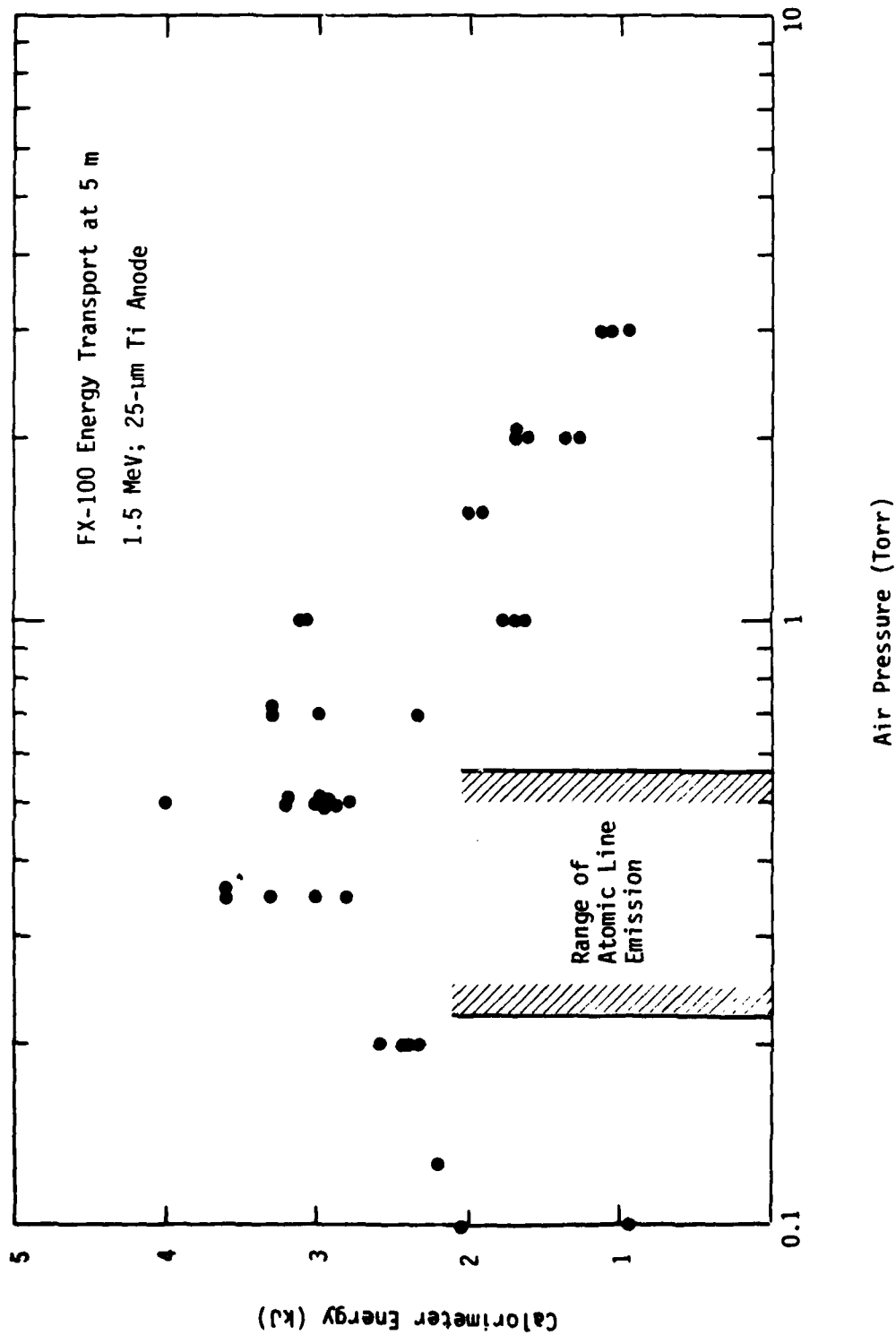


Figure 15. FX-100 propagation window in air for 5-m propagation length. In the range indicated there was intense emission of atomic line radiation as well as the characteristic molecular band emission.

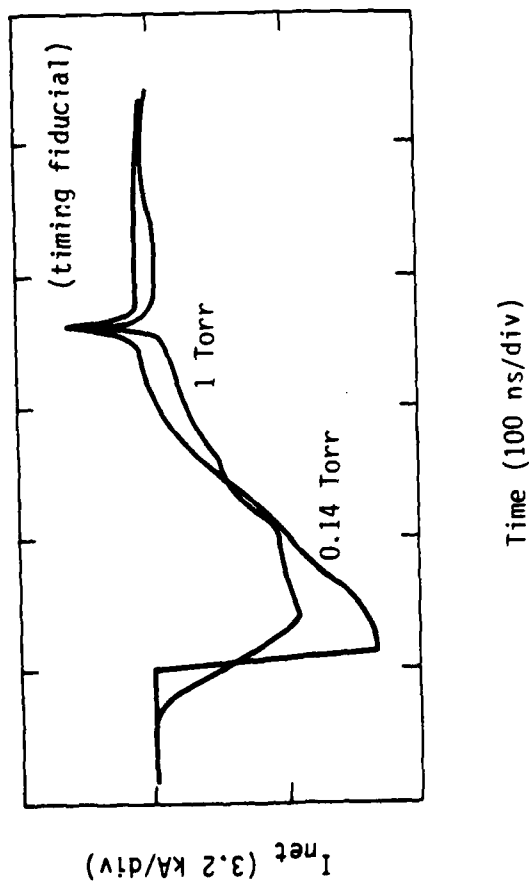


Figure 16. Net current measured in FX-100 propagation experiments at high and low air pressures in the propagation window. The pulse sharpening seen at pressures lower than that for maximum energy transport (0.5 Torr) is thought to result from rapid loss of the beam front and subsequent slow erosion.

comparatively gentle decrease on the low-energy side of the window. The erosion of the beam head can be seen in streak photographs taken at pressures lower than the window center. These are shown in Fig. 17. In Fig. 18 we show streak photographs taken at pressures on the high side of the window, and here it is clearly seen that the loss of the beam tail is the result of hosing of the beam into the wall prior to its reaching the observation port at 4.5 m. Note especially that the hose in Fig. 18 (b) appears to be convective, and that in Fig. 18 (c) a piece of the beam has been detached from the head by the extreme motion of the hose. We should emphasize that we always detected a small piece of the beam head transported to the end of the tube even in the presence of the most violent hosing at pressures in excess of 20 Torr. A small piece of the beam head propagating significant distances on axis has apparently been observed in full-density air-propagation experiments^{8,9} on large accelerators, and there was some circumstantial evidence for this in our full-density FX-25 experiments. This was true for both FX experiments, and may indicate the convective character of the hose instability at these experimental parameters. It should be mentioned that this effect has been observed in many prior propagation experiments.^{7,8,9}

In the FX-100 experiments the pressure window for propagation was also delineated by vivid displays of visible emission as is illustrated by the open-shutter photographs in Fig. 19. Spatially resolved spectral measurements of the light emitted showed that in a concentrated region near the axis much of the emission was from dissociated and ionized nitrogen (Fig. 20). Because it requires ~24 eV to form this species, we infer a high energy density for the ionized gas on axis. The radial extent of the high energy region is much less

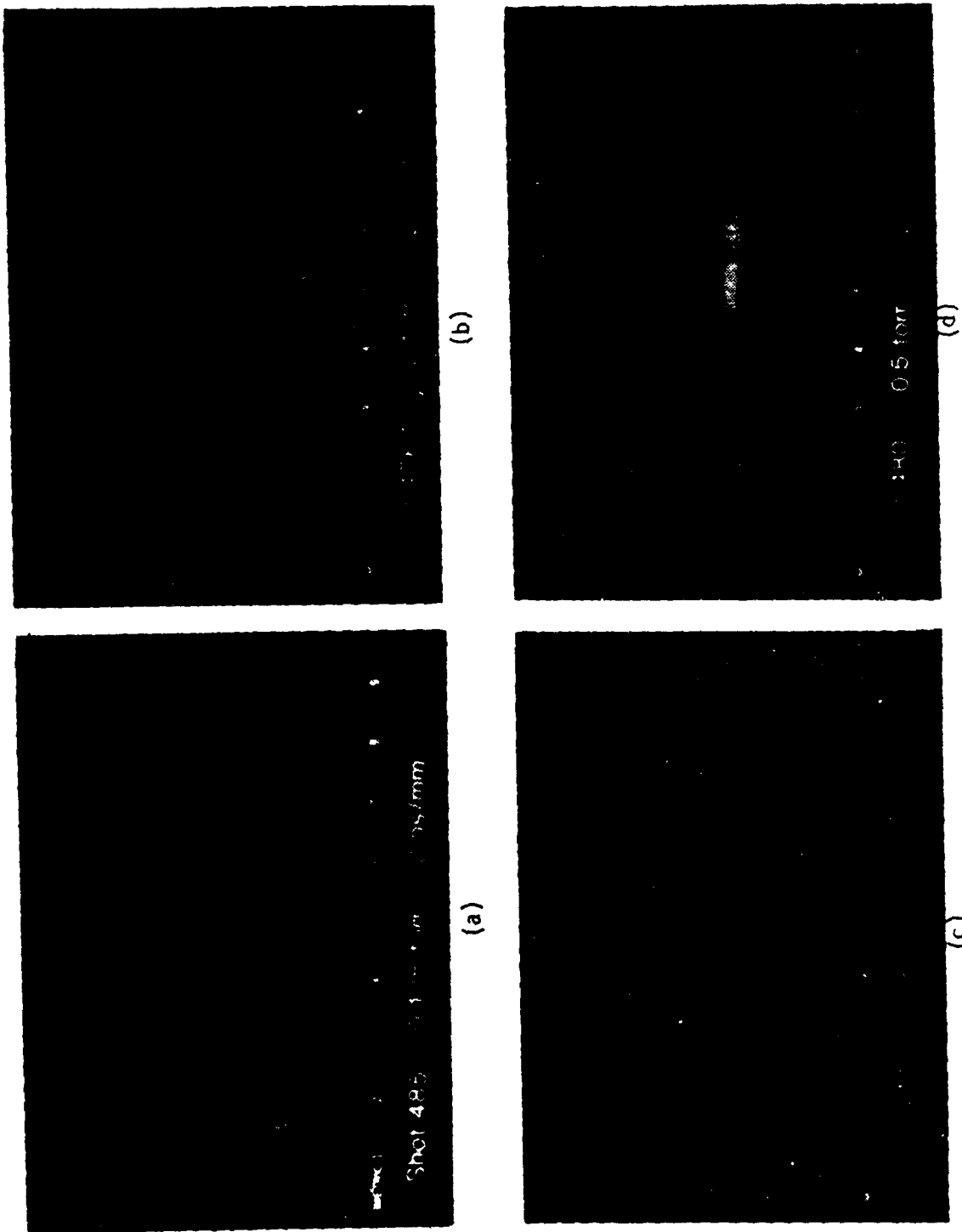
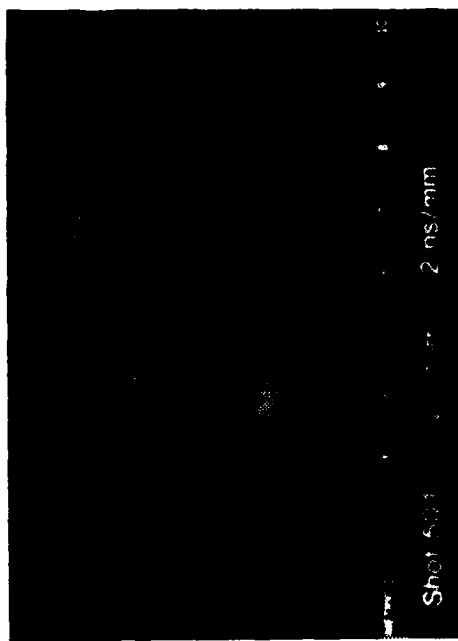
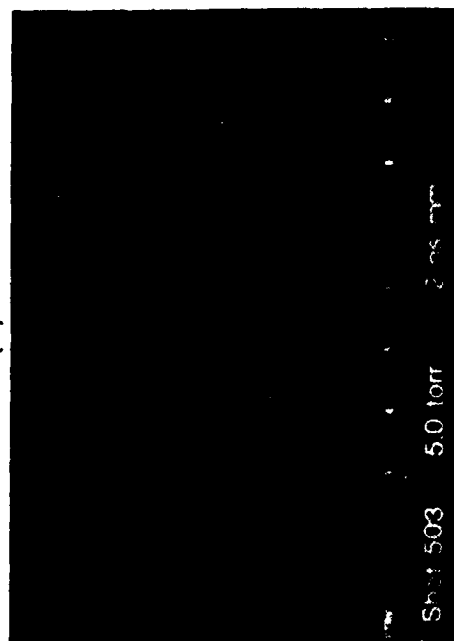


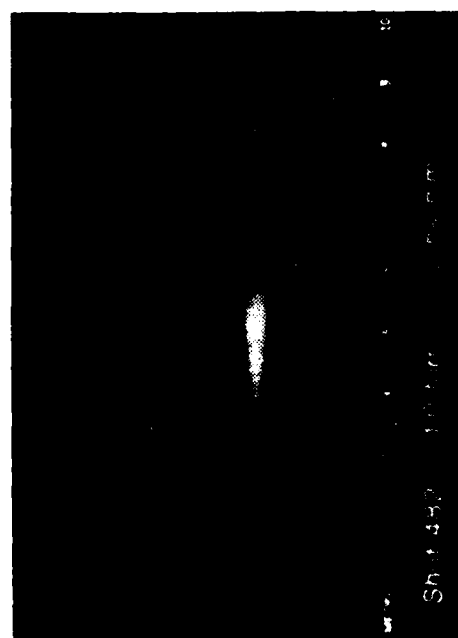
Figure 17. Streak-camera photographs of the beam-excited air emission at $Z = 4.5\text{-m}$ as pressure is increased from below the propagation pressure window (a) to the center of the window (d). (Ignore the image converter-tube blemish in the far left of each photograph.) The beam head is at the left of each streak (taken through a vertical slit). The delay in start of emission in (a) as compared with (d) is presumably the result of erosion at lower pressures.



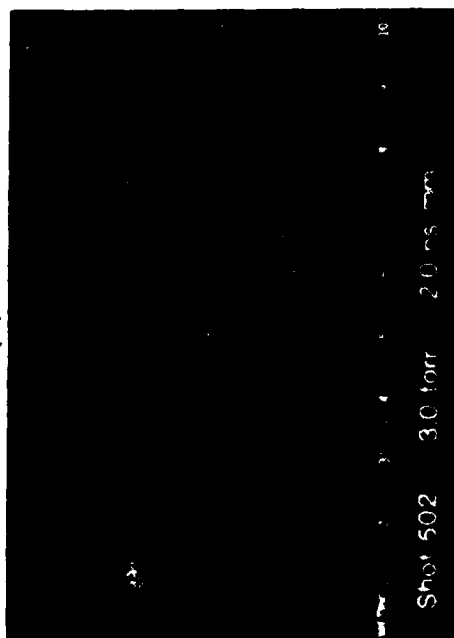
(a)



(b)



(c)




(d)

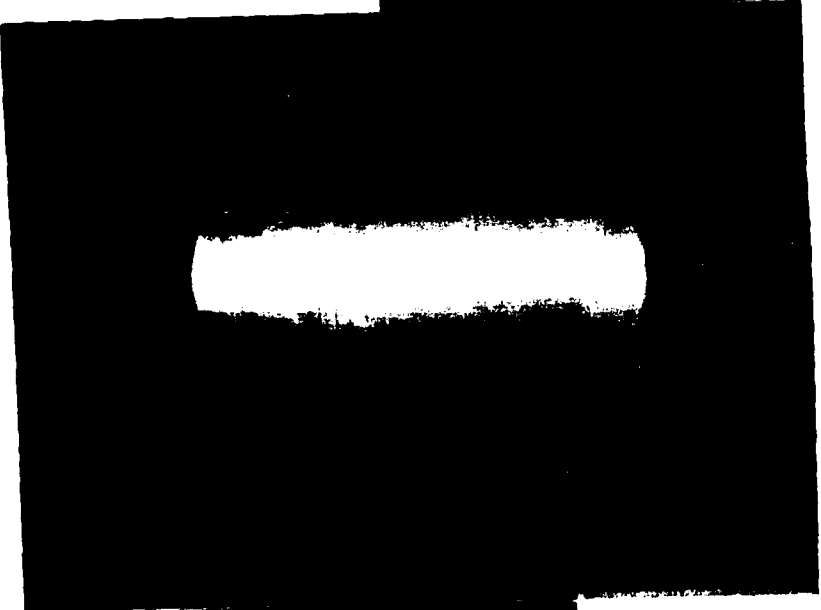
Figure 18. Streak-camera photographs of the FX-100 beam at 4.5-m as air pressure is increased above the propagation window showing loss of the tail of the beam. Figures (b) and (c) show especially clear evidence of hosing in the tail.

Figure 19. FX-100 open-shutter photographs at $Z = 4.5$ m and pressures spanning the propagation window showing the molecular band emission at high and low pressures and atomic (O) line emission at intermediate pressures. (Beam propagating left to right, circular aperture 17.5 cm diameter). Note the apparent annular halo of emission surrounding the beam.

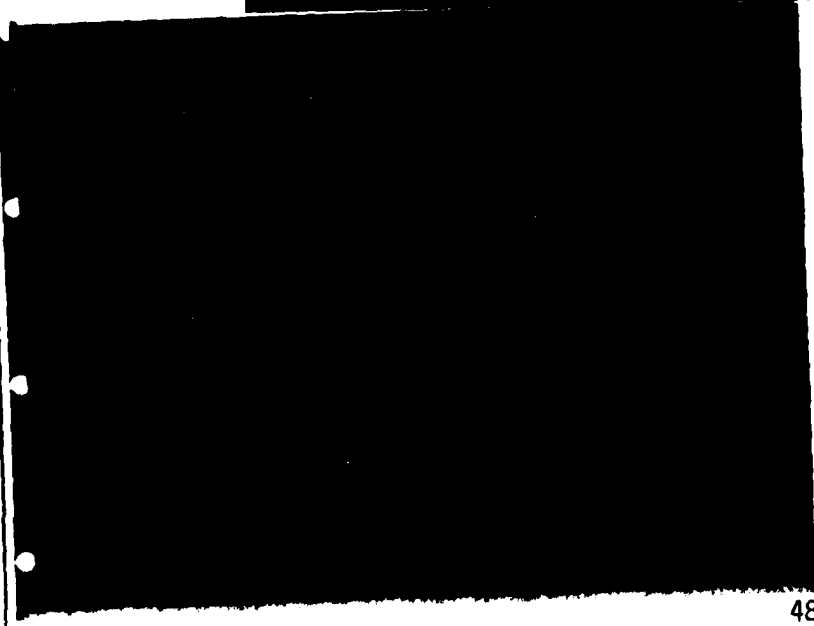
0.7 Torr



0.25 Torr



0.13 Torr



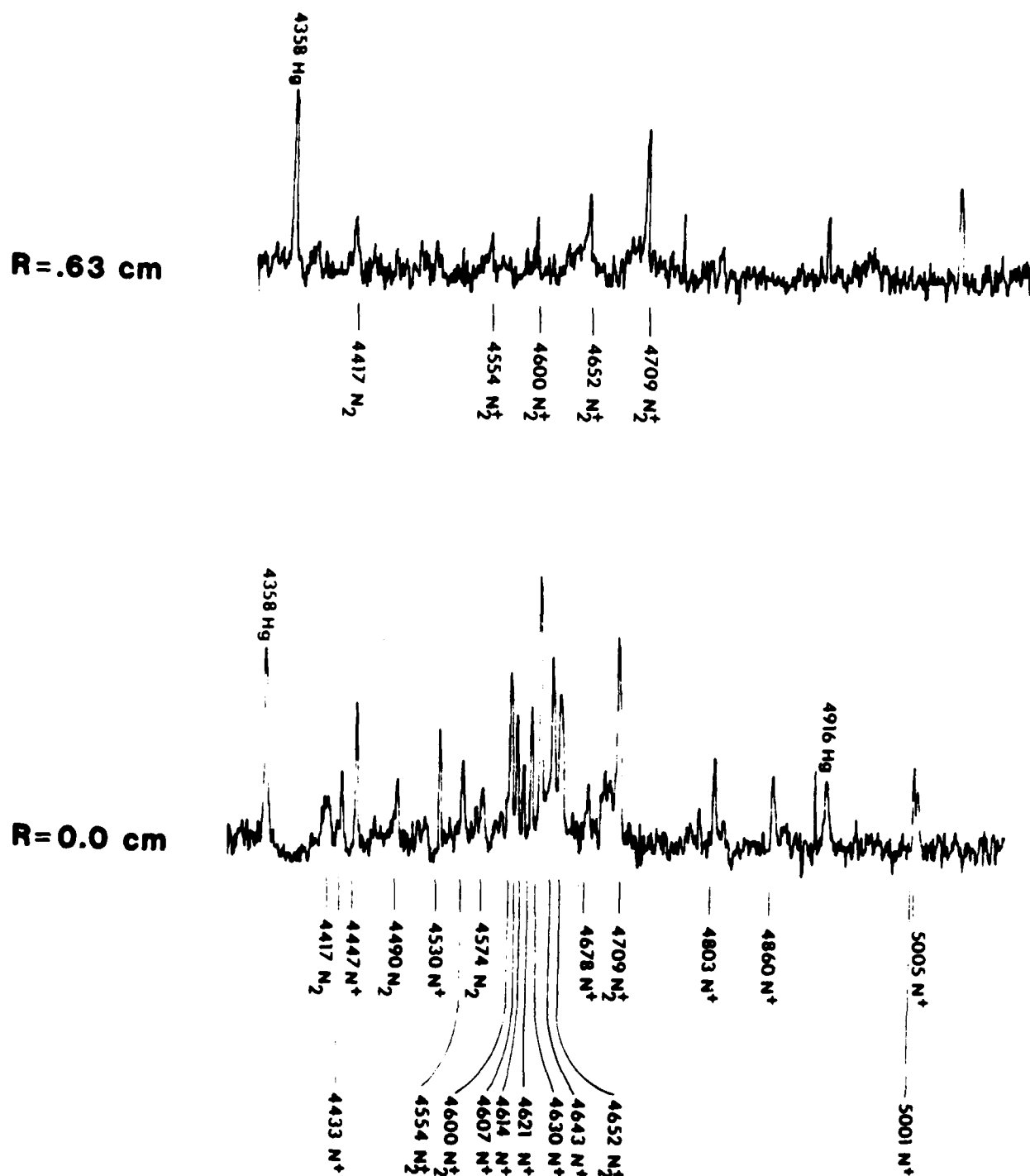


Figure 20. Atomic emission observed in the propagation window ($p = 0.35 \text{ Torr}$) is confined to region near the beam axis well inside of the beam Bennett radius ($a \sim 3 \text{ cm}$).

than the radius characteristic of the Bennett-like beam current profile ($a \sim 3$ cm). Although these spectra do not constitute a direct measurement of the channel conductivity, they are suggestive of a hotter and hence more highly-ionized and conductive gas on the axis.

The propagation window was also characterized by the appearance of a virulent azimuthally symmetric instability that caused a large fraction of the beam current to be expelled from the central channel into an annular "halo" region. This thin shell of current then propagated with the residue of the central core to the end of the drift tube. This phenomenon was observed with radiochromic foils, open-shutter photography, streak photography, and our array of fast-risetime subminiature charge collectors. The radiochromic (blue cellophane) film measurements were made with 125- μ m titanium foils shielding the film from exposure to any electrons with kinetic energy below ~ 180 keV. The same titanium foil thickness was used to shield the array of charge collectors. A time and space resolved plot of the current density at a distance less than 1 m from the diode is shown in Fig. 21. The data plotted in this figure clearly show the evolution of the annular shell at a time late in the beam pulse. An example of a radiochromic film exposure can be seen in Fig. 18 Appendix D. Many other examples of the time history of the spatial distribution of current associated with this thin-shell hollowing instability can be found throughout the appendices. The hollow current carrying shell is also evident in both time-integrated and time-resolved photographs. It is seen in the open-shutter photograph in Fig. 19 that was taken at 0.25 Torr and in the photograph taken at 0.7 Torr. Figure 22 is a streak photograph showing a well developed shell of current. The open shutter photographs show other

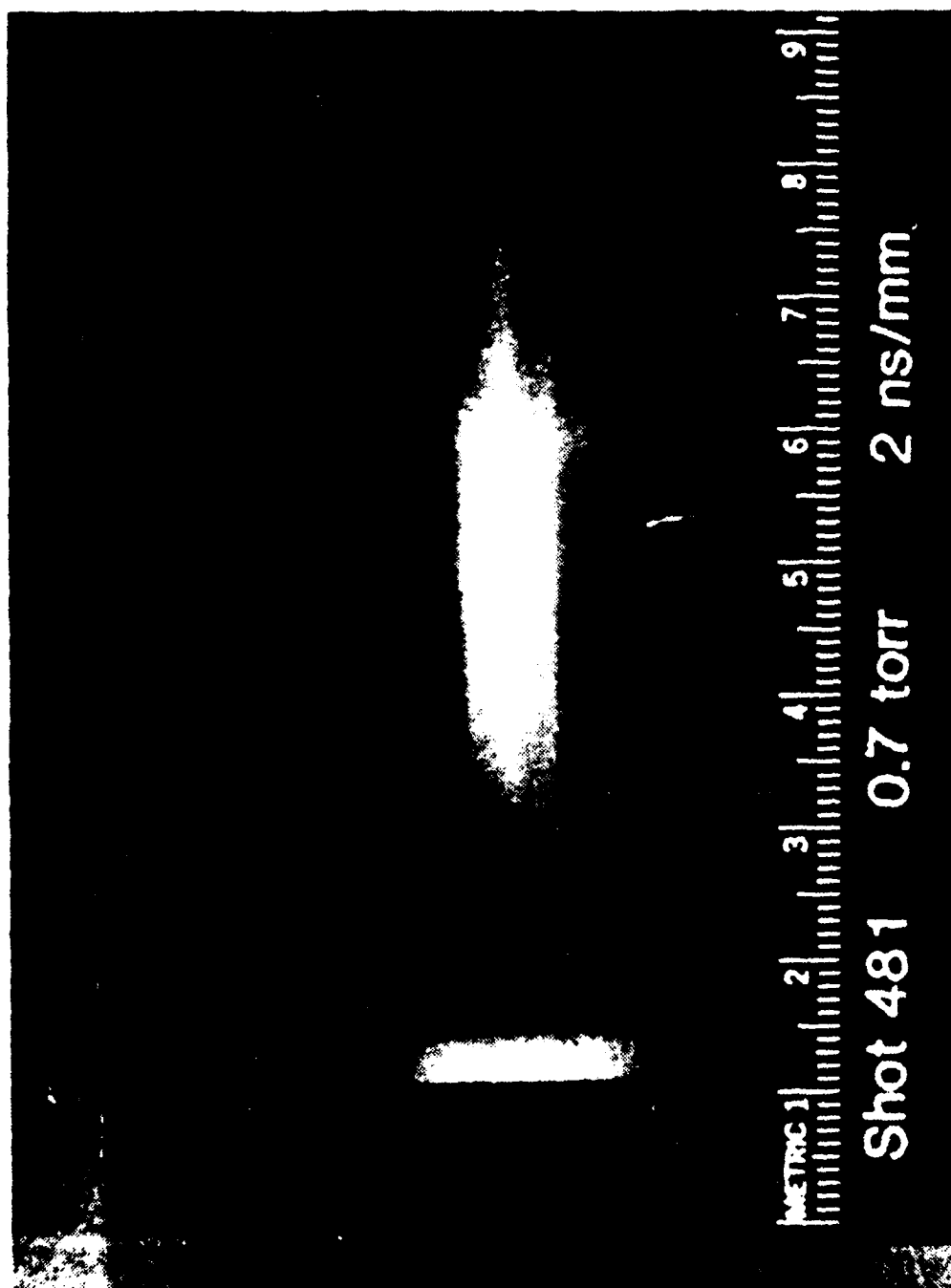


Figure 22. Imacon streak-camera picture taken through a vertical slit at 4.5 m showing emission from fully developed annular halo.

rather spectacular effects in addition to the hollowing. It is of interest to resolve these in time to try to understand their causes. In particular, the intense atomic emission concentrated near the axis persists for very long times after the passage of the beam, as seen from the framing camera sequence in Fig. 23. The time integration of this afterglow radiation accounts for the "hot spots" seen in the open shutter pictures. The most likely explanation for the persistence of this afterglow radiation is the extremely slow deionization rates for the ionized atomic nitrogen in the central core. Also evident in Fig. 23 is the apparent formation of the "streamers" during the latter part of the beam pulse. Additional observations about the streamers are that they always open in the direction of beam propagation, as if they were ejected from the channel by primaries, and the opening angle is more acute near the diode. These might be particle tracks "exposed" by the high E/p environment, they could be instabilities in the beam, or they could be low-energy electron exposures of electromagnetic-field effects. Which of these, or other, causes is responsible for the vivid streamer displays is highly speculative at this juncture. The streamers may be masked at earlier times by direct beam excited emission, but on the basis of these photographs one cannot be certain that they are not formed during the switching off of the space-charge neutralized beam current, which may lead to pinching of the remaining unbalanced charge channel.

The appearance of a thin-shell hollowing instability in the pressure regime where avalanching provides an important contribution to the conductivity, which may have a profile more peaked than the beam, and where the current is highly neutralized is in qualitative agreement with existing theory and simulations. However, the >20 -ns delay into the beam pulse before the

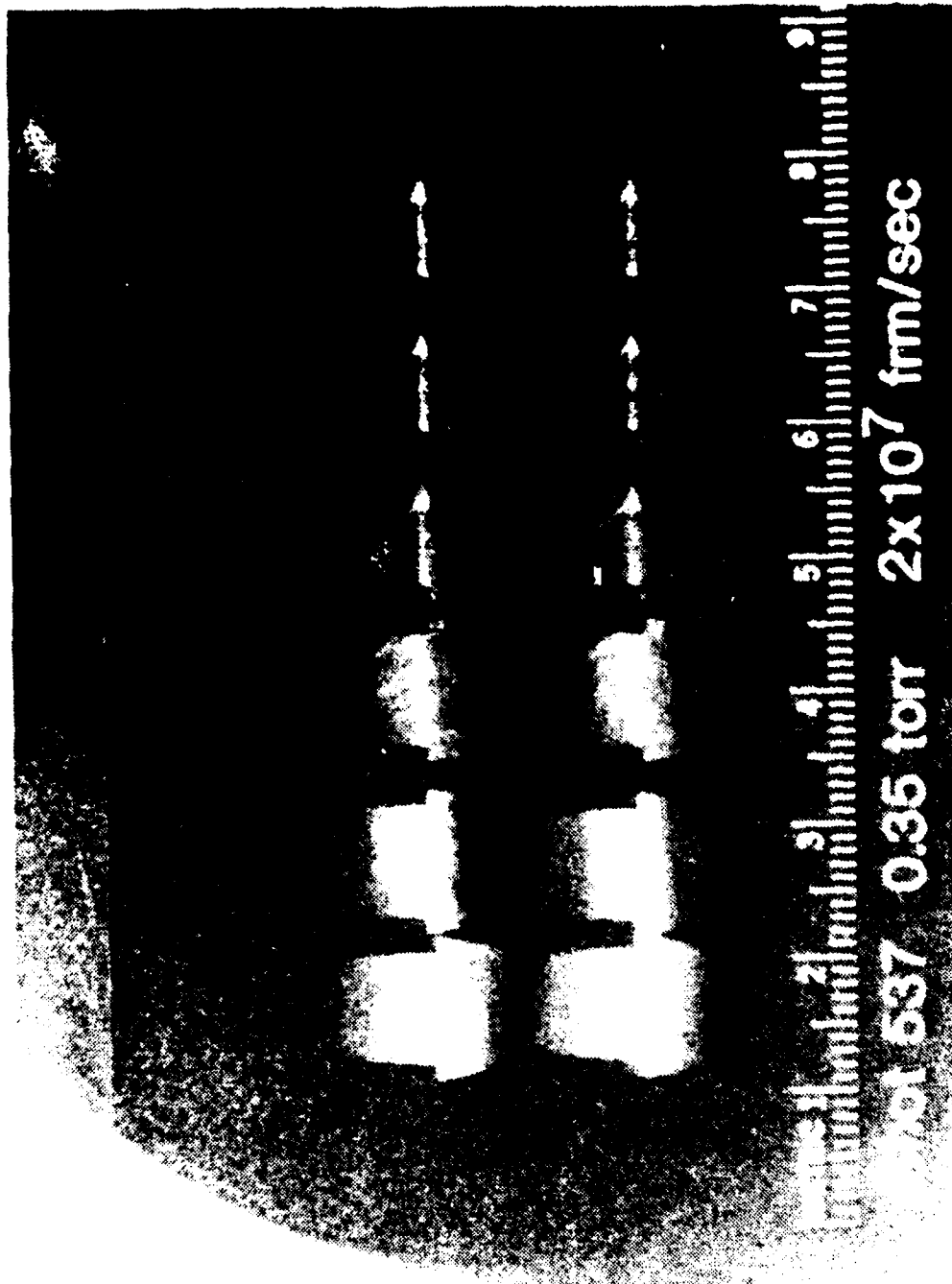
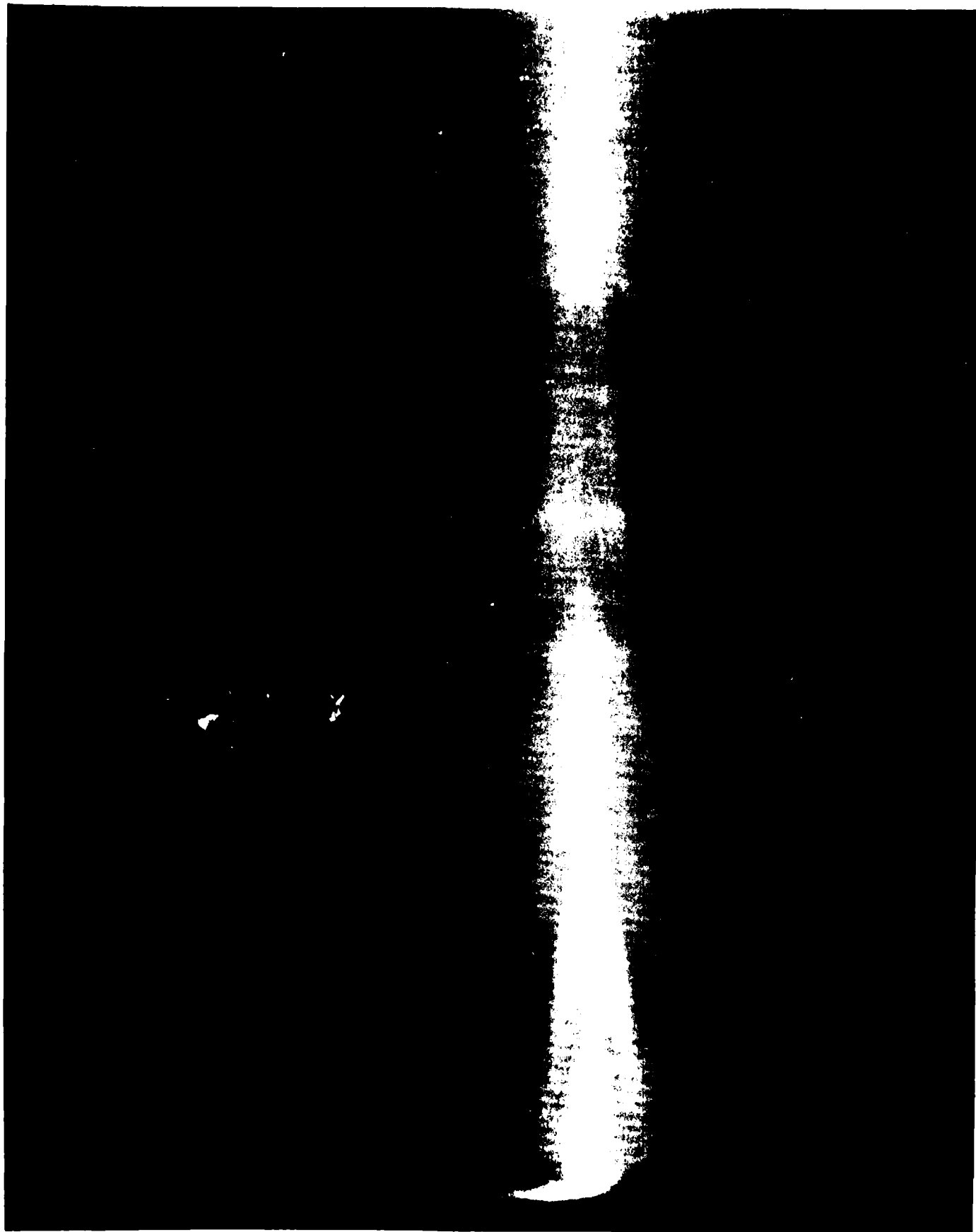


Figure 23. Framing-camera photograph of FX-100 beam at $Z = 4.5\text{-m}$. The exposure time for each frame is 10 ns. This shows the apparent development of a hollowing instability late in the beam pulse, and the persistence of the emission on axis, compared with the rapidly quenched emission from the beam body.

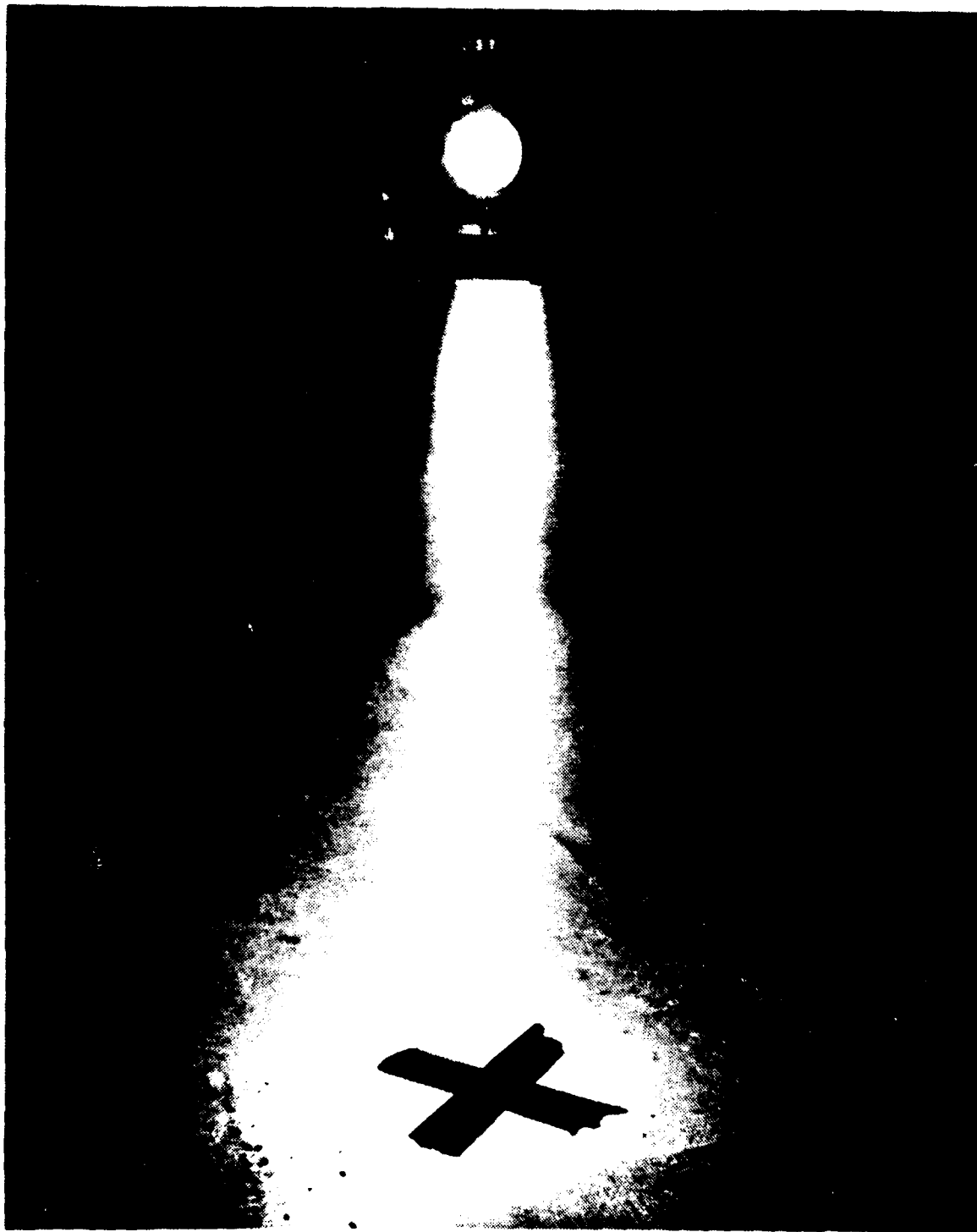
Figure 24. Open-shutter photograph at $Z \sim 10$ -cm from the diode at air pressures near the peak of the propagation window. This clearly shows the initial ejection of current from the main channel to form the current halo. (Beam propagating right to left, clear aperture length ~ 24 -cm.)



instability onset is not clear. It may be that this is simply the delay for the conductivity to form the required profile for instability, or the result of a pathological change in the diode characteristics late in the pulse.

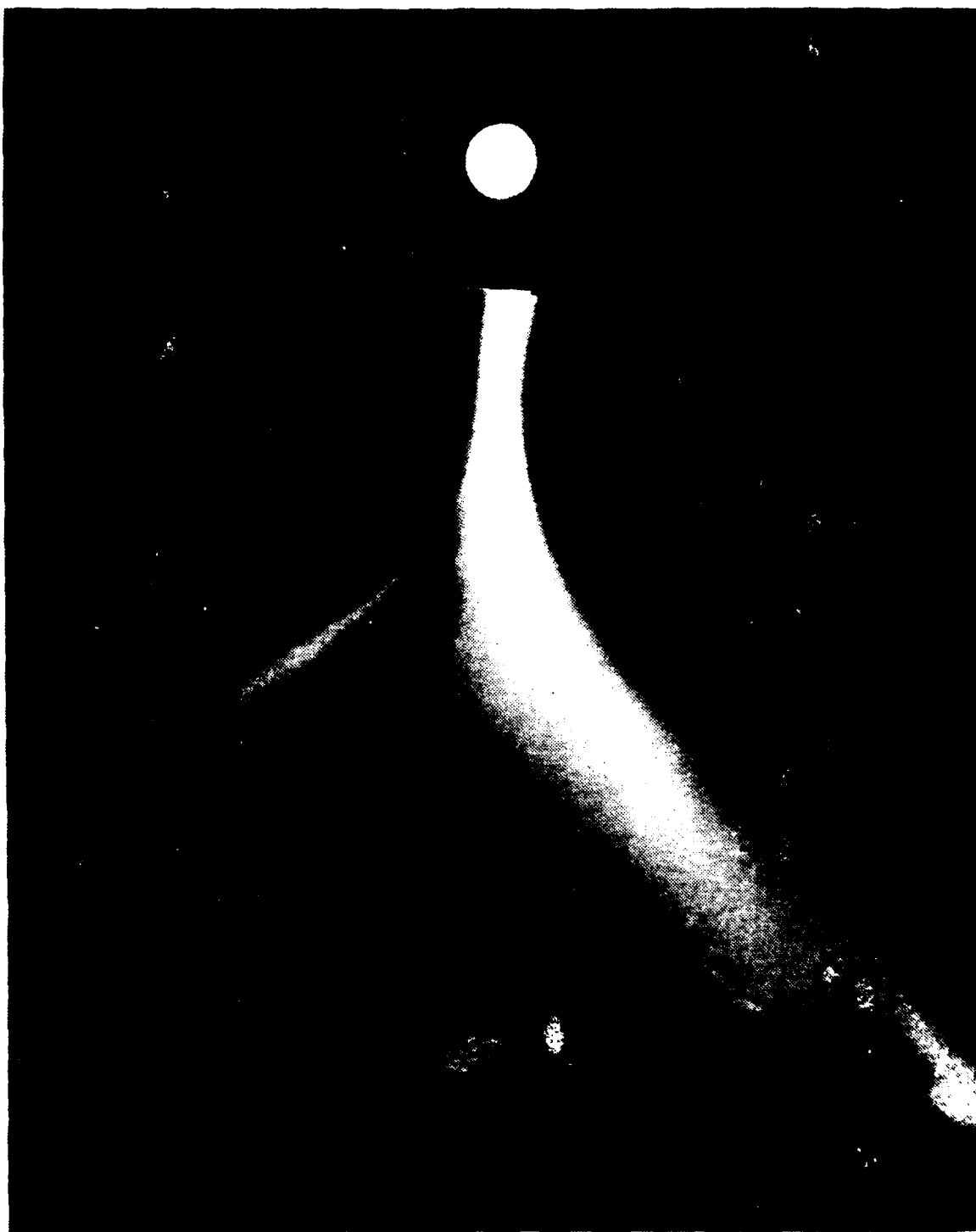
Finally, a word about our FX-25 beam extraction experiments is in order. A marked threshold for the stabilization of the full-density-air hose instability was observed when the preparation cell pressure was reduced below 1 Torr. Because there appeared to be no associated threshold in the erosion-caused pulse sharpening in the drift tube, it is unlikely that this was the dominant mechanism for stabilization, although it may be a necessary ingredient. The same may be said for phase-mixed damping of initial oscillations that are shock-excited at the diode. The probable reason for the threshold is the matching of λ_g inside the cell and just outside of the extraction foil in full-density air. This implies matching both the beam radius and net current. Our diagnostics were insufficient to provide conclusive evidence for matching at the stabilization threshold in this limited set of exploratory tests of the use of a beam conditioning cell. The effect is shown in the open shutter photographs in Fig. 25 (3-Torr in preparation cell), and Fig. 26 (0.6-Torr in preparation cell). Note that even when violently unstable in Fig. 25, there is evidence for a part of the beam transporting straight to the wall (as indicated by the fluorescence of the wall on axis). In Fig. 26 the stable propagation length is limited by the wall to about 5 or 6 betatron wavelengths. These experiments show that there is great promise for the use of the preparation cell technique for providing greater control of the beam stability properties.

Figure 25. Open-shutter photograph of the FX-25 beam extracted into full-density air (630 Torr) through a 25 μ m Kapton foil after drifting through 3-m of 3-Torr air.



Open shutter photograph of the FX-25 beam extracted into full-density air after drifting through 3-m of 3-Torr air.

Figure 26. Open-shutter photograph of the FX-25 beam extracted into full density air after drifting through 3-m of 0.6-Torr air.



Open shutter photograph of the FX-25 beam extracted into full density air after drifting through 3-m of 0.6-Torr air.

IV. PLANS FOR FUTURE EXPERIMENTS

The FX-100 and FX-25 accelerators, on which the first year experiments were performed, have been decommissioned. In order to continue the propagation experiments a new laboratory facility has been organized at the AFWL. The heart of this new laboratory is the VISHNU accelerator described in the following few paragraphs. Once VISHNU is fully operational, a minimal number of measurements to establish the low-pressure propagation window and current distribution will be made. These should proceed rapidly because of our accumulated experience with the FX-100 and FX-25 beams. Once this has been completed, we will proceed to a more comprehensive characterization of the hose and sausage instabilities at various pressures.

1. VISHNU Accelerator

VISHNU is an intense relativistic electron beam generator that is under construction at the AFWL from the components of a decommissioned Pulse Rad 4-15 generator. In its initial incarnation VISHNU has a 16 stage Marx generator that could store a maximum of 8 kJ if each stage were charged to the maximum rating of 100 kV. In practice, we will only charge to ~80% of this maximum rating in order to extend the lifetime of the components (eg., the number of capacitor discharge cycles prior to failure is roughly proportional to the seventh power of the charging voltage). When erected, the VISHNU Marx generator pulse charges a 10- Ω oil-insulated coaxial transmission line, which has a (one-way) electrical length of ~13 ns, and a capacitance small compared with the Marx generator. The calculated ringing gain for this line is ~1.7, and it would be charged to ~2.7 MV with the maximum voltage on the Marx. The

oil insulation would be severely overstressed at this voltage, however, and consequently we intend to set the untriggered single-channel oil output switch to self break when the voltage reaches 90% of the ring-up for an 80% Marx charge. This gives the oil line a 1.9 MV charge, which will produce a 0.9-MV, 90-kA, 26-ns pulse into a matched load. A field-emitting diode with these parameters would produce a highly pinched beam, and, furthermore, we wish to perform our propagation experiments with a higher kinetic energy beam having parameters close to those of our past experiments on the FX machines. Therefore, we will attempt to mismatch the diode to obtain a 1.5-MeV, 40-kA, 26-ns electron beam output.

The VISHNU diode could, of course, be designed to provide other beam parameters within the constraints of the 10- Ω generator load-line and diode pinching. The region of beam kinetic energy and current accessible by VISHNU is shown in Fig. 27 for comparison with other accelerators that are being used or planned for intense electron-beam air-propagation experiments.

At the time that MRC became involved in the VISHNU project, a number of modifications were required to make VISHNU into an operating machine. The principal task that we undertook was the design of a new oil-vacuum interface/high-voltage insulator (or diode envelope). Other tasks included the design of an adapter plate between the Marx generator tank and the pulse-line, the design of new supports for the pulse-line inner conductor, and guidance in the design of the field emitting cathode.

Design of the envelope was complicated by the temporary loss of the switch housing from the old Pulse Rad 4-15. The envelope is a conventional insulator stack with 14 angled and graded plastic rings. The metal grading rings were

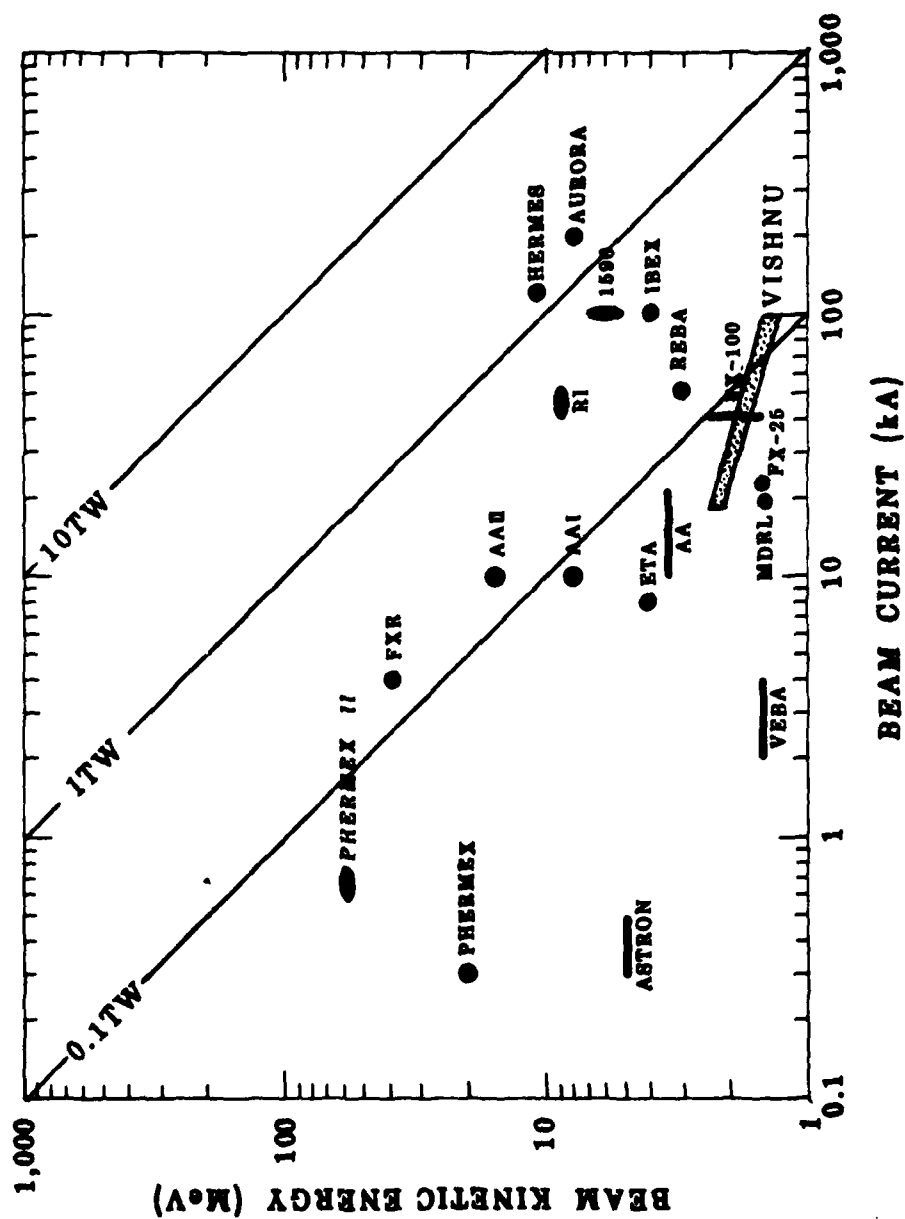


Figure 27. Intense electron beam accelerators available for air propagation experiments. Also shown are several upgrades and accelerators under development. The entire available range of current and voltage of the AFWL VISHNU accelerator is shown.

spares originally fabricated for the RADLAC accelerator, and their availability dictated the envelope diameter. Similar structures are rated at ~ 125 kV/cm, and in principle, the VISHNU envelope could be used for an output as high as ~ 4.5 MV. However, in practice non-uniform fields limit the usable gradient. The voltage standoff capability will be further limited by electron bombardment of the insulators, which may lead to flashover. Experimental data from the RADLAC accelerator program indicates that in the presence of currents, insulator breakdown is time dependent, and the VISHNU envelope may break down at ~ 2.5 MV.

A major problem with the present design is that the limited space available for the output oil switch increased the capacitive coupling between the pulseline and the diode. This capacitance is ~ 25 pF and that of the envelope transmission line is between 25 pF and 38 pF. For the 1.9 MV pulseline charging voltage the resulting capacitive coupling can be expected to give a prepulse of 0.7-1.0 MV. This rather large value would certainly cause the graphite cathode to emit, consequently an effort has been made to suppress the prepulse through the use of a dielectric-flashover switch in the vacuum transmission-line center conductor. This should lower the prepulse at the cathode to less than ~ 50 kV. Furthermore, a comparatively small prepulse leakage current of ~ 500 A would reduce the prepulse by a factor of ~ 8 . If it turns out that the prepulse is unacceptably large, a 2-k Ω shunt resistor may solve the problem. Other solutions include the use of a groundplane shield in the oil switch.

Another problem we may face is that the single-channel oil switch and high-impedance vacuum transmission line output can be expected to result in a risetime longer than ~ 10 ns. If this causes a serious degradation of the short, ~ 25 -ns, pulse produced by the oil insulated coax we may need to resort to a lower impedance switch or output.

The diode envelope is supported by tie rods fabricated from "Superstud CR", a new high-strength glass-fibre reinforced polyester manufactured by Permal Corp. Other features of the design include an adjustable cathode shank, and a switch gap that is adjustable from the vacuum side of the envelope. Finally, access ports have been provided for the placement of capacitive V-dot voltage monitors on the oil side of the envelope, and for B-dot current monitors on the output transmission line.

When fully operational, VISHNU will be a versatile and reliable accelerator for the production of the electron beams required for the completion of our second year propagation experiments.

2. Beam Conditioning Cell

It seems clear from the results of the FX-100 experiments that any diode-generated beam will not be in equilibrium when injected into the air-propagation experimental chamber. This makes for poor reproducibility and lack of control of the beam behavior through the variation of external parameters (ie., air pressure, return-conductor radius, etc.). Because our second year research objectives require a much more precise control of the beam characteristics than we feel is obtainable with direct diode injection into the chamber, we will attempt to precondition the beam by equilibrating it in a short conditioning cell. This is based in part on our FX-25 experiments with

the stabilization of the full-density-air hose instability by the use of a conditioning cell. We intend to use helium gas in this cell because of its reduced scattering and simpler chemistry.

3. Propagation Chamber

Several large-diameter chambers have been located at the AFWL, and we have set these aside for use as a large diameter ($r > 60$ cm) propagation chamber in order to avoid unwanted wall effects. These have large viewing ports that will allow us to observe a significant beam propagation length without impediment. It will be a simple matter to use conducting-screen tubes with varying diameters in this chamber to investigate wall effects on hose growth, nose erosion, and coupling. We will also be able to explore the thin-shell hollowing instability in the absence of return conductors, if indeed this mode is observed in experiments with the shorter-pulse VISHNU beam.

V. SUMMARY

In summary, we have accomplished our first year objectives of delineating the pressure window for propagation of the FX-100 beam, of measuring the temporal evolution of the spatially resolved beam current distribution, and of providing insight into the experimental results through strong theoretical support.

We utilized available experimental time on the FX-25 to develop the subminiature charge collector diagnostic that was to prove invaluable in the following FX-100 experiments. We also used the FX-25 to perform experiments on

the stabilization of the full-density-air hose through the use of a low-pressure beam-preparation cell. The encouraging results of this exploratory use of a preparation cell will enable us to exercise greater control over the beam in future experiments.

Maximum energy transport of the FX-100 beam occurred at 0.3-0.5-Torr air pressure. The window for maximum energy transport was defined by loss of the tail of the beam at high pressures and by erosion of the beam head at low pressures in both the FX-25 and FX-100 experiments. Propagation in the window was characterized by a high degree of current neutralization (~80% or more). In the propagation pressure window we observed a strong hollowing instability. The hollowing caused as much as 80% of the beam current to be carried in a thin annular shell at a radius about twice the Bennett radius that characterized the injected current distribution. Space- and time-resolved measurements of the current distribution with a fast-risetime subminiature charge collector array showed that the thin-shell hollowing instability developed late (~20 ns or more) into the beam pulse. Spectroscopic measurements of the visible emission suggest that the air near the axis of the beam may have been hotter and more highly ionized in this pressure regime, which may have resulted in a conductivity profile more centrally concentrated than that of the beam.

The appearance of a thin-shell hollowing instability in the pressure regime where avalanching provides an important contribution to the conductivity, which may have a profile more peaked than the beam, and where the current is highly neutralized is in qualitative agreement with existing theory and simulations. The observed delay in onset is not. The source of the disagreement may lie in imperfect air-chemistry modelling giving an erroneous

delay for the buildup of an unstable conductivity profile. Simulations with CPROP showed many features consistent with the experimental results, including a high degree of current neutralization, rapid blowoff of the beam head after injection followed by slower erosion, and a lack of instability early in the beam pulse. Simulations with KMRAD showed instability to thin-shell hollowing in the body of the beam.

The experimental low-pressure air propagation experiments will be continued using the electron beam produced by a new accelerator (VISHNU) being constructed at the Air Force Weapons Laboratory. VISHNU is designed to have electron beam parameters close to those of the FX accelerators in order to take advantage of our experience with those beams. It will, however, have a shorter pulsewidth than the FX-100, which may have an effect on the onset of the hollowing instability.

VI. REFERENCES

1. C. A. Ekdahl, Rev. Sci. Instrum. 51, 1645(1980) and references therein.
2. G. E. Leavit, J. D. Shipman, Jr., and L. M. Vitkovitsky, Rev. Sci. Instrum. 36, 1371 (1965).
3. N. W. Harris, Rev. Sci. Instr. 45, 961 (1974).
4. W. Rogowski and W. Steinhaus, Arch. Elektrotech. 1, 141(1912).
5. D. Honea and S. S. Medley, J. Phys. E. 7, 537(1974).
6. P. Gehringer, E. Proksch, and H. Eschweiler, Int. J. Appl. Radiat. Isot. 33, 27(1982) and references therein.
7. T. J. Fessenden, R. J. Briggs, J. C. Clark, E. J. Lauer, and D. O. Trimble, Lawrence Livermore Laboratory Report UCID-17840, 1978.
8. R. B. Miller, private communication.
9. M. C. Clark, private communication.

VIII. ACKNOWLEDGEMENTS

This research was sponsored by the Air Force Office of Scientific Research (AFSC) under contract F49620-81-C-0016, monitored by Lt. Col. Anthony Hyder. One of the authors (W. Bostick) was a senior research physicist in the University of Residency Program at the Air Force Weapons Laboratory, sponsored by the Air Force Office of Scientific Research under IPA-905-79-01016C, throughout most of the experiments. We are indebted to the entire staff of the particle beam group at the Air Force Weapons Laboratory, in particular, Dr. M. C. Clark and Dr. D. Straw, for their cooperation and assistance in this research. We are indebted also to the following members of the Dynamics Testing Division at Los Alamos National Laboratory for the time-resolved framing and streak camera photography of the FX-100 propagation experiments: Dr. R. Benjamin, L. Builta, Dr. D. Moir, Dr. S. Schmidt, and Dr. T. Starke.

APPENDIX A

Interim Report - Beam Propagation Experimental Study

INTRODUCTION

During February, 1981 the FX-25 accelerator was made available for development of diagnostics and exploratory propagation experiments. The diagnostic effort focused on the development of an array of subminiature Faraday cups for the determination of the beam spatial distribution. Experiments were also performed with a new technique for the measurement of the divergence of high energy density beams. In the propagation experiments the previously established range of pressures for stable propagation was confirmed for the particular geometry used; the beam spatial distribution was measured; and data was obtained on beam emittance. These measurements were made over a range of pressures that extended above and below the window for stable propagation. Finally, the beam was extracted into full density air after having propagated through the low pressure drift tube in order to investigate the effect on the hose instability of pulse sharpening, profile broadening, and phase mixing.

I. DIAGNOSTIC DEVELOPMENT

A. Subminiature Faraday-Cup Array

An array of fast-response Faraday-cup charge collectors was developed to measure the time-resolved current density spatial distribution. The use of this array allows the determination of the evolution of the radial beam profile on a single shot. The array used for the measurements reported here consisted of several coaxial Faraday collectors embedded in a carbon beam stop and shielded from the plasma electrons with a thin carbon sheet. The use of subminiature charge collectors eliminates the noise and response time problems associated with the detection of high currents. Furthermore, using a coaxial collector driving a matched and terminated signal cable provides the fastest possible response time. The response time of the signals observed in this experiment was limited by the bandwidth of the oscilloscopes to ~ 1 ns. The high signal level and unbroken coaxially-shielded construction gave essentially noise-free oscillograms.

Graphite was used throughout the design because of its superior resistance to damage by the high energy density beam. In a further development of this design, which had equivalent performance, the insulating gap, t_g , was replaced with a thin sheet (25 μm) of Kapton, which also had a high resistance to damage in this intense beam. A large version of this array has been constructed for use in the FX-100 experiments.

Electron scattering in the probe materials make it difficult to accurately predict the effective area of the coaxial charge collector. Existing Monte Carlo electron-transport codes are being investigated as a means for establishing the sensitivity of the probes. This calibration was established experimentally for the FX-25 array by normalizing current density distributions measured close to the diode (Fig. 2) to the total diode current (measured with a resistive shunt). The same procedure will be used to experimentally calibrate the FX-100 array.

B. Faraday Cup Beam-Emittance Measurements

A new technique for making a time resolved measurement of the beam emittance was experimented with on the FX-25. Consider the geometry of Figure 1 with the thin carbon sheet (t_c) removed and the UT-47 solid coax retracted into the hole in the carbon block to a depth, δ , from the front surface. If the carbon were a perfect absorber then the only electrons that would be collected would be those with angles of incidence less than $\tan^{-1} D/2\delta$. A set of such probes retracted to different depths would thus provide a quantitative time-resolved measurement of the angular distribution of the incident beam. In fact, scattering in the carbon complicates the interpretation of the data obtained with this geometry and without elaborate Monte Carlo calculations, the results of the measurements made on the FX-25 can be only considered crude estimates, at best. Even using the scattering by known foil thicknesses as a means of establishing an empirical calibration does little to reduce the difficulty in interpreting data collected with this geometry. These preliminary experiments did, however, result in an improved design that should give easily interpreted data, and has been constructed for the FX-100

experiments. In this apparatus the coax charge collectors are set at the bottom of conical (rather than cylindrical) holes with varying cone angles. The depth of each hole is the same and is greater than one practical range in carbon for the FX-100 electron energy. This should sharpen the angular discrimination lacking in the previous design. Multiply-scattered electrons, secondaries, and plasma electrons will be discriminated against by use of a Kapton insulated tantalum sheet over the end of the coax detector. An experimental calibration will be effected by exposing the array to the FX-100 beam scattered in anode foils of known thickness. This will be backed up with Monte Carlo scattering calculations.

11. PROPAGATION EXPERIMENTS

The propagation experiments reported here were performed in reduced pressure air in a 5-cm inner diameter, 307-cm long conducting drift tube. A graphite Rogowski surface cathode was used with a 25- μ m Ti foil anode to produce a ~ 20 μ s, 20 - 25 kA, 1.5 - 2.0 MeV beam from the FX-25 accelerator (Fig. 2). It has been previously established that the pressure window for stable propagation for this accelerator is 1 - 2 Torr. This was confirmed for this particular geometry by measurements of the beam energy deposited in a graphite calorimeter especially constructed for these experiments. The maximum energy was deposited in the calorimeter when the drift tube pressure was 1.6 Torr. This was only about 15 - 20% of the initial beam energy. The reason for this inefficient transport became clear when time-resolved measurements of the current density at 3 m were made. As seen in the data for the on-axis probe (Fig. 2) there was no pressure for which the full ~ 20 ns diode-current pulse width was propagated to the end of this drift tube. At the lower pressures, erosion of the beam head shortened the pulse from the maximum width of ~ 12 - 15 ns observed at ~ 1.6 Torr, while at higher pressure the hose instability eroded the tail of the beam as well. This overlap of the pressure regimes for severe nose erosion and hose instability was not observed on earlier FX-25 experiments with larger-diameter drift tubes, and is probably a result of the small-diameter tube used for these experiments.

The beam distribution at peak current evolved into a Bennett-like profile at the end of the drift tube as shown in Figure 4. The Bennett radius for the beam propagated in 1.6 Torr air inferred from these data is ~ 0.5 cm, and corresponds closely to the radius inferred from damage to dielectric foils (Fig. 4). However, the radius inferred from open shutter photographs of N_2^+ fluorescence at 3914 \AA is about a factor of two greater, probably as a result of excitation by lower energy secondaries and plasma electrons.

As the pressure was reduced below 1.6 Torr into the regime of severe erosion of the beam, the profile broadened (Fig. 5), and an increase of current transported in the wings was observed. The inferred Bennett radius increased with reduced pressure until it was approximately equal to the tube radius at a pressure of ~ 0.8 Torr.

The total beam current inferred from the distribution profiles and maximum current rate of change are shown in Figure 6. It is seen here that although the current may be sharpened by erosion at lower pressures, the reduction in current results in an overall reduction in the rate of change.

III. BEAM EXTRACTION EXPERIMENTS

To date, all high intensity beams extracted directly from the diode into full density air have been observed to become hose unstable within a few (1 - 4) betatron wavelengths. The betatron wavelength is $\lambda_B \sim 2\pi a (I_A/I_{net})^{1/2}$, where I_{net} is the net (beam plus plasma) current, "a" is the Bennett equilibrium radius, and $I_A = \gamma \beta mc^3/e$ is the Alfven current. Therefore, effects that increase the equilibrium radius (such as increased beam emittance from foil scattering) have been observed to increase the hose-free propagation distance in previous experiments. Thick foil scattering also appears to have increased the number of betatron wavelengths before hose disruption, perhaps because of a reduction in growth rate resulting from more rapid phase mixing of the betatron motions. Finally, it is noted that a reduction of I_{net} will also increase λ_B and thus the hose-free propagation distance.

Extraction of the FX-25 beam into full-density air after it propagates through the 3-m low-pressure drift cell could be expected to produce a more stable beam by some combination of the aforementioned effects. The beam was observed to have a higher emittance at the end of the drift tube than at the diode. Furthermore, at the lower pressures the observed larger Bennett equilibrium radius would favor a larger hose-free propagation path. Finally, erosion-sharpened beam fronts could produce higher conductivity (as a result of avalanching in the high induction field) that in turn would result in reduced net currents and the associated increased λ_B .

To test the possibility of stabilizing the hose by pre-equilibration in a low-pressure propagation cell, the FX-25 beam was extracted through a 25- μ m Kapton foil at the end of the 3-m drift tube. As the propagation-cell air pressure was reduced from slightly above the propagation window to slightly below, a marked stabilization of the hose was observed (Fig. 7 - 10) at pressures ≤ 1 Torr. Hose-free propagation was observed below this threshold until the beam struck the shield-block wall ~ 1 m from the exit point. (Presumably, if the available space for propagation were greater, then the extracted beam would eventually destabilize.) Hose stabilization in these experiments apparently resulted from increased emittance and Bennett-equilibrium radius at the reduced pressures. Enhanced conductivity was probably not contributory, because, as shown in Figure 6, the rate-of-change of beam current did not increase significantly as the cell pressure was dropped.

In conclusion, the availability of time on the FX-25 made it possible to develop two of the more important diagnostics required for the forthcoming FX-100 propagation experiments. A limited set of propagation experiments in a 3-m drift tube was performed that indicated an increased Bennett equilibrium radius at pressures below the pressure for maximum beam energy transport. This effect was used to stabilize the beam extracted into full-density air.

The author wishes to acknowledge the assistance of Winston Bostick in performing these experiments, especially in the development stages of the subminiature Faraday collectors.

This research was sponsored by the Air Force Office of Scientific Research (AFSC) under contract F49620-81-C-0016. Professor Bostick is a senior research physicist in the University Residency Research Program sponsored by the Air Force Office of Scientific Research under IPA-905-79-01016C.

Figure 1. Subminiature Faraday collector for beam current density measurements. The graphite shield thickness ($t_c = 1.8$ mm) is sufficient to stop electrons with energies less than 700 keV. An insulating gap ($t_g = 1.7$ mm) is provided between the shield and the graphite beam stop, which houses the array of rigid coaxial cable (UT-47) detectors. These have solid copper outer ($D = 1.2$ mm) and inner ($d = 0.29$ mm) conductors, and Teflon insulation.

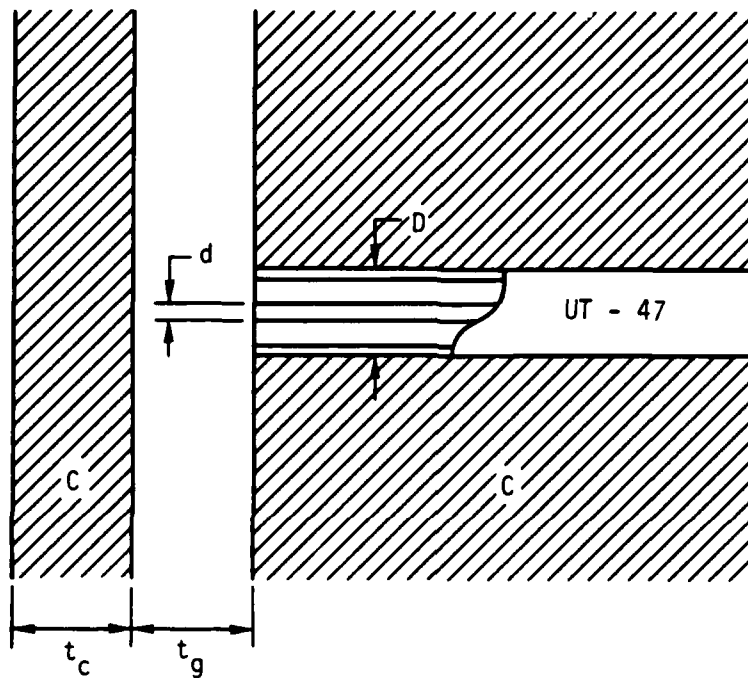
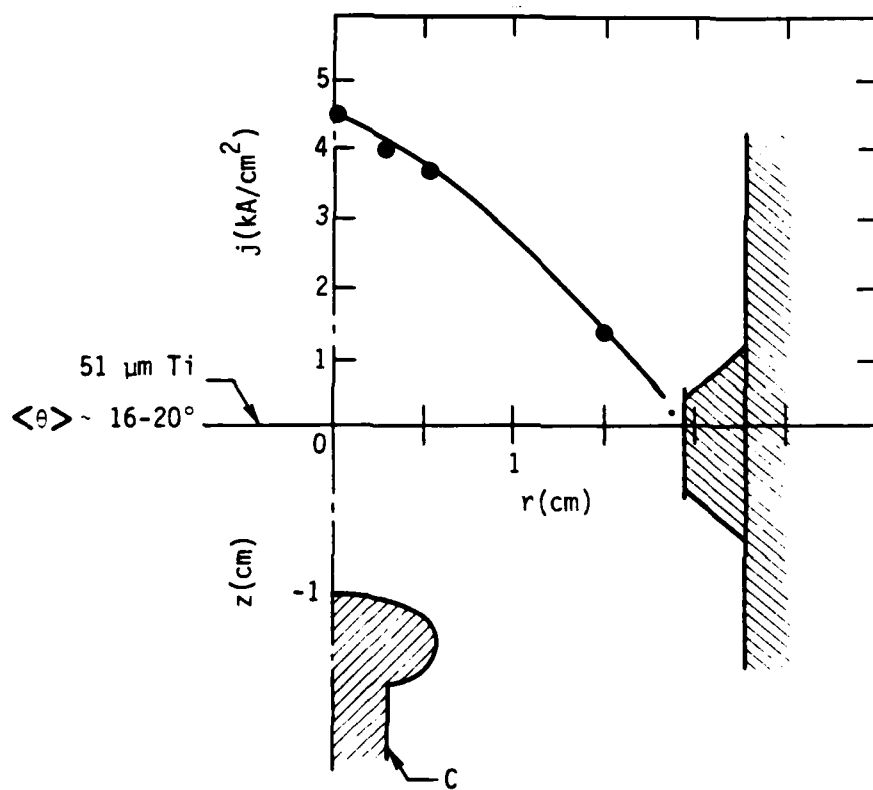


Figure 2. FX-25 diode geometry and beam current density profile measured in vacuum 0.5 cm from the titanium anode foil. The 51- μm anode foil induces a mean scattering angle of 16-20°. The current density profile shown was obtained at the time of peak current ($I_{\text{max}} = 22 \text{ kA}$). The FX-25 produced beams having nominal values for parameters shown.



FX-25

1.5-2.0 MeV

20-25 kA

$\Delta t \sim 20 \text{ ns}$

$t_r \sim 5 \text{ ns}$

Figure 3. Beam current density on axis for different pressures near the propagation window. The current density near the diode had a waveform that approximated the envelope of these signals. The erosion of the beam nose is clearly evident at pressures below 1.6 Torr (upper). At higher pressures both nose erosion and tail loss resulting from hosing are evident (lower).

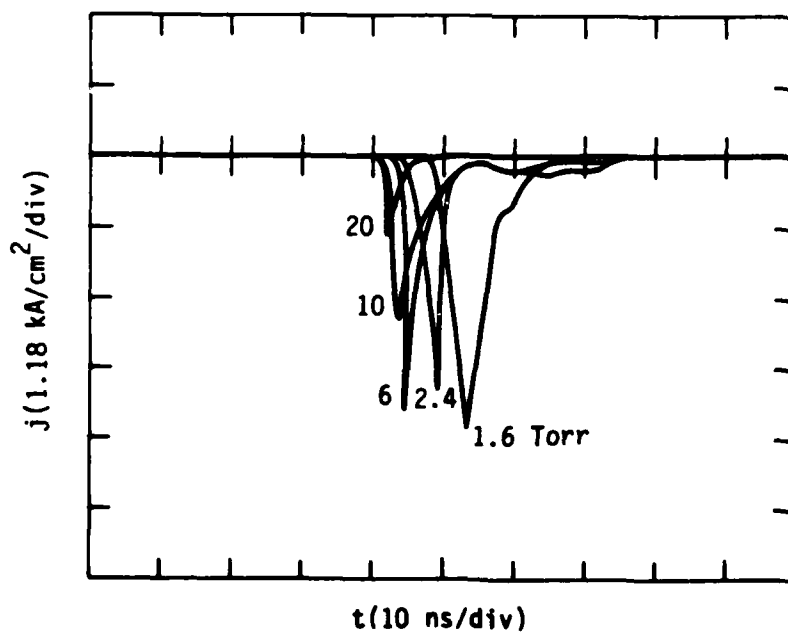
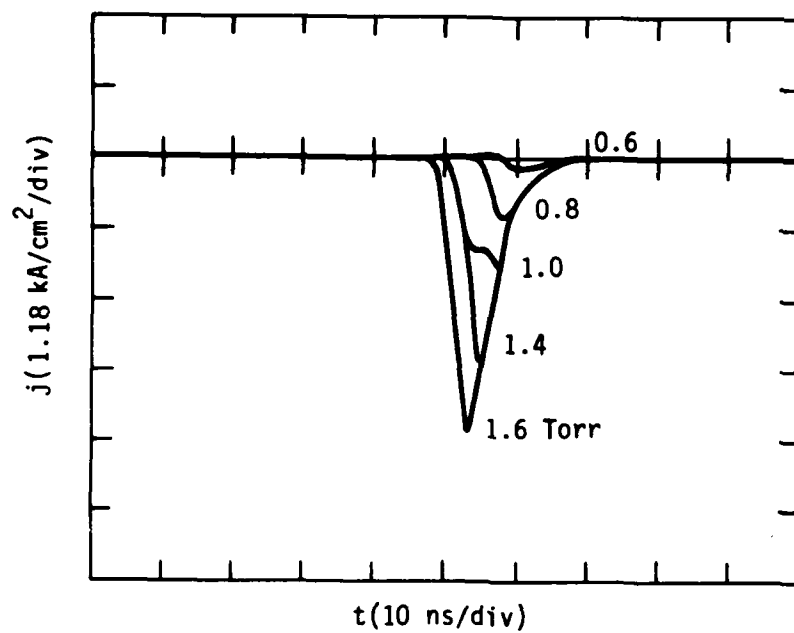


Figure 4. Evolution of the beam current distribution near the diode (upper figure) into a Bennett-like profile (lower figure) after propagating 3-m in 1.6-Torr air (the pressure for maximum energy transport). Also shown are the range of radii determined from damage to dielectric foils (centered at $r \sim 0.5$ cm), and determined from extent of 3914 \AA (N_2^+) emission (centered at $r \sim 1$ cm).

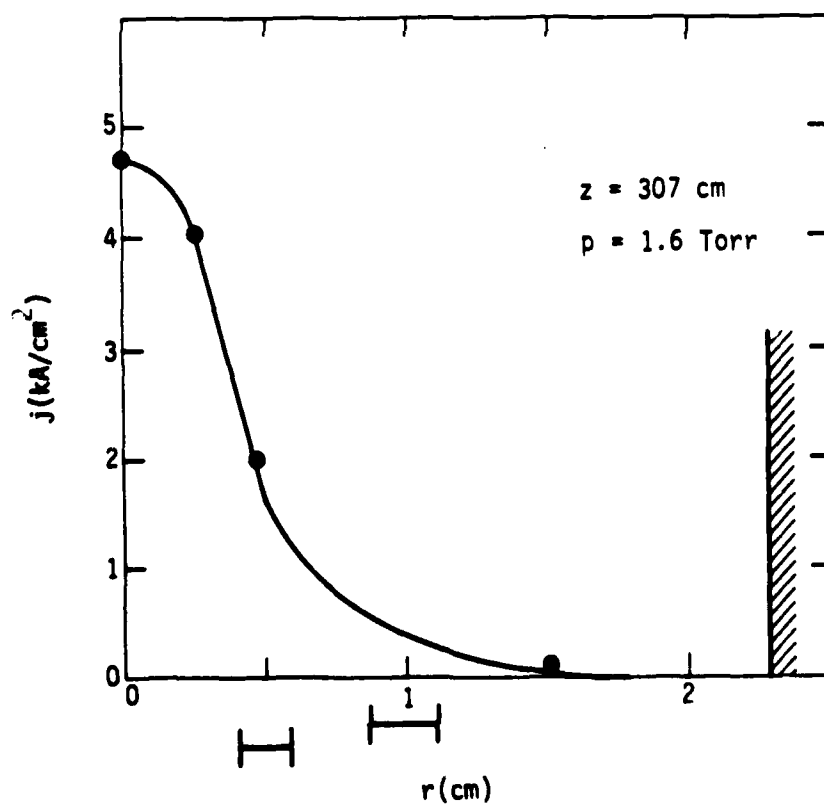
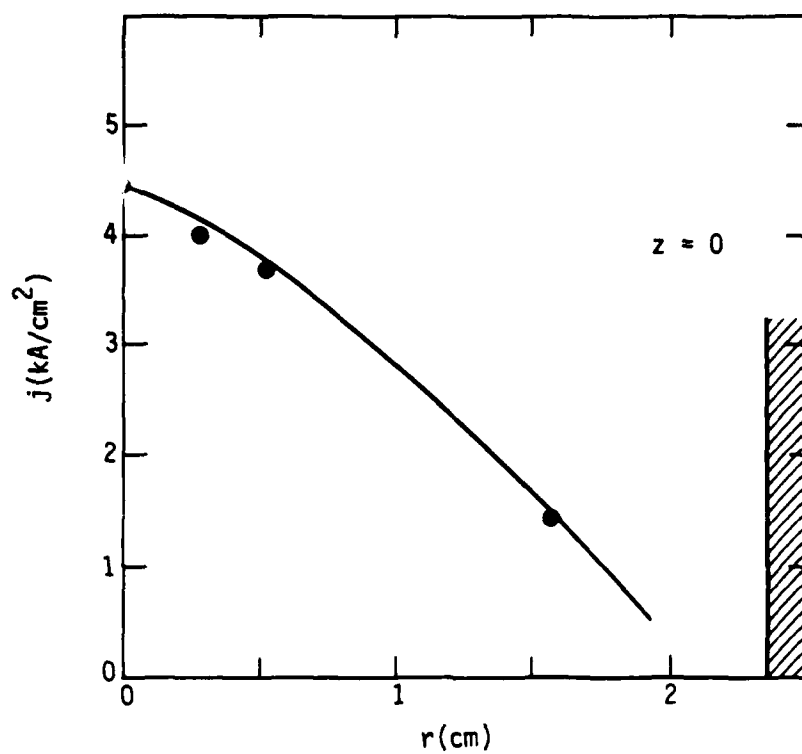


Figure 5. Beam current distributions at 3 m for several air pressures. Maximum energy transport was observed at 1.6 Torr. The increased current density in the wings of the profiles at lower pressures was an effect noted on all of the shots at these pressures.

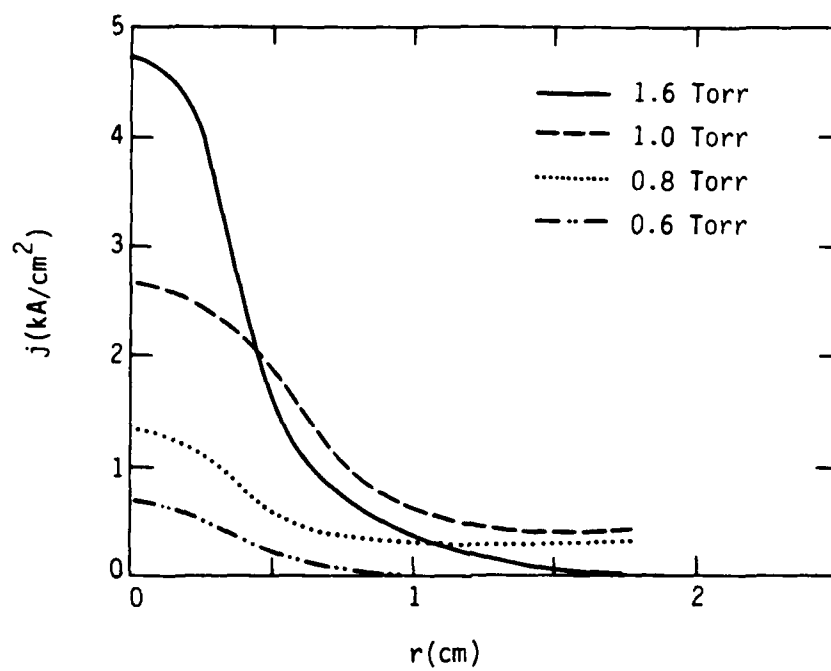


Figure 6. (Upper figure) Total beam current at the end of 3 m. These data were obtained by integrating the current distributions measured with the array of miniature Faraday cups. (Lower figure) Maximum time rate-of-change of the beam current at the end of the three meter drift tube.

AD-A118 755

MISSION RESEARCH CORP ALBUQUERQUE NM
FX-25 AND FX-100 PROPAGATION EXPERIMENTS.(U)
JUL 82 C A EKDAHL, L A WRIGHT, T P HUGHES
AMRC-R-391

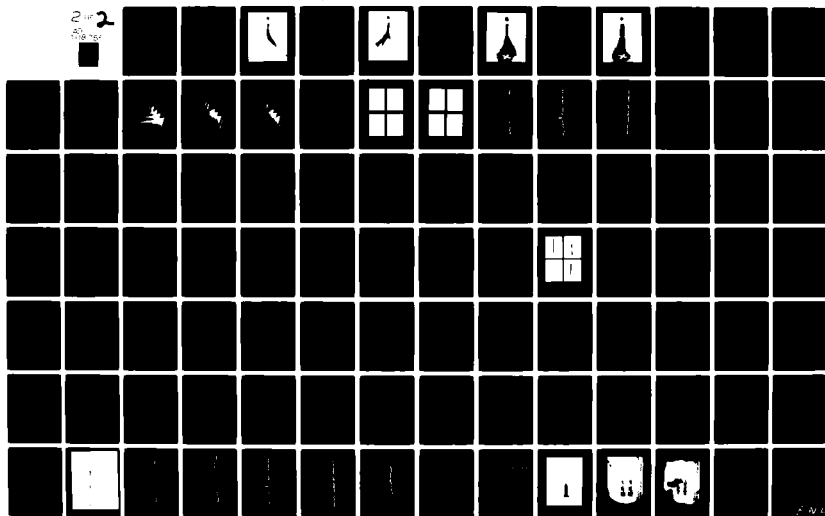
F/G 20/7

F49620-81-C-0016

NL

UNCLASSIFIED

2 of 2
Microfilm
[Symbol]



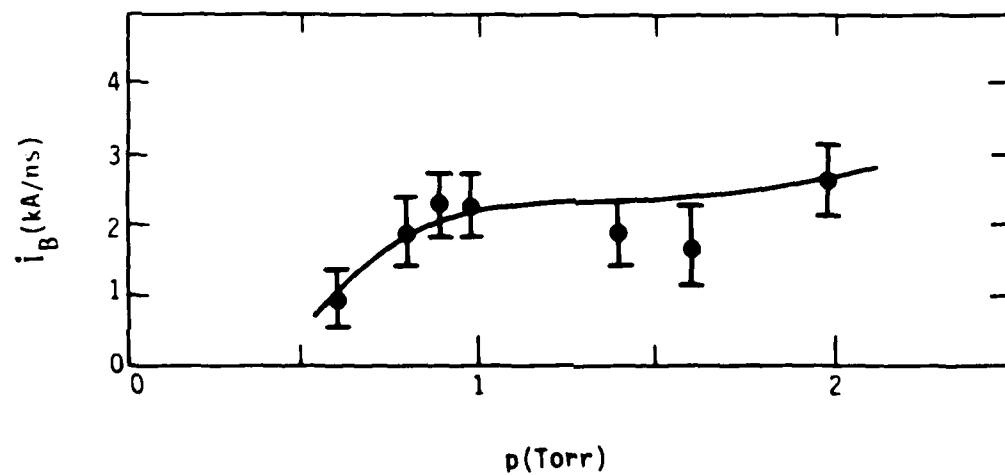
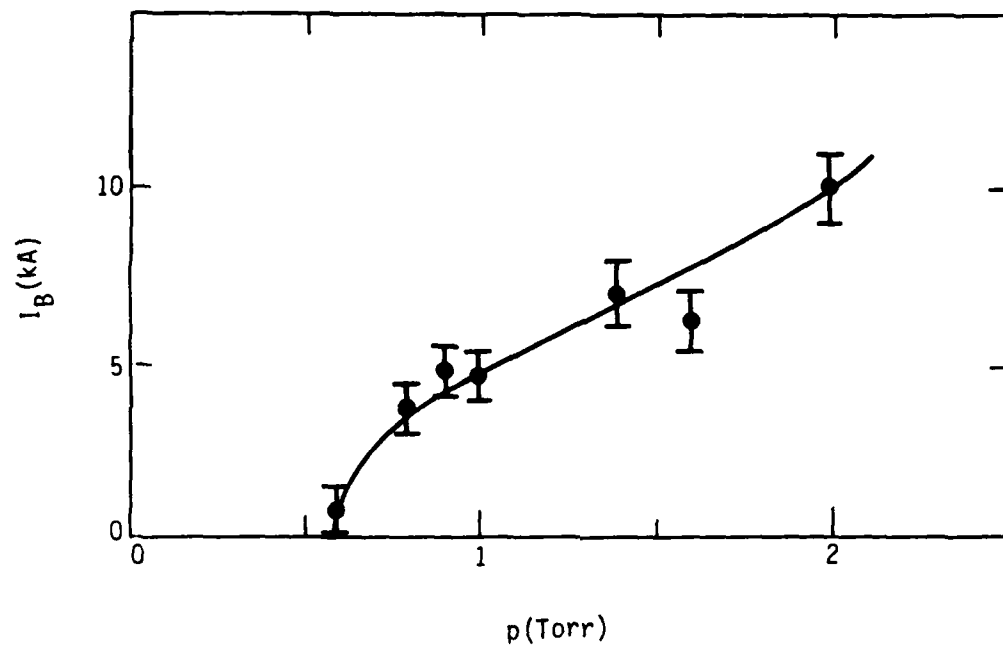
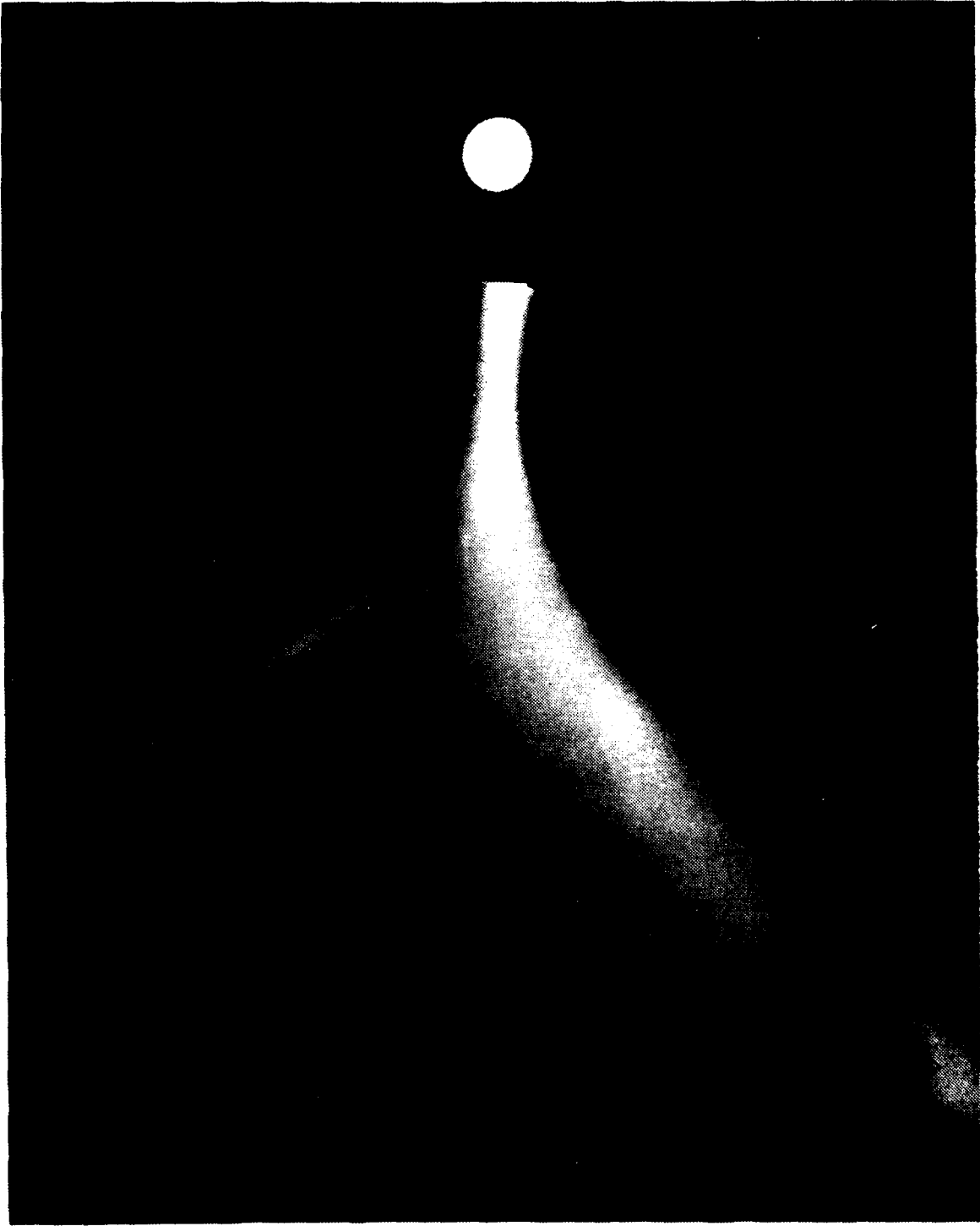
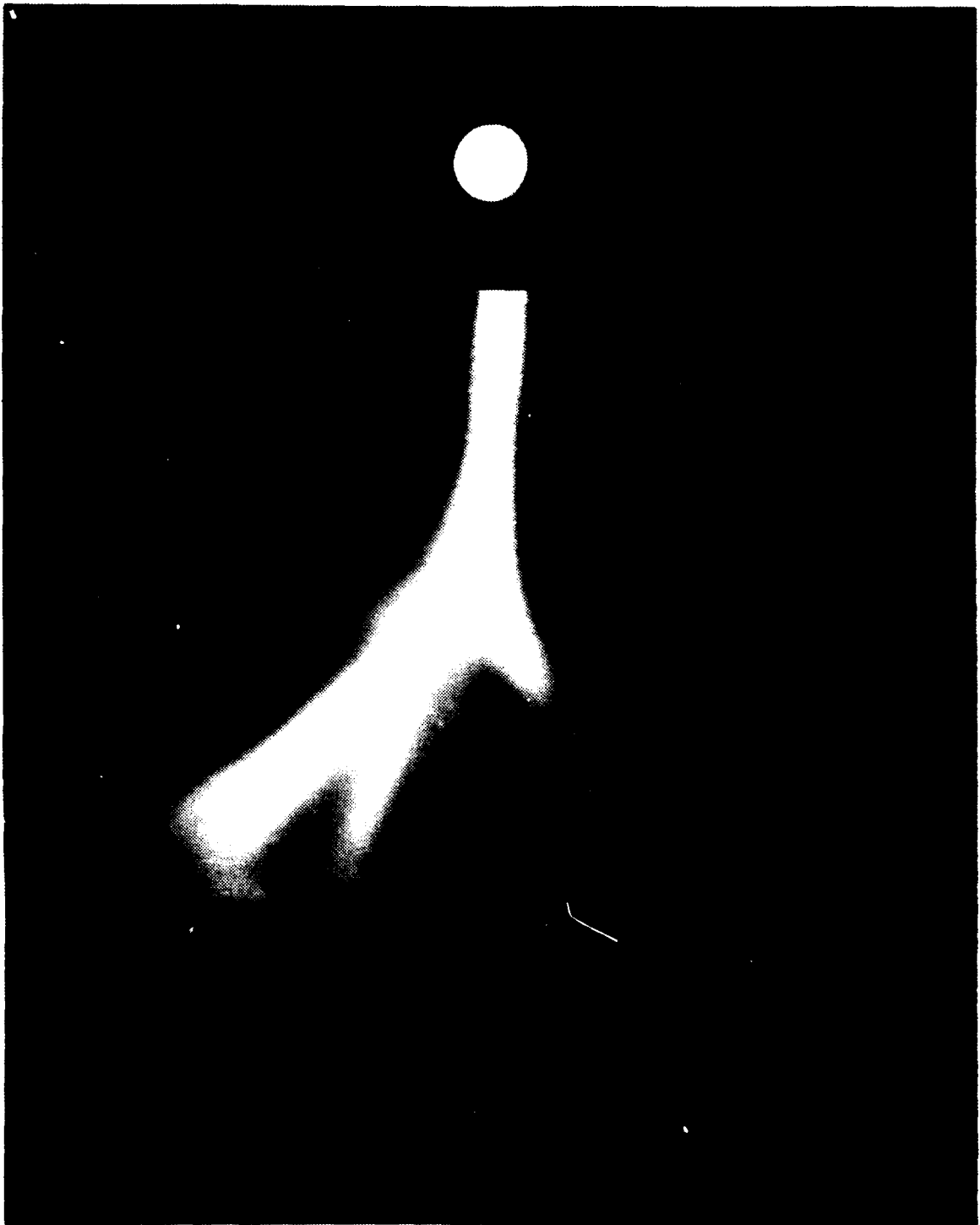


Figure 7. Open shutter photograph of the FX-25 beam extracted into full-density air after drifting thorough 3-m of 3-Torr air.



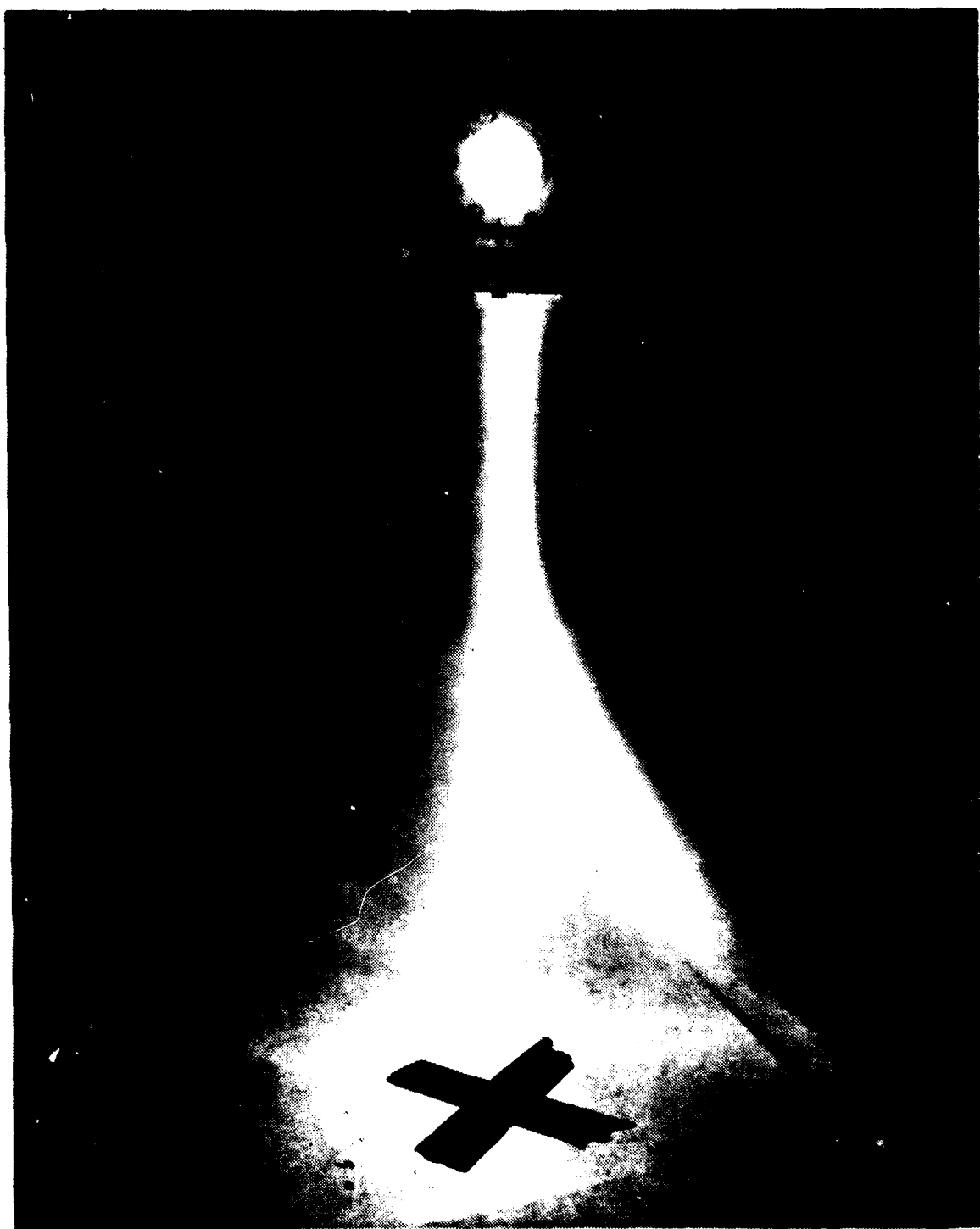
Open shutter photograph of the FX-25 beam extracted into full density air after drifting through 3-m of 0.6-Torr air.

Figure 8. Open shutter (time integrated) photograph of FX-25 beam extracted into full-density air (630 Torr) through a 25- μ m Kapton foil after propagating 3-m in a 5-cm diameter conducting drift tube. The air pressure in the drift tube was 1.6 Torr, the pressure for maximum beam energy transport. The beam in the drift tube is visible through the round port on the drift tube.



1.6 Torr air pressure in 3-m drift tube

Figure 9. Open shutter photograph of the FX-25 beam extracted into full-density air after drifting through 3-m of 0.8 Torr air.



0.8 Torr air pressure in 3-m drift tube

Figure 10. Open shutter photograph of the FX-25 beam extracted into full density air after drifting through 3-m of 0.6-Torr air.



Open shutter photograph of the FX-25 beam extracted into full-density air after drifting through 3-m of 3-Torr air.

APPENDIX B

**FX-100 Propagation Experiments - DARPA/Services Experimental
Coordination Meeting**

MRC

**BEAM PROPAGATION EXPERIMENTS
USING AFWL FX-25 AND FX-100**

**CARL EKDAHL (MRC)
WINSTON BOSTICK (UNIVERSITY RESIDENT AT AFWL)**

**SPONSORED BY THE AIR FORCE OFFICE OF SCIENTIFIC
RESEARCH UNDER CONTRACT F49620-81-C-0016 AND
IPA-905-79-01016C.**

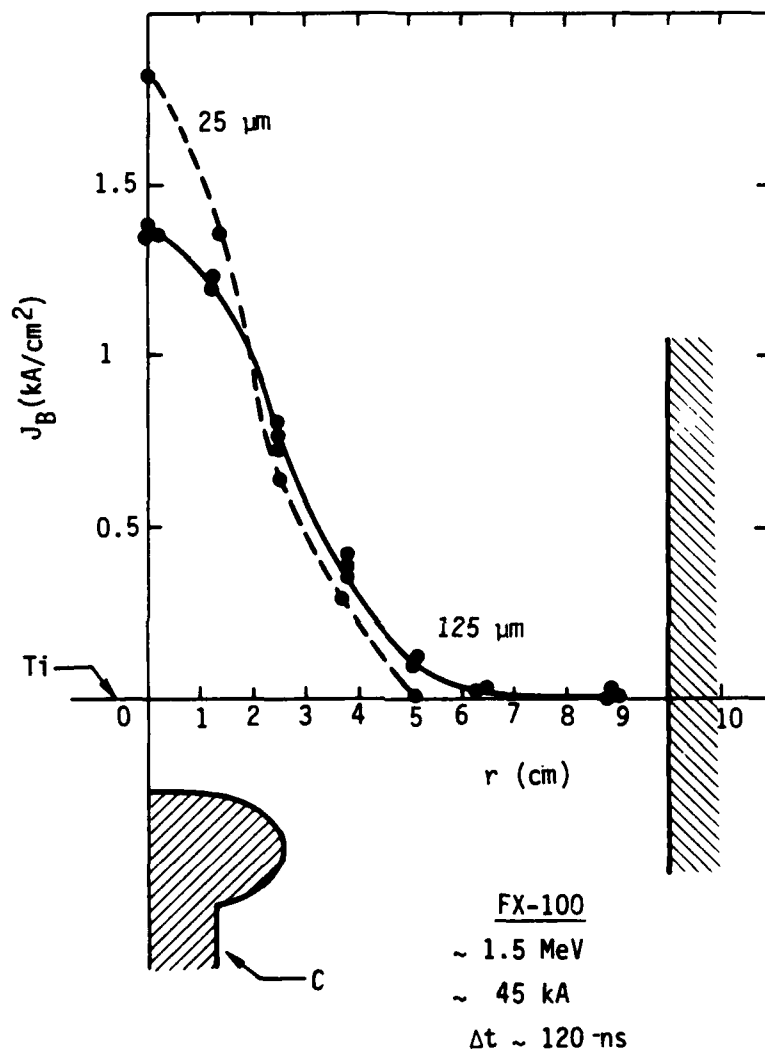


Figure 1. Beam profile at peak current at injection into drift tube. Also shown is the geometry of the Rogowski surface cathode used to obtain quasi-Bennett beam profiles. Data is shown for two anode-foil thicknesses, however, only 25- μ m foils were used for the propagation experiments.

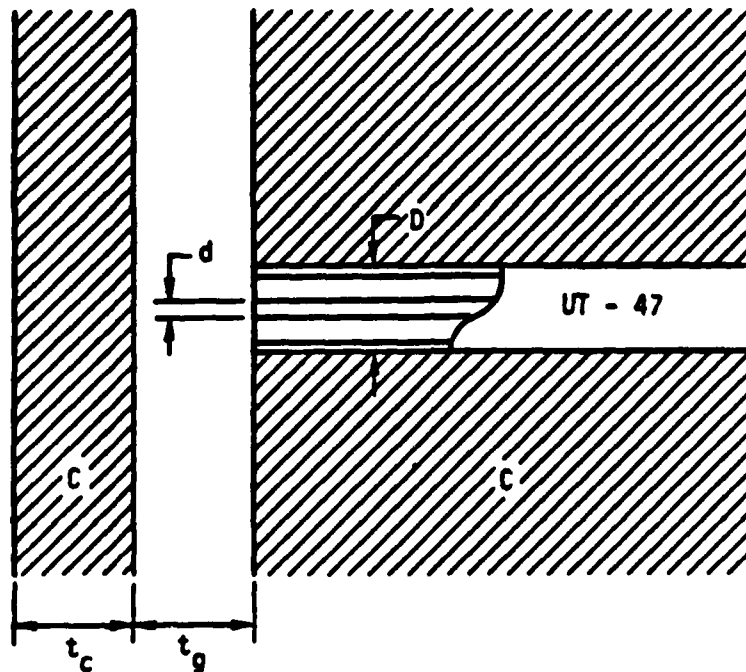


Figure 2. Geometry of subminiature Faraday collector. For FX-25 array the C plasma shield was $t_c = 1.8$ mm thick and was insulated by a $t_g = 1.7$ mm vacuum gap. The FX-100 array used a $t_c = 0.125$ mm thick Ti shield and $t_g = 0.025$ mm Kapton foil insulator. Both arrays used UT-47 rigid-coax collectors with $d = 0.29$ mm diameter inner conductors and $D = 1.2$ mm diameter outer conductors with Teflon insulation.

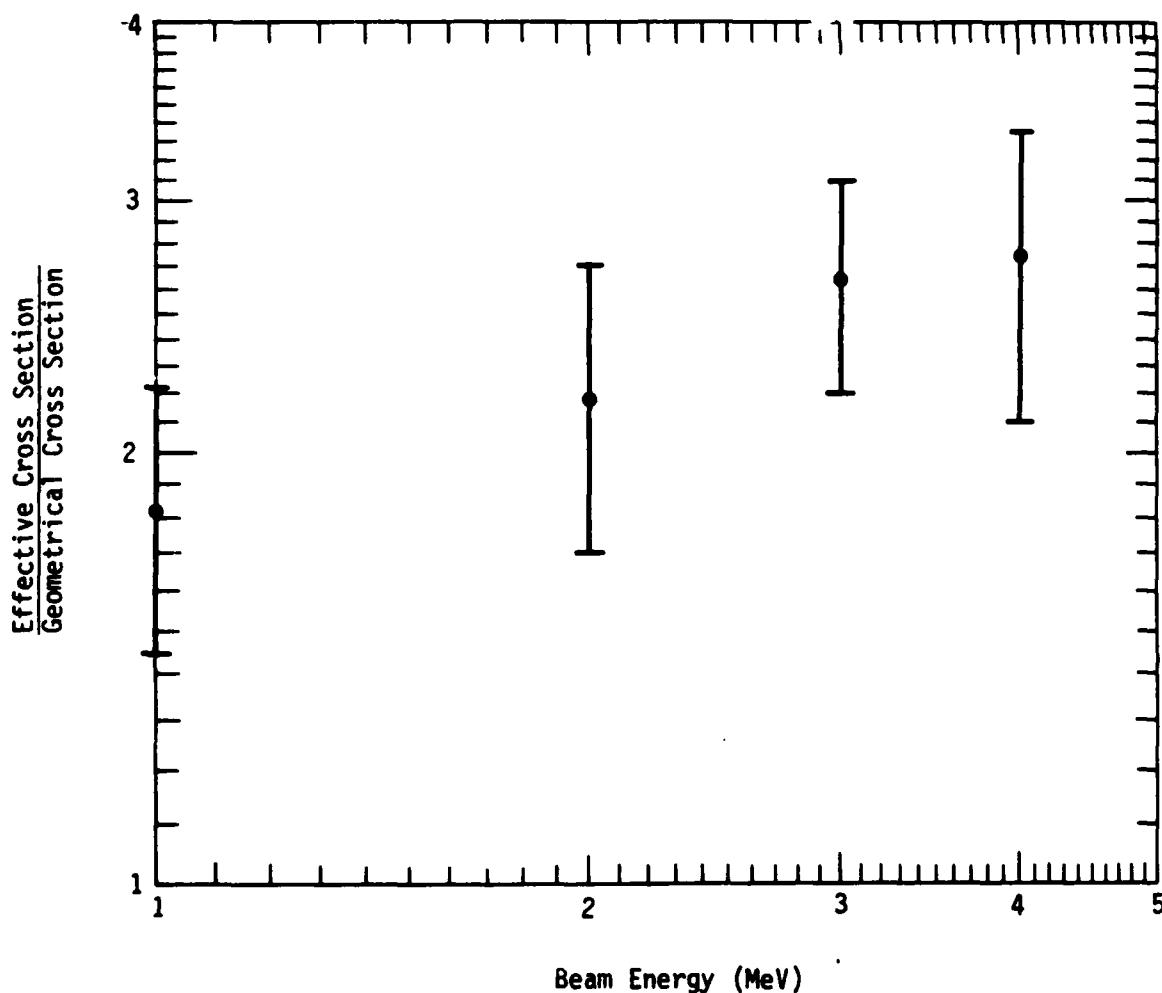


Figure 3. Energy sensitivity of the effective collection area for the sub-miniature Faraday cup array. The Monte Carlo transport code, CYLTRAN, was used to calculate this sensitivity, which results from scattering of electrons into the collector from the surrounding materials.

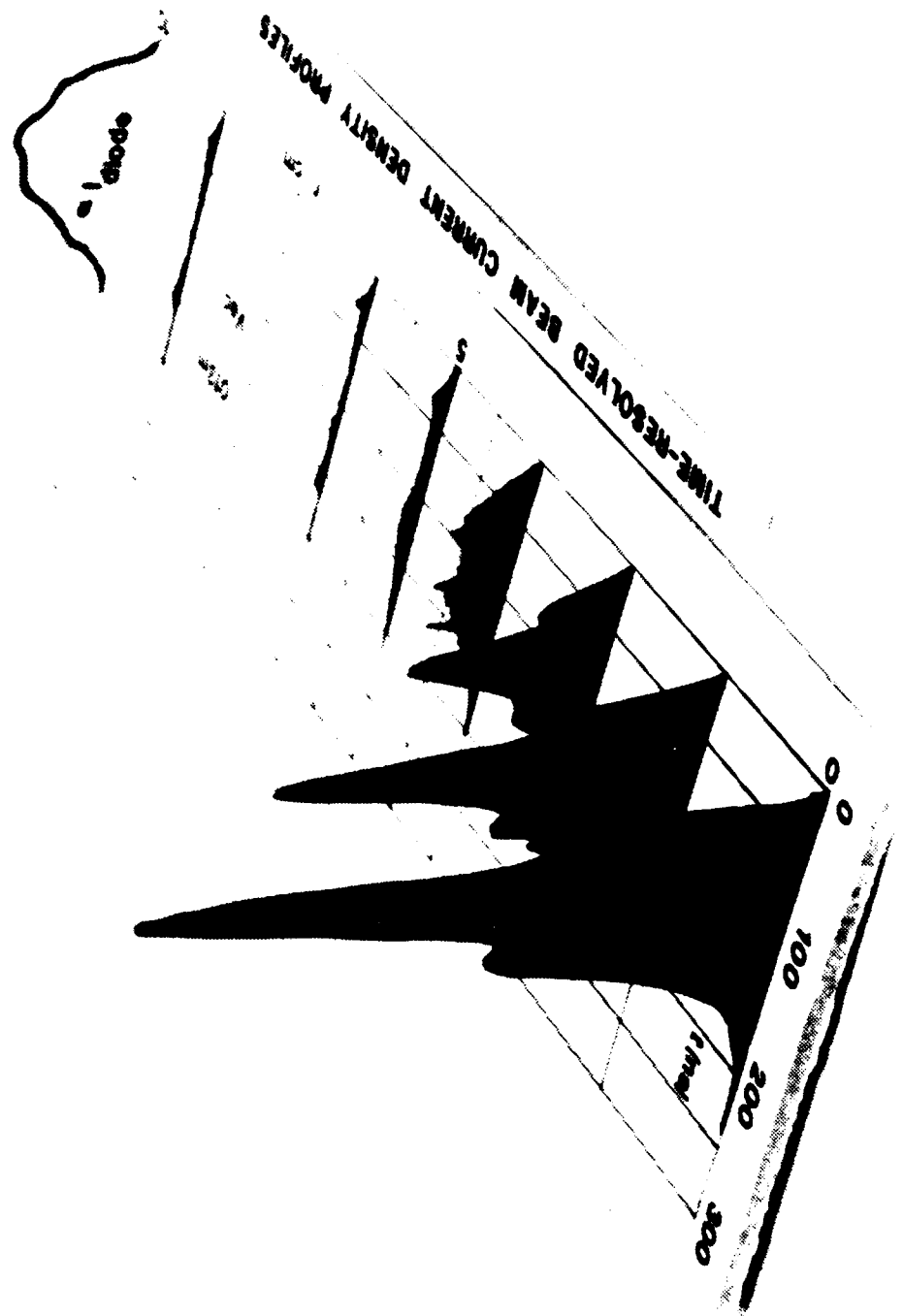


Figure 4. Time-resolved FX-100 beam current density profile at injection obtained with the subminiature Faraday collector array. This shows very little diode shark emission (at large radii).

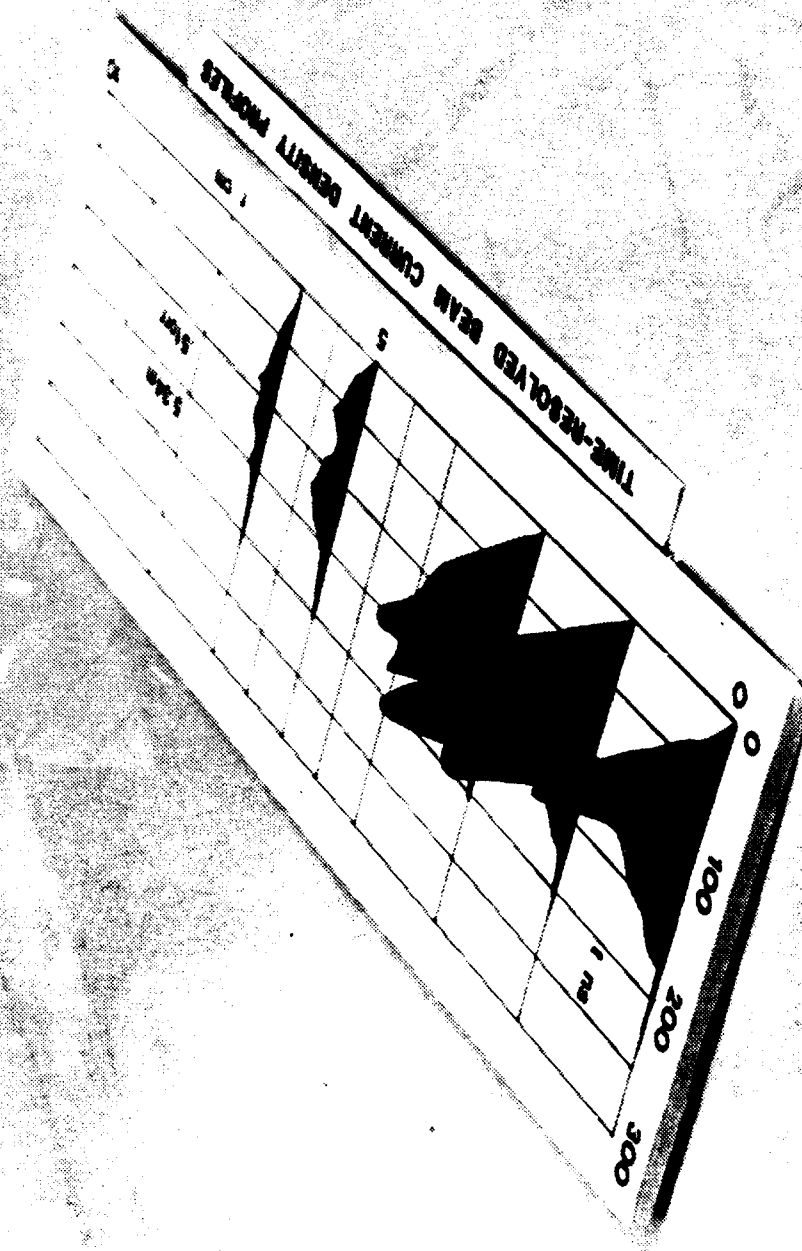


Figure 5. FX-100 beam current density profile after propagating 5.34 m through air at a pressure of 0.5 Torr. In this shot the beam was slightly off axis.

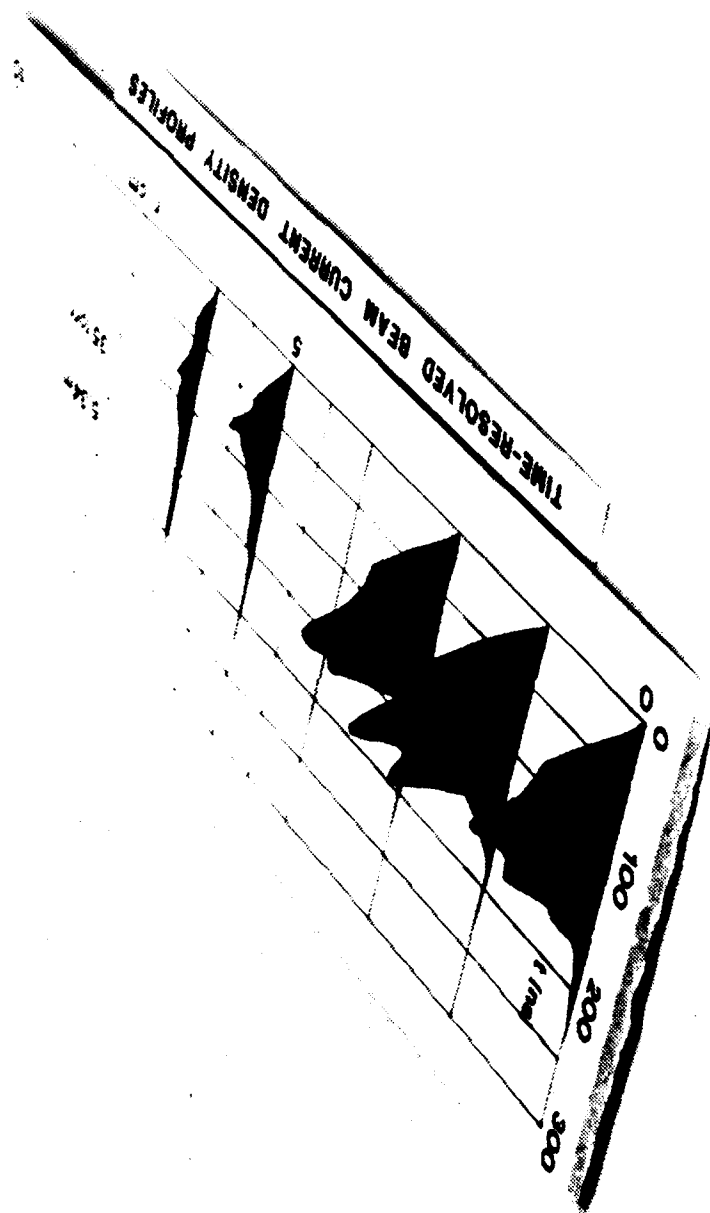


Figure 6. Time-resolved beam current density profile after propagating 5.34 m in 0.35-Torr air. This shot shows the development of an annular region of current transport (at $r=5$ cm).

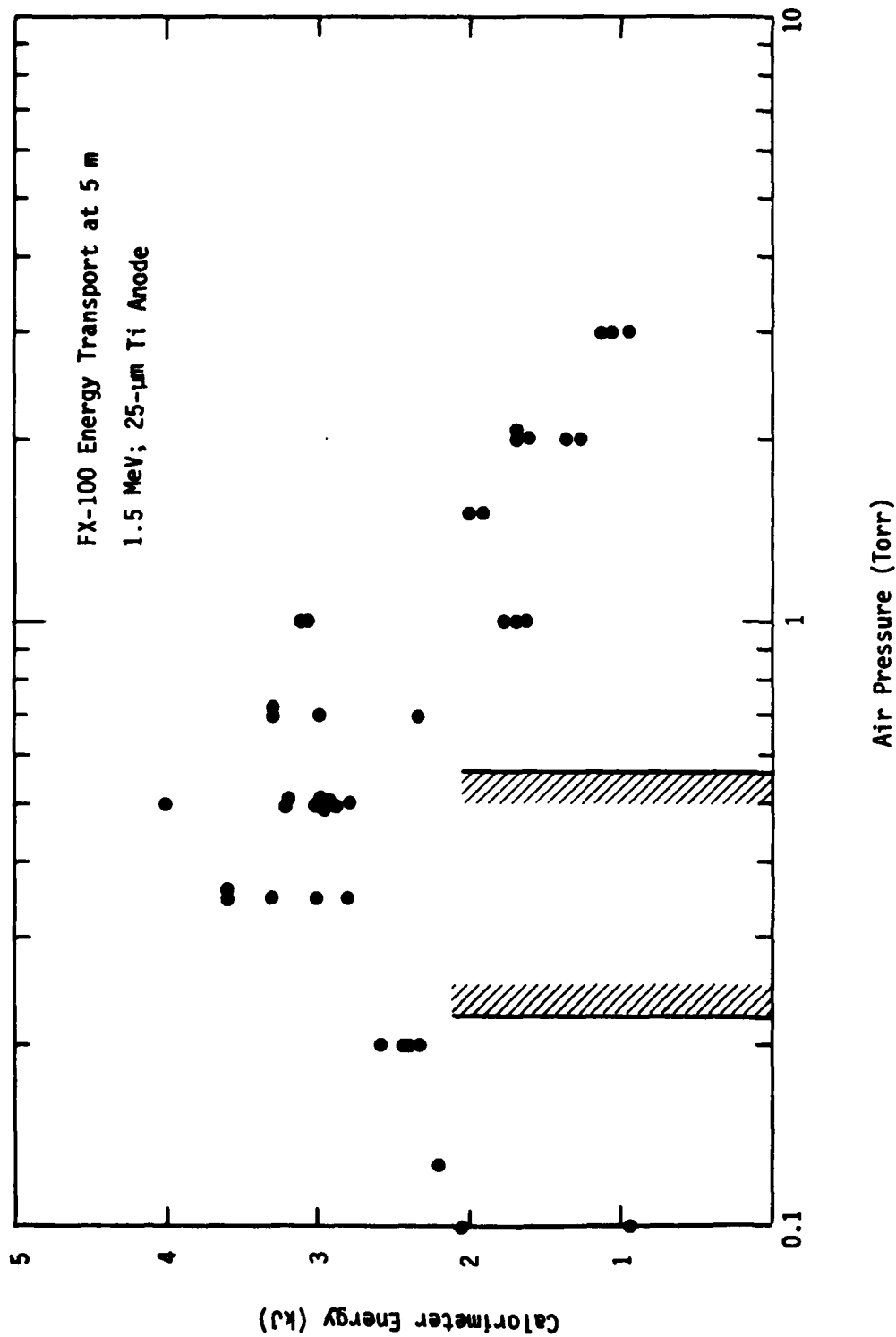
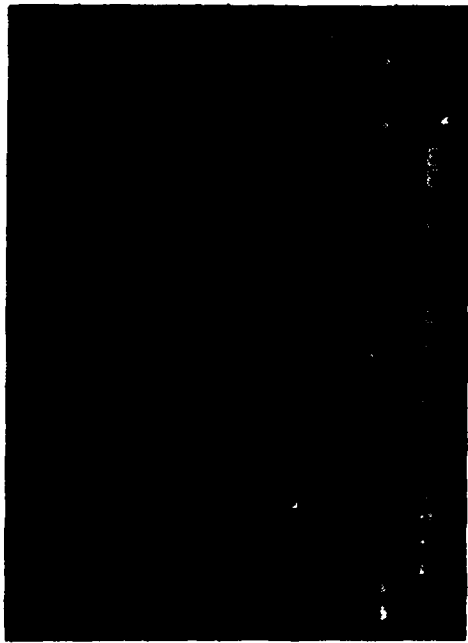
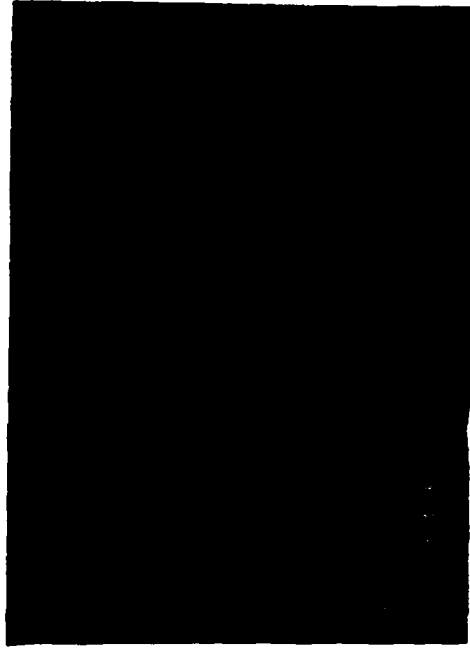


Figure 7. Energy deposition by FX-100 beam in a carbon calorimeter at the end of the 5.3 m drift tube. The shaded region indicates the pressure window in which spectra showed evidence for atomic line emission near the beam axis.



(a)



(b)



(c)

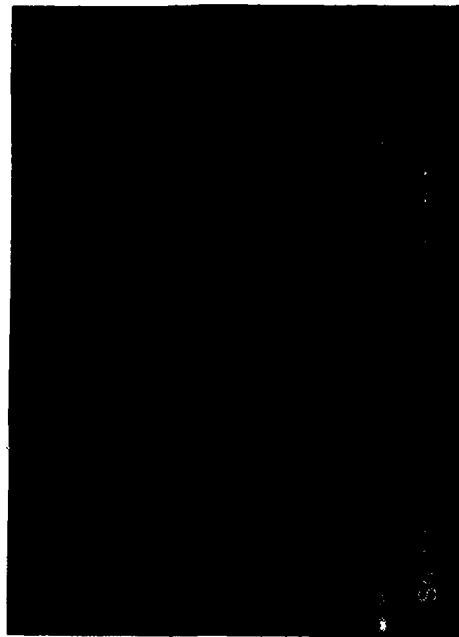


(d)

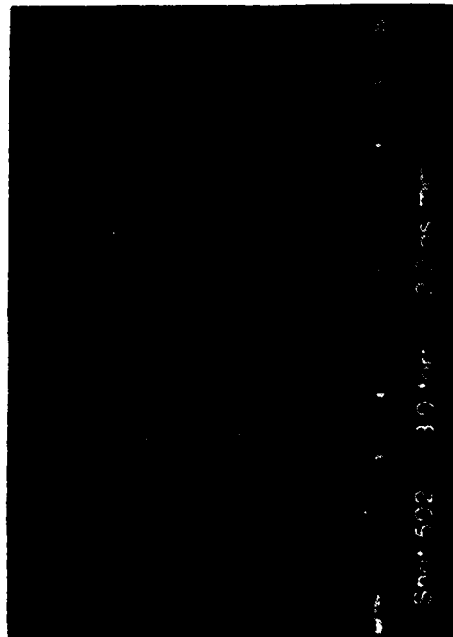
Figure 8. Streak-camera photographs of the beam-excited air emission at $Z = 4.5$ m as pressure is increased from below the propagation pressure window (a) to the center of the window (d). (Ignore the image converter-tube blemish in the far left of each photograph.) The beam head is at the left of each streak (taken through a vertical slit). The delay in start of emission in (a) as compared with (d) is presumably the result of erosion at lower pressures.



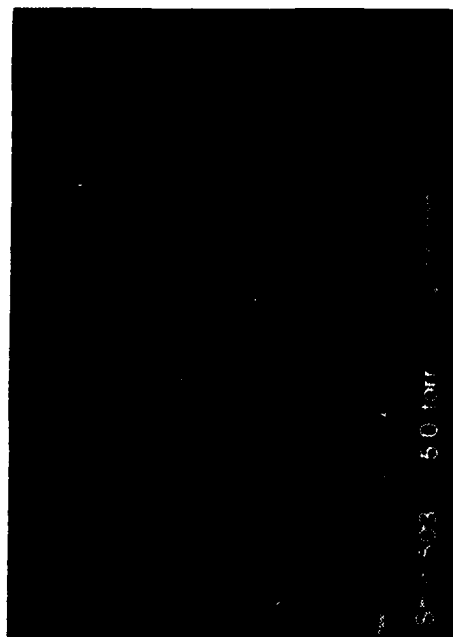
(a)



(b)



(c)



(d)

Figure 9. Streak-camera photographs of the FX-100 beam at 4.5 m as air pressure is increased above the propagation window showing loss the tail of the beam. Figures (b) and (c) show especially clear evidence of hosing in the tail.

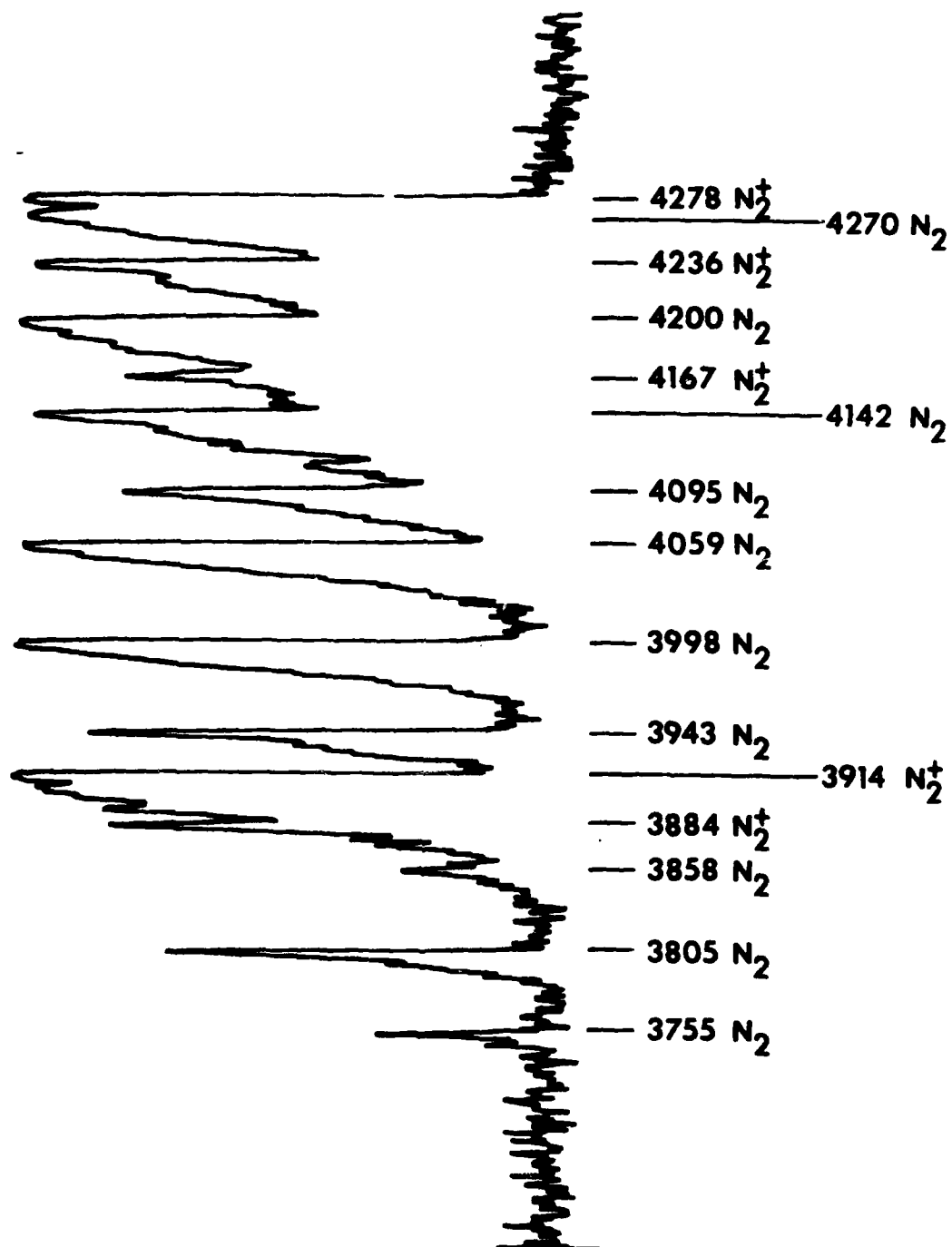


Figure 10. Microdensitometer scan of time-integrated spectrometer photograph of the emission from FX-100 beam-excited air at 0.35-Torr pressure. This scan shows the characteristic molecular nitrogen band emission that gives rise to the blue color in beam excited air.

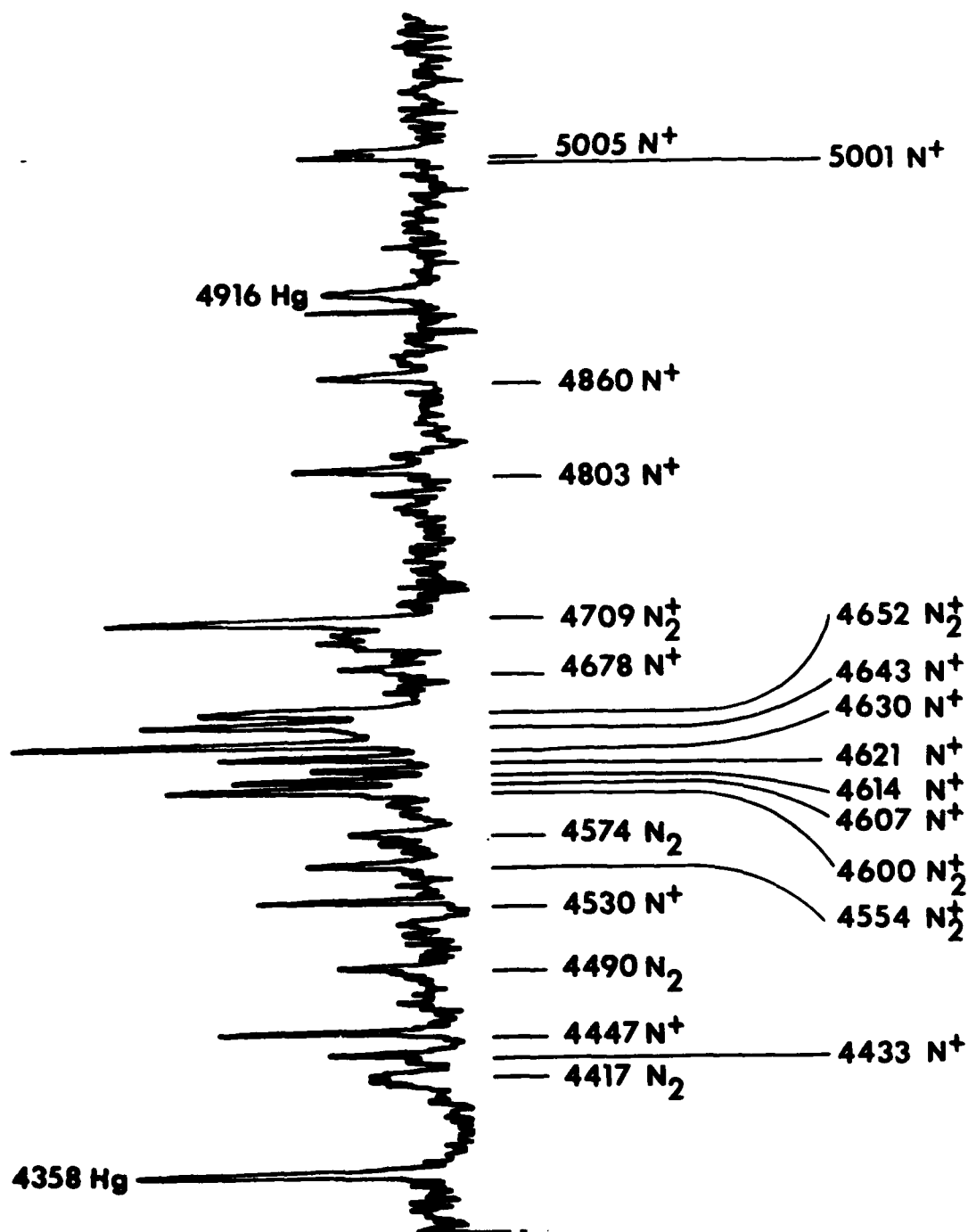


Figure 11. FX-100 beam-excited air spectrum in blue-green region. (Hg lines from calibration source.) This shows the appearance of singly ionized nitrogen lines (N^+) in 0.35-Torr air experiments, which is indicative of high plasma electron temperatures.

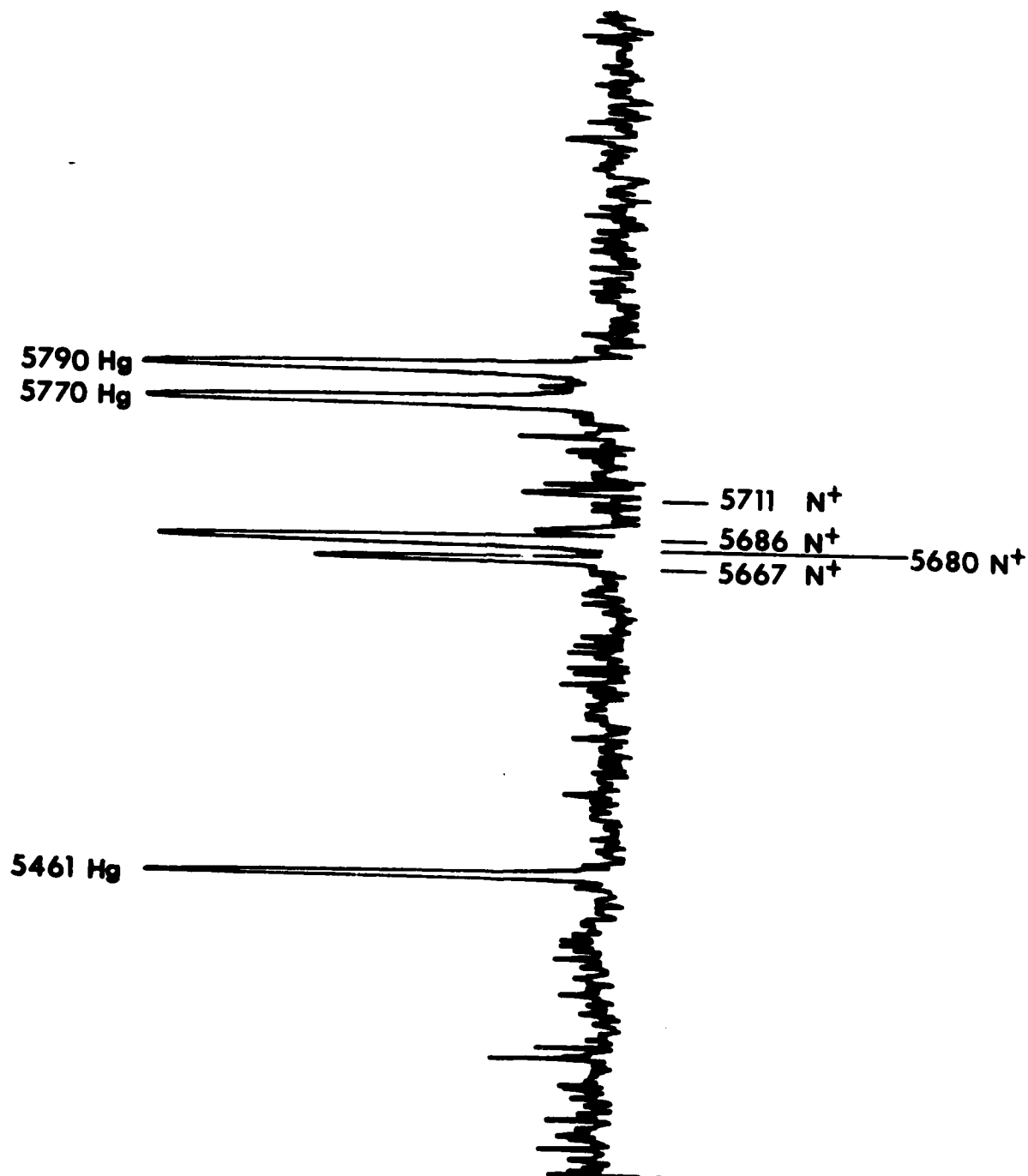


Figure 12. FX-100 beam-excited 0.35-Torr air spectrum in the yellow region showing further N⁺ line emission. Note that -24 eV is required to dissociate and ionize nitrogen.

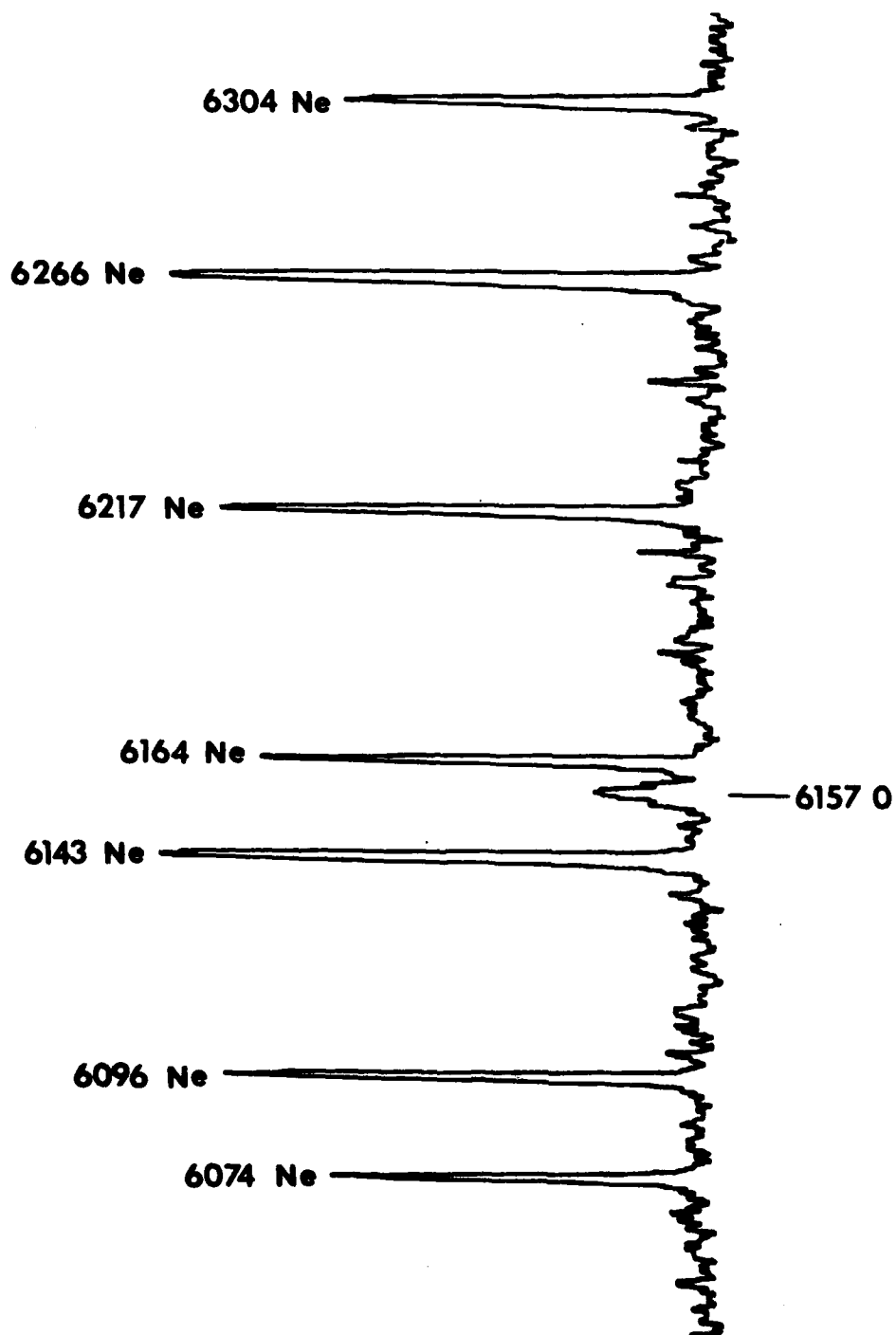


Figure 13. FX-100 beam excited 0.35-Torr air spectrum in the red region showing the atomic oxygen line responsible for the vivid red that appears in open shutter photographs taken in this pressure regime.

WAVELENGTH λ	ATOM/MOLECULE	TRANSITION (band) (v' , v'')
3755	N_2	(2+) (1,3)
3805	N_2	(2+) (0,2)
3858	N_2	(2+) (4,7)
3884	N_2^+	(1-) (1,1)
3914	N_2^+	(1-) (0,0)
3943	N_2	(2+) (2,5)
3998	N_2	(2+) (1,4)
4059	N_2	(2+) (0,3)
4095	N_2	(2+) (4,8)
4142	N_2	(2+) (3,7)
4167	N_2^+	(1-) (3,4)
4200	N_2	(2+) (2,6)
4236	N_2^+	(1-) (1,2)
4270	N_2	(2+) (1,5)
4278	N_2^+	(1-) (0,1)
4344	N_2	(2+) (0,4)
4417	N_2	(2+) (3,8)
4433	N^+	$3d\ 3p_{-4f}\ D(5/2)$
4447	N^+	$3p\ 3D - 3d\ 3D_0$
4490	N_2	(2+) (2,7)
4530	N^+	$3d\ 1F - 4f\ G(9/2)$
4554	N_2^+	(1-) (3,5)
4574	N_2	(2+) (1,6)
4600	N_2^+	(1-) (2,4)
4607	N^+	$3s\ 3p_0 - 3p\ 3p$
4614	N^+	$3s\ 3p_0 - 3p\ 3p$
4621	N^+	$3s\ 3p_0 - 3p\ 3p$
4630	N^+	$3s\ 3p_0 - 3p\ 3p$
4643	N^+	$3s\ 3p_0 - 3p\ 3p$
4652	N_2^+	(1-) (1,3)
4678	N^+	$3d\ 1p_0 - 4f\ D(3/2)$
4709	N_2^+	(1-) (0,2)
4803	N^+	$3p\ 3D - 3d\ 3D_0$
4860	N^+	$3p\ 3D - 3d\ 3D_0$
5001	N^+	$3p\ 3D - 3d\ 3F_0$
5005	N^+	$3s\ 5p - 3p\ 5p_0$
		$3p\ 3D - 3d\ 3F_0$
5667	N^+	$3s\ 3p - 3p\ 3D$
5680	N^+	$3s\ 3p - 3p\ 3D$
5686	N^+	$3s\ 3p - 3p\ 3D$
5711	N^+	$3s\ 3p - 3p\ 3D$
6157	O	$3p\ 5p - 4d\ 5D_0$

Figure 14. Identification of the spectral lines and bands observed from 0.35-Torr air emission.

OBSERVED	AURORAL
WAVELENGTH:	6157 A
DESIGNATION:	4d ⁵ D-3p ⁵ P
ASSOCIATED LINES: NONE WITH SAME INTENSITY	2p ⁴ ¹ D-2p ⁴ ³ P
EXCITATION:	¹ D- ³ P 6364 A ¹ S- ¹ D 5577 A (NOT OBSERVED)
PROBABLY RECOMBINATION	LARGELY PHOTODETACHMENT
OR	$O^+ + e + M \rightarrow O^+ + M$ $O^+ + e + e \rightarrow O^+ + e$
QUENCHING:	HIGHLY QUENCHED BY ELECTRONS
MISCELLANEOUS:	NO FORBIDDEN TRANSITIONS ARE OBSERVED TOO MUCH IS HAPPENING AROUND THE BEAM

Figure 15. The observed red emission, although an atomic oxygen line, was not the 6300 Å auroral line as was initially speculated after first seeing the vivid red in open shutter photographs.

APPENDIX C

Electron Beam Transport in a Small Aperture Faraday Cup

In this appendix, "Appendix A" and "Appendix B" refer to lengthy CYLTRAN outputs in the original report which have been deleted for brevity.

ABSTRACT

The Monte Carlo transport code CYLTRAN is used to study electron transport and scattering in a Faraday cup consisting of a small cross section coaxial cable surrounded concentrically by a massive carbon block. Electrons impinging on the center wire of the coax generate a signal proportional to the electron beam current. As expected, it is found that the effective cross section of the wire is greater than its geometrical cross section due to scattering of primaries into it. The cross section is only slightly modified by production and deposition of secondary electrons in the form of knockons. These effects are dependent on electron beam energy.

PROBLEM CONFIGURATION

The design of a small aperture Faraday cup to measure electron beam current is given in Figure 1. It consists of a UT-47 coaxial cable embedded in a cylindrically shaped massive carbon block. In experiments, the block is sufficiently large in axial and radial extent to stop all primary and secondary electrons. Figure 1 depicts the accurate coaxial cable dimensions. However, the carbon block shown was utilized in code runs to minimize necessary computer time. The length is sufficient to effectively stop all electrons up to 4 MeV - the maximum energy tested. Because we were not interested in electrons scattered outward, the block radius was set equal to the beam radius.

CODE RESULTS

The Monte Carlo transport code CYLTRAN was used in this study. It is particularly suitable, because it can calculate both electron and photon transport in cylindrical geometry. The problem may involve up to five materials each consisting of a maximum of ten elements without code modification. The problem cylinder may be zoned axially and radially into 100 compartments, if necessary. CYLTRAN is detailed in Reference 1.

Data on materials used in the Faraday cup pertaining to beam stopping power, range and radiation yield up to a maximum beam energy of 4 MeV is compiled in Appendix A. It is generated based on material density, composition, and tabulated cross sections for the various elements.

The largest obstacle in producing statistically significant results from this problem was the exceedingly small ratio of the area of the central wire, which generates the signal, to the beam area. That ratio is $.367 \times 10^{-3}$. The beam is assumed to have a uniform current density and is monoenergetic. Increasing the particle substep size in zones comprising

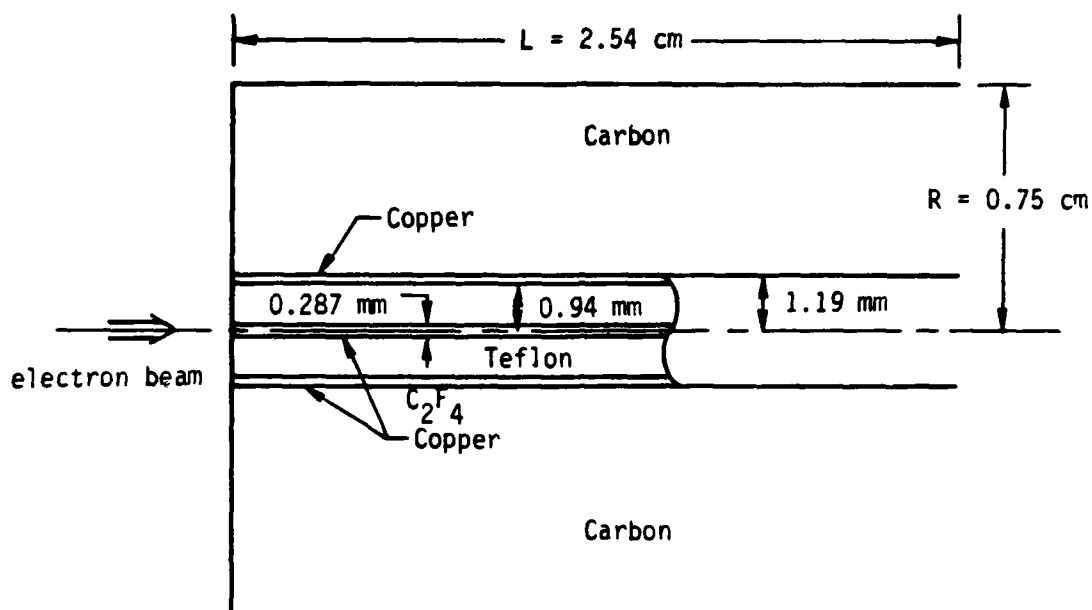


Figure 1. Physical dimensions and material composition of a small aperture Faraday cup. The electron beam is uniformly distributed over the entire cross sectional area.

the coaxial cable improved the statistics only marginally. Eventually, ten batches of 3000 particles were utilized. Further statistical improvement could be obtained by increasing the number of primaries. However, the increased accuracy was not deemed necessary for the present application.

The main purpose of this study was to determine the amount of charge deposited in the central wire due to scattering and secondary electron production versus that predicted from its cross section area. Electrons with energies greater than approximately 10 keV were followed. It was found that the number of electrons deposited was several times larger than could be explained by purely geometric considerations. This is the result of the higher density of copper in relation to the other materials present in the problem. The higher density results in a shorter range and larger stopping power for electrons in the wire than in carbon or Teflon. This effect was observed over the range of energies studied from 1 to 4 MeV. Results are presented in Figure 2. The error bars are too large to derive an exact energy dependence for the ratio of effective to geometric cross sections. However, it appears to be logarithmic in energy. Finally, it is noteworthy that although, depending on beam energy, five to ten secondary electrons are created for each primary electron, they insignificantly modify the charge distribution in the various zones. This indicates that on average the number of knockons created in a zone is equal to the number whose histories are terminated in that zone by dropping below the minimum energy level of 10 keV.

ACKNOWLEDGEMENT

The author is pleased to acknowledge helpful discussions with J. Mack of Los Alamos National Laboratory and J. A. Halbleib of Sandia National Laboratory on the use of the CYLTRAN code.

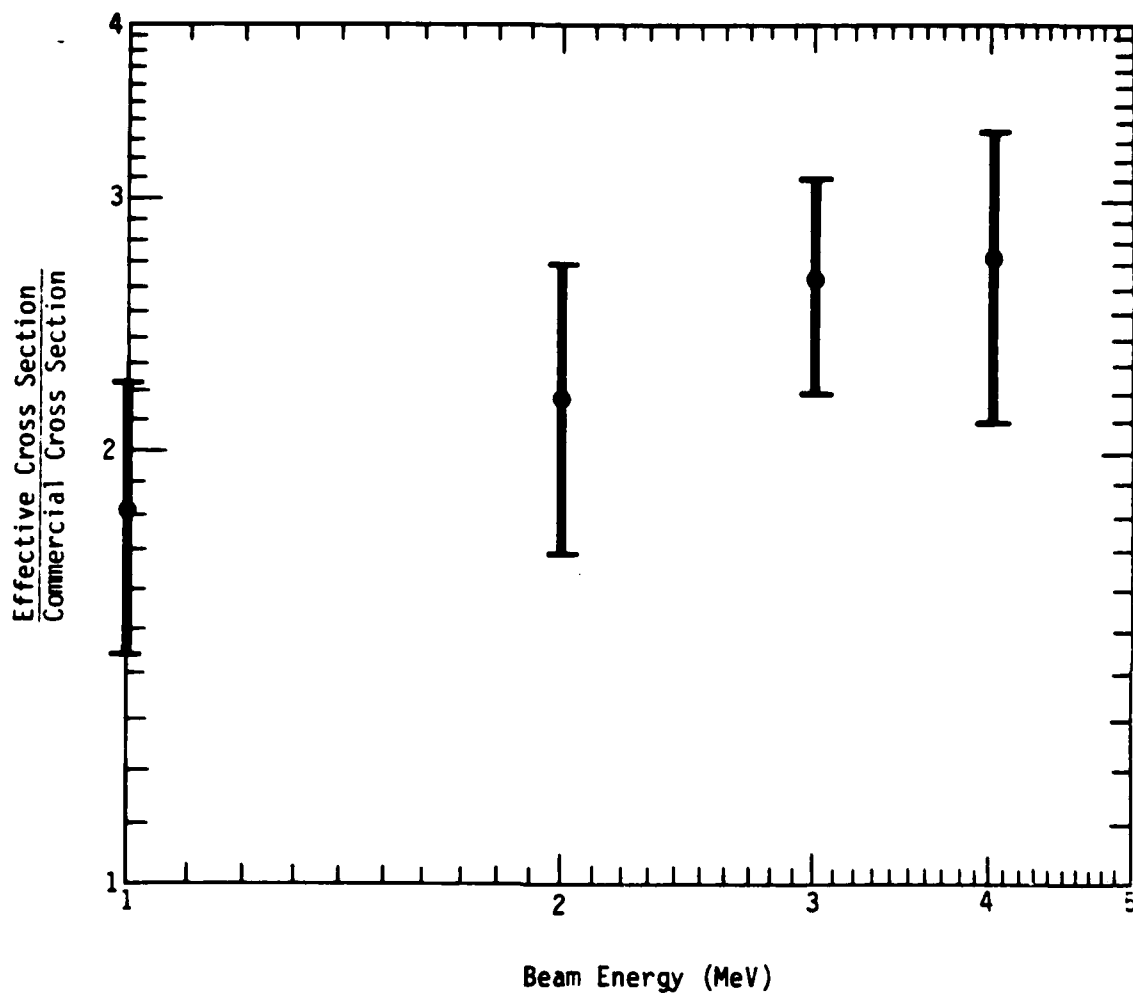


Figure 2. Ratio of effective to geometrical cross section versus electron beam energy.

REFERENCES

1. J. A. Halbleib Sr. and W. H. Vandevender, CYLTRAN: A Cylindrical-Geometry Multimaterial Electron/Photon Monte Carlo Transport Code, SAND 74-0030, Sandia National Laboratories, (1975), unpublished.

APPENDIX D

Monte Carlo Electron Beam Transport in Air

In this appendix, "Appendix A" and "Appendix B" refer to lengthy CYLTRAN outputs in the original report which have been deleted for brevity.

ABSTRACT

The Monte Carlo transport of a 1.5 MeV electron beam in low density and full atmosphere air is studied. At a pressure of 0.5 Torr virtually none of the beam is deflected in 10 meters due to classical scattering or bremsstrahlung. At 760 Torr the beam is scattered in less than 2 meters. The main purpose of this research was to determine the angular dependence of secondary electrons (delta rays) leaving the beam-air interaction region on their energy. At low pressure, excellent agreement is observed between code results and an analytical formula for the scattering angle as a function of delta ray energy down to energies of a few tens of keV.

PROBLEM CONFIGURATION

A monoenergetic 1.5 MeV electron beam of radius 3.8 cm is injected into a cylindrical column of air 10 cm in radius and 10 meters deep. The air is composed of 79% Nitrogen, 20 % oxygen and 1% Argon. The low pressure simulation at 0.5 Torr is sectioned into 80 zones in an attempt to determine where the beam energy is deposited. The high pressure run at 760 Torr is divided into 2 zones from 0 to 2, and 2 to 10 meters. The primary purpose of this was to reduce computer running time, because we were mainly interested in the angular distribution of delta rays (secondary electrons) as a function of their energy. At high pressure, however, the angular dependence was unobtainable.

RESULTS

The Monte Carlo transport code CYLTRAN was used in this study. It is particularly suitable, because it can calculate both electron and photon transport in cylindrical geometry. The problem may involve up to five materials each consisting of a maximum of ten elements without code modification. The problem cylinder may be zoned axially and radially into 100 compartments, if necessary. CYLTRAN is detailed in Reference 1.

Data on air at 0.5 Torr pertaining to beam stopping power, range and radiation yield up to a maximum beam energy of 1.5 MeV is compiled in Appendix A. It is generated based on material density, composition, and tabulated cross sections for the various elements. Transport data for the electron beam in 0.5 Torr air is also given in Appendix A. It shows that all of the electron beam is transmitted. Only those zones within the beam path have any energy from primary electrons deposited in them. Total energy deposition from primary and secondary electrons is .10%. No charge deposition due to primaries is recorded. Charge loss from secondaries leaving the beam volume is .7%. The 500,000 incident beam electrons generate only 3440 secondary electrons - all knockons. This results in rather

poor statistics for delta ray production and angular dependence on energy. Nevertheless, those points which can be plotted show excellent agreement with an already existing, well-known formula for the angular dependence of delta rays. The equation which was derived from momentum and energy conservation, is

$$\cos \theta = \frac{w}{E} \left(\frac{E + 2 mc^2}{w + 2 mc^2} \right)^{1/2} \quad (1)$$

where E is the primary electron energy and w and θ are the delta ray energy and scattering angle. Equation (1) and the points derived from the CYLTRAN program are given in Figure 1.

A second run at full atmospheric pressure was made. CYLTRAN results at this higher pressure are given in Appendix B. In contrast with the prior results, all beam electrons are scattered with virtually all escaping the air cylinder laterally in less than 2 meters. A small percentage (< .2%) are reflected, but none are stopped in the cylinder volume. On average each primary deposits 9.1% of its energy to create .7 knockons/primary. Note, however, that delta rays which are created with energy of less than 10 keV are ignored, so that this number is an underestimate. Because the vast majority of the beam electrons are escaping laterally along with those deltas with sufficient energy to escape the cylinder, it is impossible to determine delta ray angular dependence on energy. Each 10° angular bin has electrons of all possible energies (1.5 MeV to 10 keV) in it. A code update which provides separate data on escaping primary and secondary electrons will be necessary to resolve this problem.

ACKNOWLEDGEMENT

The author is pleased to acknowledge helpful discussions with J. Mack of Los Alamos National Laboratory and J. A. Halbleib of Sandia National Laboratory on the use of the CYLTRAN code.

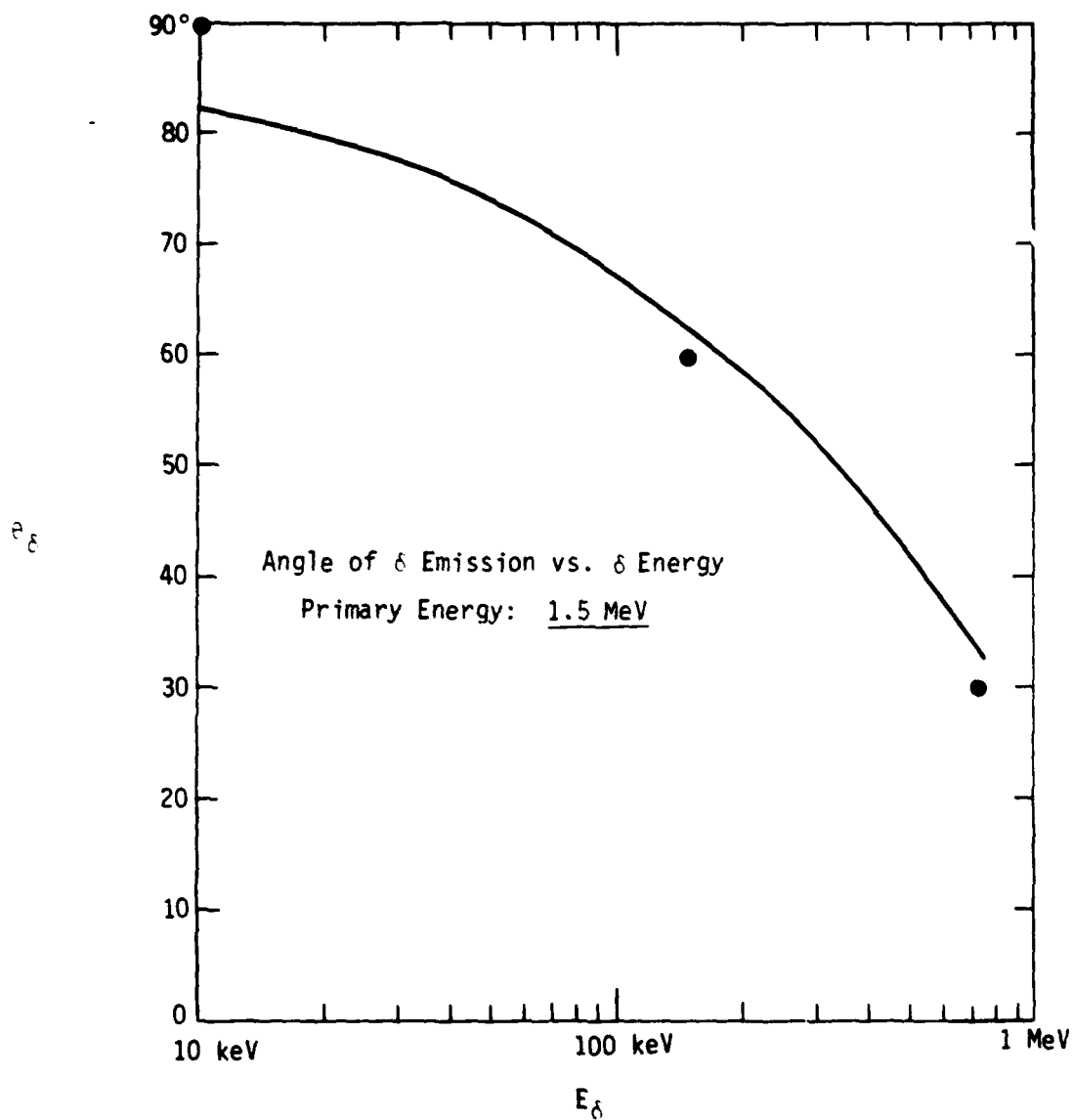


Figure 1. Angular dependence of delta rays on their energy for a 1.5 MeV beam. The solid line results from Equation (1). The points are based on CYLTRAN for air at 0.5 Torr.

REFERENCES

1. J. A. Halbleib Sr. and W. H. Vandevender, CYLTRAN: A Cylindrical-Geometry Multimaterial Electron/Photon Monte Carlo Transport Code, SAND 74-0030, Sandia National Laboratories, (1975), unpublished.

APPENDIX E

Particle Simulation of FX-100 Beam Propagation and Comparison with Experiment

CONTENTS

<u>SECTION</u>		<u>PAGE</u>
I	INTRODUCTION	3
II	NUMERICAL RESULTS	5
III	SUMMARY	13
	REFERENCES	14

LIST OF ILLUSTRATIONS

<u>FIGURE</u>		<u>PAGE</u>
1	Initialization of CPROP at 0.4 Torr. Part (a) shows contours of the beam current density $J_b(\rho, z)$ in units of 17 kA/cm^2 . The values of the contours, labeled by A, B, C, D, E, F, G, are linearly spaced. The z coordinate is in cm. The radial coordinate ρ is related to the physical coordinate r by $\rho = a \ln(1 + r/a)$ where a is the Bennett radius in cm. The Bennett radius is at $\rho = 2.2$. In (b), (c), (d), (e) phase plots of the beam are depicted. The current and voltage ramps in (a) and (e), respectively, are approximately those of the experiment.	4
2	Contour plots of the fields E_z , E_r , in units of 0.51 MV/cm , the B_θ field in units of $0.51 \times 10^4/3$ gauss, the z component of the net current density J_{net} , and the conductivity σ in units of $3 \times 10^{10}/4\pi \text{ sec}^{-1}$, at an air pressure of 0.4 Torr. Avalanching is included in the conductivity model.	6
3	Contour plots of J_{net} , B_θ , and σ with the same normalization as in Fig. 2, also at 0.4 Torr. The avalanching term in the conductivity model has been removed.	8
4	Open shutter photographs of the FX-100 beam at various air pressures (p). The beam is propagating from left to right. In (a), (c) and (d), the camera is positioned 13 cm downstream from the diode. In (b), it is 4.4 m downstream.	9
5	Contour plots of J_{net} , B_θ and σ at 0.125 Torr. Avalanching is included.	11
6	Phase plots of beam after traveling two meters through air at 0.4 Torr, showing nose erosion. Cf. Fig. 1.	12

I. INTRODUCTION

Theoretical investigations in support of the FX-100 experiments have relied on two existing MRC computer codes: CPROP, which is a propagation code, and KMRAD, a linear theory code. The usefulness of these codes is hampered by lack of an air conductivity model whose known range of validity encompasses the 0.1 - 2.0 Torr regime. At present, CPROP uses a conductivity model developed for use at pressures in the range 10^2 - 10^3 Torr.¹

The validity of this model at pressures in the neighborhood of 1 Torr is certainly questionable, but its degree of inaccuracy is unknown. We shall interpret our numerical results in this light and seek to extract information which will guide future efforts.

The CPROP model for the beam is straightforward. The beam is initialized with current and voltage ramps close to those measured experimentally, and is given a Bennett profile in radius (Fig. 1). Due to computing expense and computer core limitations only the first 15 ns of the pulse were simulated. At each location in z (direction of propagation) the beam particles were assigned an emittance based on an approximate formula for the scattering produced by the titanium anode foil.² The initialization of the code is completed by computing the self-consistent fields, conductivity, and return current in the frozen field approximation³ (the initialization is the only stage at which this approximation is used by CPROP).

The code KMRAD requires the input of a beam equilibrium and conductivity profile. It provides linear growth rates and is much cheaper to run than CPROP. It simulates only the body of the pulse and cannot deal with the head of the beam.

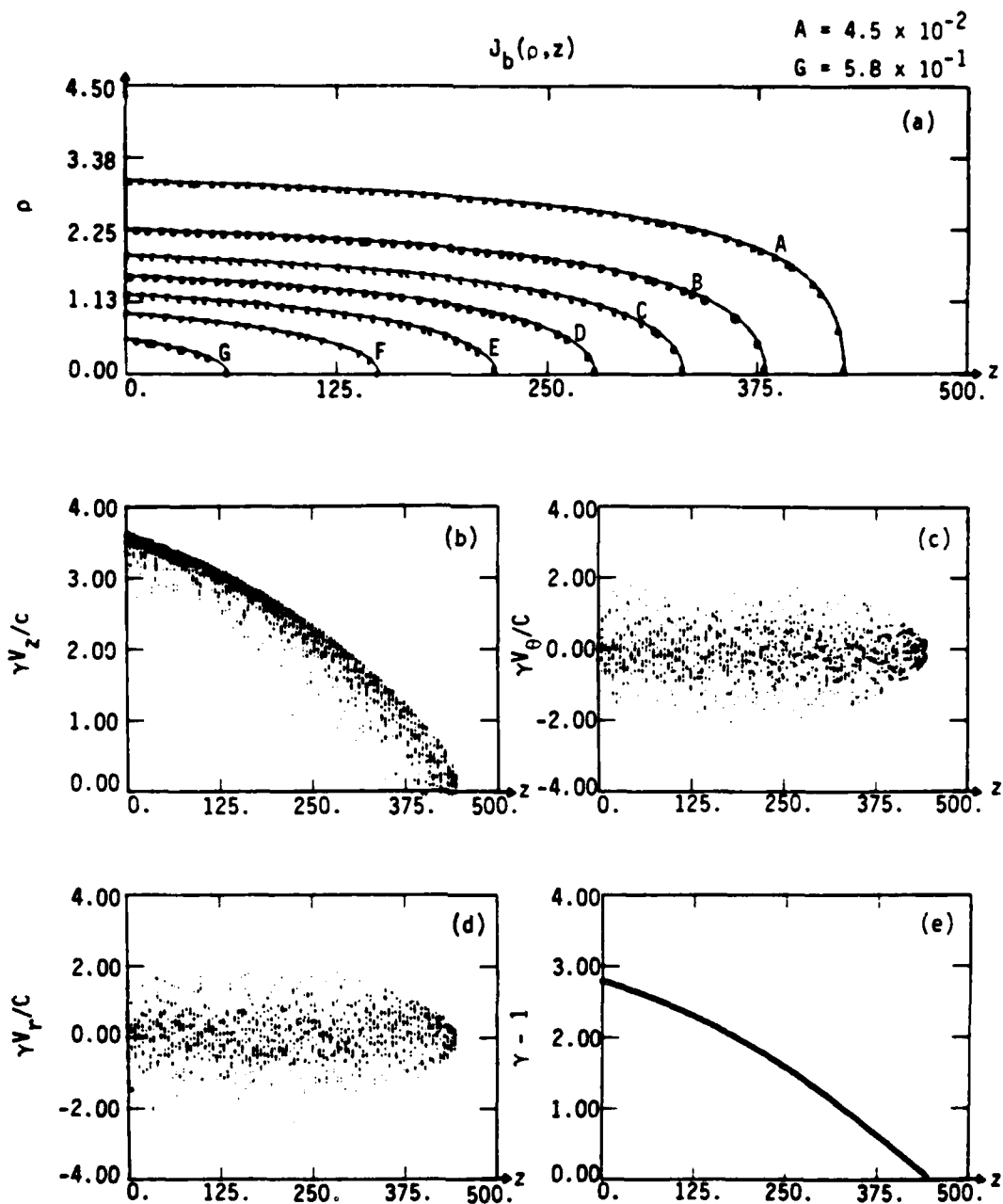


Figure 1. Initialization of CPROP at 0.4 Torr. Part (a) shows contours of the beam current density $J_b(\rho, z)$ in units of 17 kA/cm^2 . The values of the contours, labeled by A, B, C, D, E, F, G, are linearly spaced. The z coordinate is in cm. The radial coordinate ρ is related to the physical coordinate r by $\rho = a \ln(1 + r/a)$ where a is the Bennett radius in cm. The Bennett radius is at $\rho = 2.2$. In (b), (c), (d), (e) phase plots of the beam are depicted. The current and voltage ramps in (a) and (e), respectively, are approximately those of the experiment.

II. NUMERICAL RESULTS

The result of initializing CPROP at a pressure of 0.4 Torr, which is in the experimental propagation window, is shown in Fig. 2. This figure shows the presence of both an electrostatic radial and an inductive longitudinal electric field at the head of the beam where the conductivity is lowest. Comparing Fig. 2 with Fig. 3, we see that the avalanching these fields produce have a large effect on the magnitude and profile of the return current. In Fig. 2, the return current fraction obtained is $f \approx 80\%$ and the return current is more peaked on axis than the beam current so that the B_θ field peaks near the wall instead of at the Bennett radius. When the particles are "let go," the beam expands out radially and loses almost one third of the particles to the wall before contracting. Most of these lost particles come from the nose of the beam. The beam continues to bounce but few particles are subsequently lost. It has been suggested⁴ that at low pressures, avalanching will not occur on a significant scale because of the long mean free path of secondary electrons. With avalanching turned off in CPROP, we obtain $f \approx 35\%$ and the return current has approximately the same radial profile as the beam. If propagated, this beam will start to pinch inward. The experimental evidence tends to favor the inclusion of avalanching in the conductivity model. At pressures near 0.35 Torr, return current fractions of 80 - 95% are observed near the diode. Furthermore, several open shutter photographs taken near the diode (Fig. 4a) show some of the beam blowing off radially.

The large conductivity produced by avalanching leads to a long magnetic decay time for the monopole return current, $\tau \approx 900$ ns (the pulse length is about 120 ns). This means that the resistive instabilities most likely to develop are those with short transverse wavelength λ_\perp , i.e. filamentary instabilities, since the magnetic decay time is proportional to λ_\perp^2 . The linearized simulation code KMRAD was used to look for such instabilities. The open shutter photographs seem to indicate that the fine structure in the beam is azimuthally symmetric so we set $m=0$

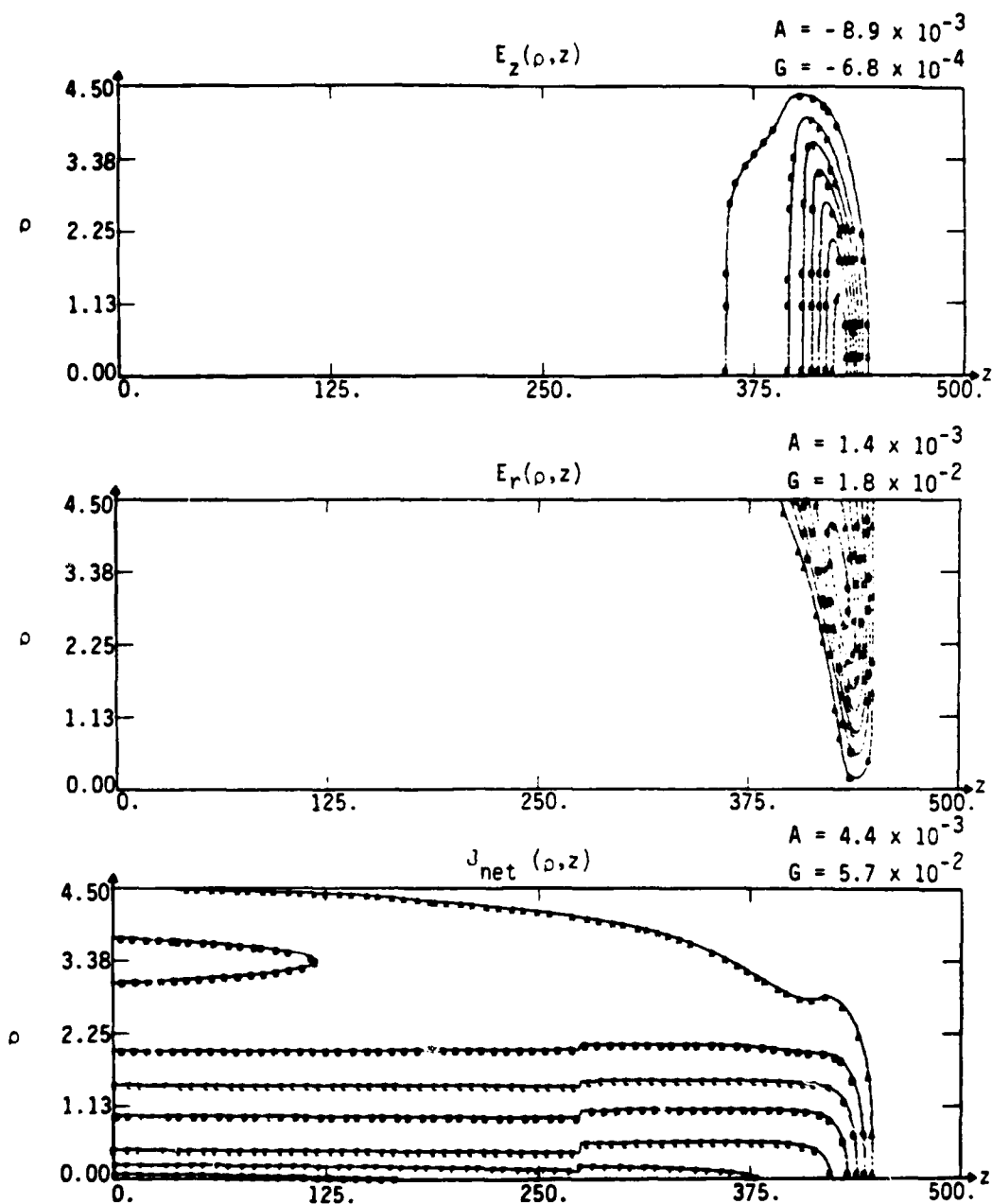


Figure 2. Contour plots of the fields E_z , E_r , in units of 0.51 MV/cm, the B_z field in units of $0.51 \times 10^4/3$ gauss, the z component of the net current density J_{net} , and the conductivity σ in units of $3 \times 10^{10}/4\pi$ sec $^{-1}$, at an air pressure of 0.4 Torr. Avalanching is included in the conductivity model.

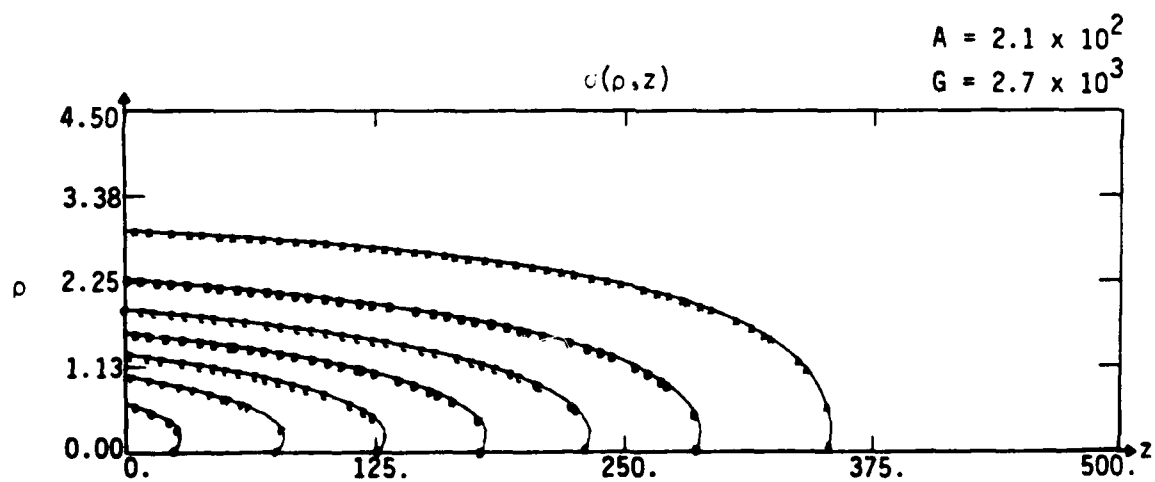
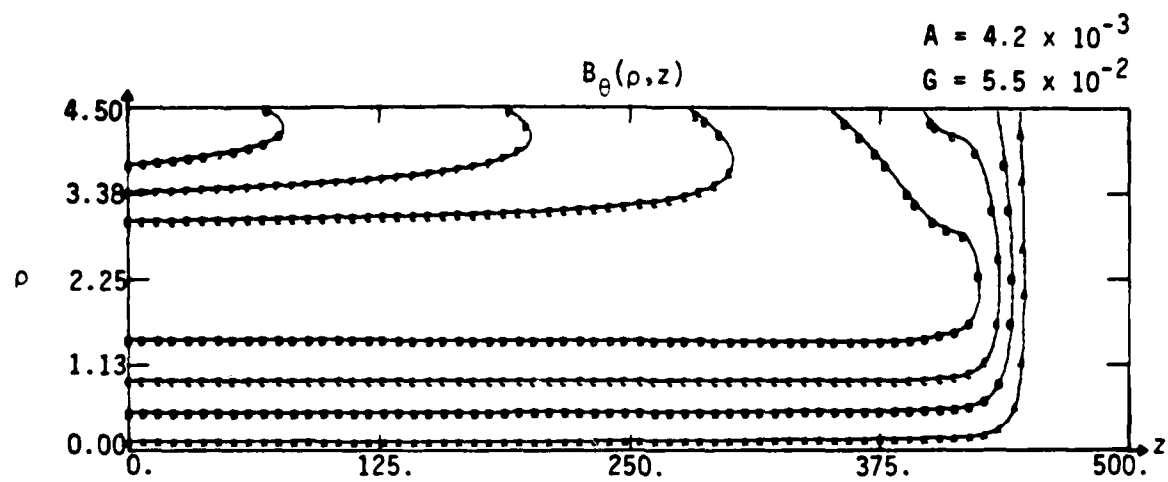


Figure 2 (continued).

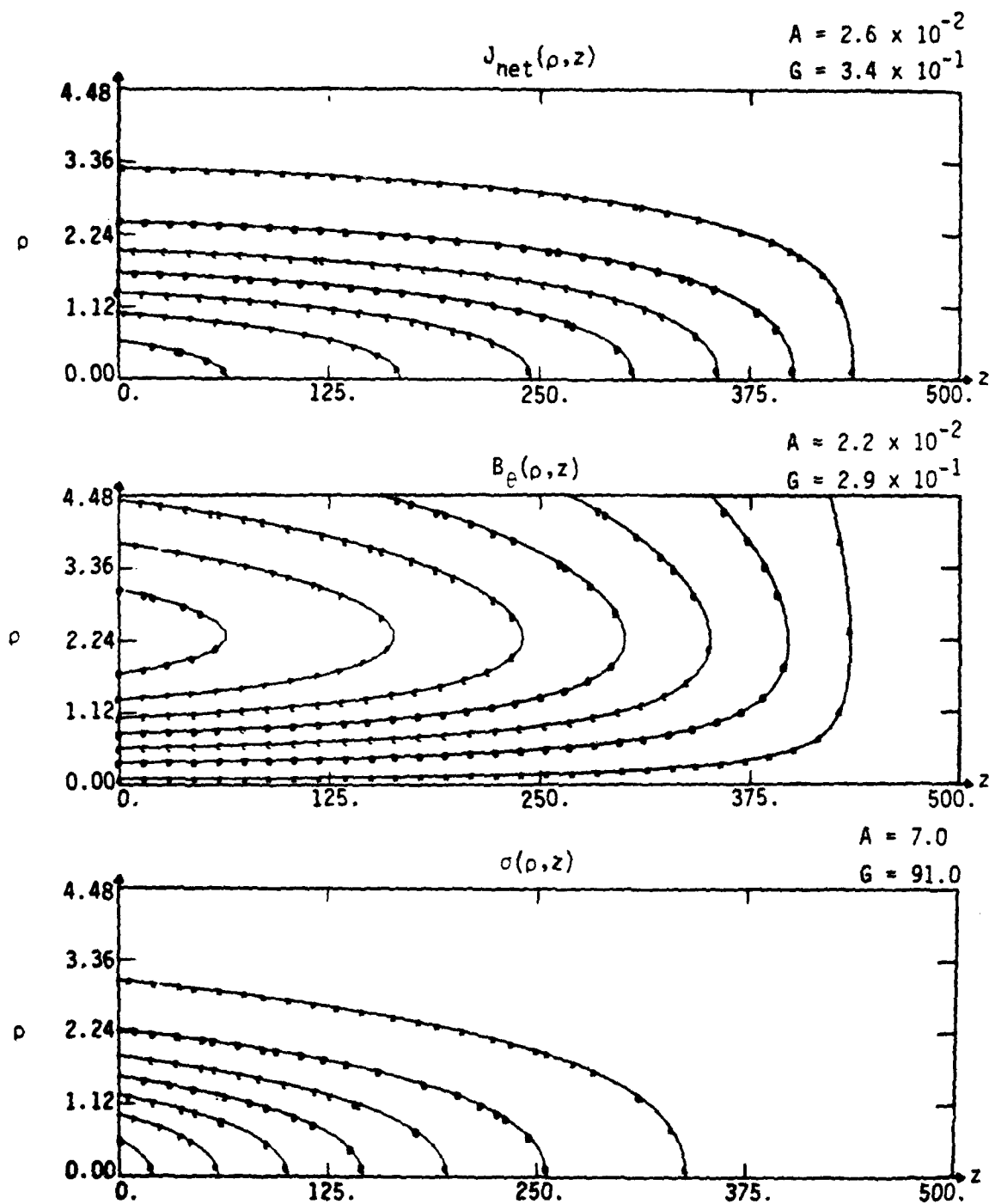
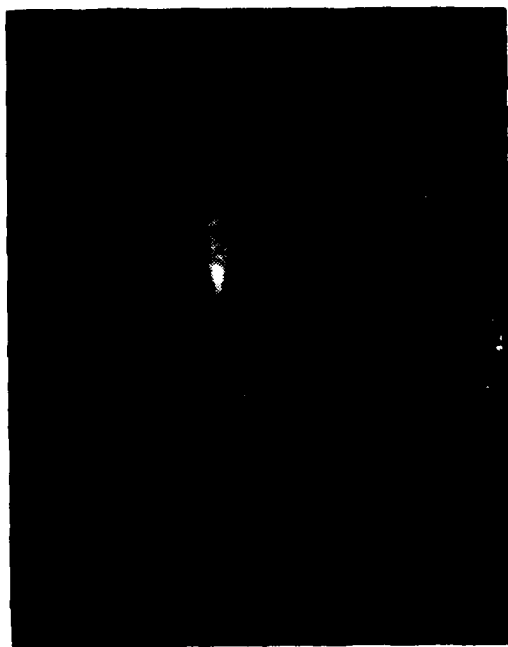
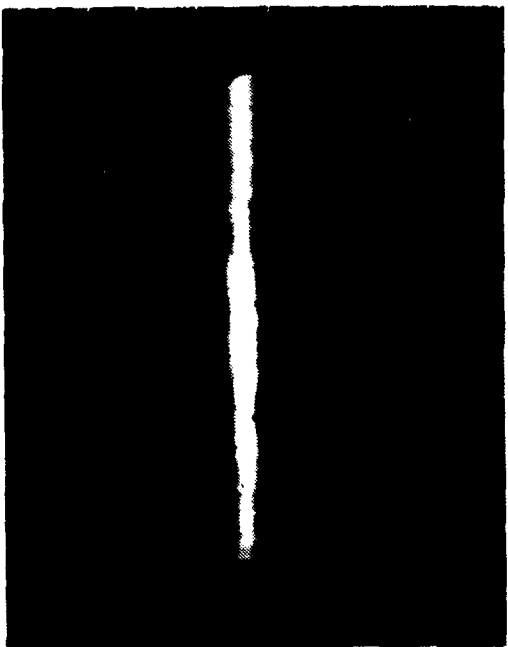


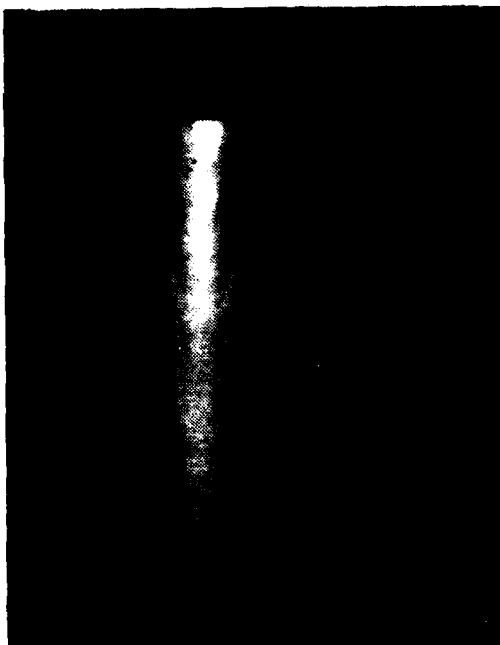
Figure 3. Contour plots of J_{net} , B_e , and σ with the same normalization as in Fig. 2, also at 0.4 Torr. The avalanching term in the conductivity model has been removed.



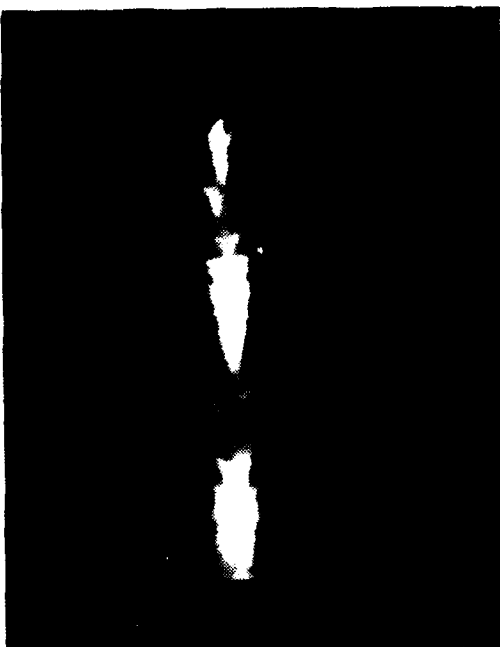
(a) $p = 0.4$ Torr



(c) $p = 0.1$ Torr



(b) $p = 0.4$ Torr



(d) $p = 0.2$ Torr

Figure 4. Open shutter photographs of the FX-100 beam at various air pressures (p). The beam is propagating from left to right. In (a), (c) and (d), the camera is positioned 13 cm downstream from the diode. In (b), it is 4.4 m downstream.

in the simulations. We chose a return current fraction of 95% and the return current and conductivity profiles were assumed to follow the beam profile. The magnitude of the conductivity was taken from CPROP. We found growth rates on the order of $2 \times 10^8 \text{ sec}^{-1}$, with a transverse wavelength of 0.8 - 1 cm (The beam Bennett radius is 3 cm). The growth rates are largest for $k_z \ll k_\perp$ which corresponds to low real frequencies, and low group velocities. The latter implies that the number of e-foldings which the instability can undergo is roughly $N_\gamma = \gamma \tau_p$, where γ is the growth-rate and τ_p is the pulse length. Assuming that our estimate of the growth rate is reasonable, then $N_\gamma \approx 20$ can be attained, which would allow the instability to develop strongly. However, while these calculations are suggestive, the experimental data is not detailed enough to allow us to rule out other explanations for the fine structure seen both in the open shutter (Figs. 4b, 4d) and streak photographs.

At lower pressures, in the neighborhood of 0.1 Torr, CPROP predicts return current fractions of about 70%, and a return current profile close to that of the beam current (Fig. 5). When propagated, the beam collapses to a smaller radius than its initial one of 3 cm. This behavior is qualitatively similar to that observed experimentally. The measured return current fraction is about 45% and the open shutter photographs (Fig. 4c) show a pinched beam with a radius of about 2 cm.

No significant nose erosion is seen experimentally. CPROP predicts that at $p = 0.4 \text{ Torr}$, the beam loses about 1 meter in propagating the first 2 meters, as we see by comparing Figs. 1 and 6. This erosion is at the limit of the experimental precision. The steepening of the longitudinal beam current profile in Fig. 6 gives rise to an increase in the amplitude of E_z at the beam head by a factor of six over its value at $t = 0$ (Fig. 2). This does not lead to a dramatic increase in the erosion rate however since the beam energy γ also increases as one moves back from the head.

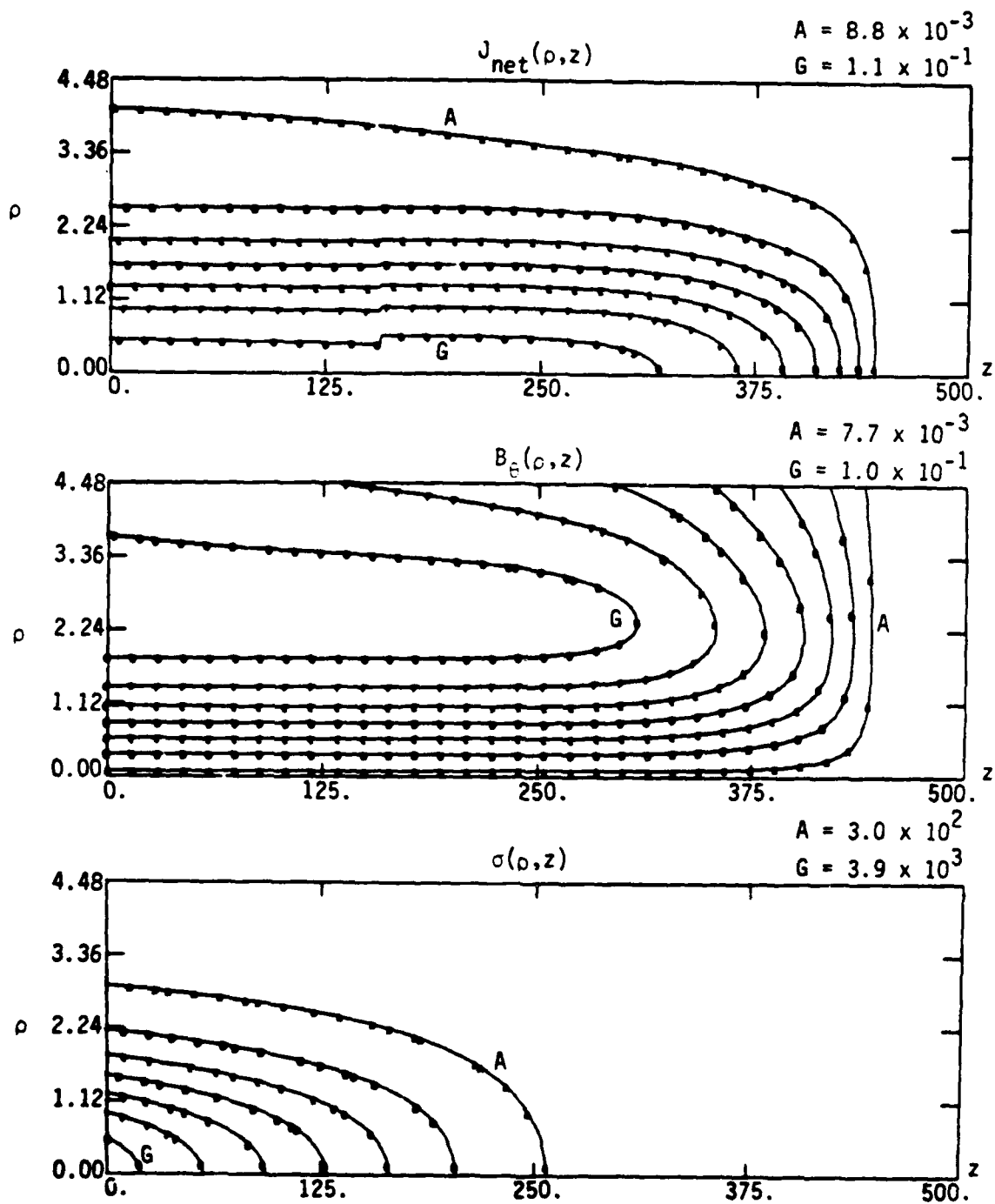


Figure 5. Contour plots of J_{net} , B_{θ} and σ at 0.125 Torr. Avalanching is included.

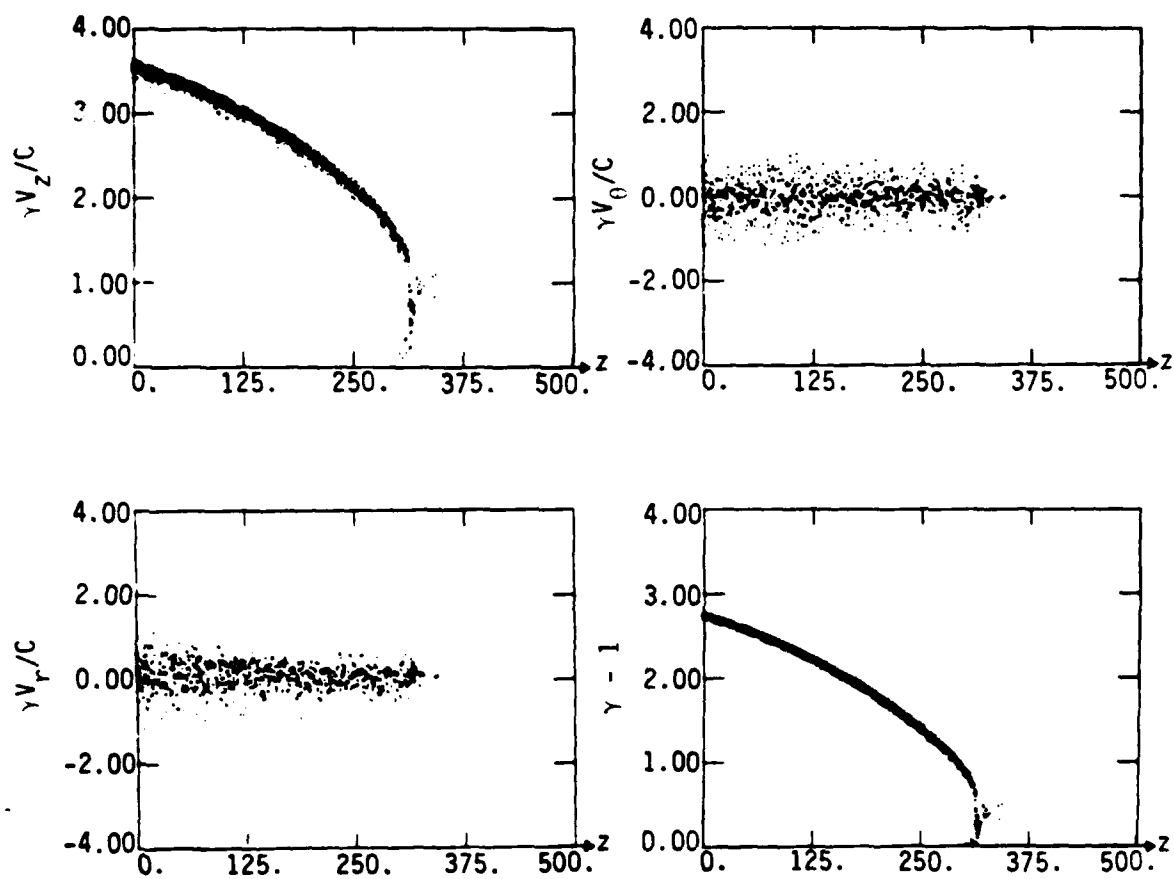


Figure 6. Phase plots of beam after traveling two meters through air at 0.4 Torr, showing nose erosion. Cf. Fig. 1.

III. SUMMARY

We have used the simulation codes CPROP and KMRAD to attempt to explain some of the phenomena seen in the FX-100 experiments. Since we have doubts about the appropriateness of the conductivity model employed, our conclusions are tentative. The simulations show that:

- (1) The large return current fractions measured experimentally near 0.4 Torr and above are consistent with the presence of avalanching.
- (2) At 0.4 Torr and above, avalanching causes the return current to concentrate on axis, and this may be responsible for the radial blowing-off of some of the beam seen in open shutter photographs.
- (3) Resistive filamentation instabilities driven by the large return current fraction may be the source of the fine structure seen in open shutter and streak photographs at 0.2 - 0.4 Torr.
- (4) Near 0.1 Torr the return current profile tends to follow the beam current profile.

To put the above conclusions on a more secure footing, an improved conductivity model is essential. In addition, more carefully controlled experimental conditions would benefit future work. In the present series of experiments, the beam exhibited diverse behavior on different shots under apparently identical conditions.

ACKNOWLEDGMENT

We would like to thank Dr. Winston Bostick and Mr. Ray Lemke for useful conversations.

REFERENCES

1. F. W. Chambers, UCID-18302, Lawrence Livermore National Laboratory (1979).
2. L. E. Thode, private communication.
3. E. P. Lee, UCID-17826, Lawrence Livermore National Laboratory (1976).
4. R. J. Briggs, UCID-19187, Lawrence Livermore National Laboratory (1981).

APPENDIX F

Optical Emission from Intense Relativistic Electron
Beam Excited Air

ABSTRACT

During the low-pressure air propagation experiments with the FX-100 electron beam ($E \sim 1.5$ MeV, $I \sim 40$ kA, $\Delta t \sim 120$ ns, $p \sim 0.1 - 20$ Torr) several diagnostics that used visible light emission were employed. These included time-integrated (open shutter) photography, time-resolved (streak and framing) photography, and time-integrated spectroscopy. In this report we develop a theoretical framework for interpretation of these diagnostics and discuss the results of the measurements.

We find that for propagation experiments in general there may be large contributions to the observed emission from both delta rays and the ionized-channel electrons. The plasma electron contribution is sensitive to temperature and to distortion of the tail of the distribution through high E/p effects. The emitted light can be used to observe the beam current in regions not dominated by high E/p because of the proportionality of the descendent electron density to the beam electron density. However, radial resolution of the current density profile may be blurred by the contribution of delta rays ejected at large angles. The temporal response of the emitted light can be expected to faithfully reproduce the beam current history only when the pressure is higher than a minimum, which depends on the highest frequency of interest in the beam current.

From the spectral measurements we have identified observed red emission to be atomic oxygen at 6157Å, we have identified a large number of N_2 , N_2^+ and N^+ emissions, and we have shown the atomic line radiation to emanate from a region of limited radial extent. In the streak photographs we have seen some results of the magnetic field collapse at the end of the beam. We have observed that the molecular emissions temporally track the beam and that the atomic emission persists at late times, after the beam has passed. The framing photos also show the collapse of the field and radiating volume, and the long history of the atomic emissions.

CONTENTS

<u>Section</u>		<u>Page</u>
	ABSTRACT	i
I.	INTRODUCTION	1
II.	THEORY OF VISIBLE EMISSION FROM ELECTRON BEAMS PROPAGATING IN AIR	3
III.	EXPERIMENTAL RESULTS AND DISCUSSION	12
	REFERENCES	37

I. INTRODUCTION

Observation of visible light emission is a commonly used diagnostic technique in high-intensity relativistic electron-beam propagation experiments. Photography is an obvious and useful way of observing the behavior of self-luminous experiments, and much information has been obtained from both high-speed and time-integrated photography. For example, estimates of the hose-instability growth length, betatron wavelength, and beam radius have been obtained from photographic records.¹⁻³ Visible light emitted in beam experiments has also been observed by other methods such as wavelength-filtered fast photodetectors measuring the total light emitted from a region of limited axial extent.⁴ For some beam and air pressure parameter regimes, these measurements were found to be correlated with the total beam current, which suggests that this technique could be employed as a nonperturbing beam-current monitor ("optical Faraday-cup").⁵⁻⁶ Furthermore, if the excitation of air fluorescence by primary beam electrons is indeed the dominant source of light, then the analysis of high-speed streak or framing camera photographs would be a convenient method for obtaining time-resolved details of the beam current density distribution.

As indicated, there is a wealth of information to be gained from the proper interpretation of optical emissions. The purpose of this report is two-fold: to develop a rough theoretical basis for such an interpretation, and to present the results of optical measurements from recent FX-100 experiments. In Section II the underlying assumptions about optical emissions are reviewed, excitation mechanisms other than by the primary beam identified and the importance of these mechanisms estimated.

We will show that for propagation experiments in general there may be significant contributions to the emitted light resulting from delta rays (knock on electrons) and ionized-channel electrons. The contribution from the channel-plasma electrons is sensitive to the temperature and can be enhanced by distortions of the high-energy tail of the distribution by large electric fields. We will develop the necessary conditions on the air pressure that must be met in order to reproduce the beam current temporal history with high fidelity. We will conclude that because of the proportionality of the descendent-electron distribution to the beam electron distribution, reproduction of the beam current is possible within these constraints, although delta rays can lead to a blurring of the radial current profile. In Section III experimental results are presented and discussed. These results include spectra, streak photographs and framing photographs. Observed red emission from the low-pressure FX-100 experiments was spectrally identified as an atomic oxygen line. Additionally, we identified a large number of singly ionized nitrogen lines confined in a region much smaller than the beam radius, as well as the typical beam-excited molecular nitrogen bands seen over the entire radial extent of the beam. The atomic emissions were seen to persist for times much longer than the passage of the beam, leading to an "over-exposure" of persistent stationary structure in the time-integrated open-shutter photographs.

II. THEORY OF VISIBLE EMISSION FROM ELECTRON BEAMS PROPAGATING IN AIR

In high-density air propagation experiments with p_0 greater than a few Torr the emission is dominated by the molecular nitrogen purple-blue light emissions.⁷ Of these, the N_2^+ first negative (1^-) band emission at 3914 Å and the N_2 second positive (2^+) band emission at 3371 Å are transitions that have been suggested as useful for beam diagnostics. The excited states of these transitions are rapidly quenched and it is assumed that the time history of these transitions accurately reflects the time history of the electron density that excites the molecules. With this assumption and if the emission results from only the beam primaries, the light emitted from an axially limited region measures the beam current and accurately maps the radial distribution of the high-energy beam.

Possible sources of error in these interpretations can result if there is significant excitation of the molecular states by the secondary (delta-ray) electron population or by the weakly-ionized channel electrons. The cross sections for excitation generally have thresholds of about 5- 20 eV, have maxima near 70-90 eV, and fall off as $\ln E/E$ in the high energy limit.⁸ Figure 1 presents the excitation cross section for the N_2^+ first negative band. The delta-ray distribution, which extends outside of the beam radius, will provide a significant contribution to the excitation because of the large proportion of delta-rays with energies near the excitation cross-section maximum. This is evident from inspection of the delta-ray distribution⁹ presented in Figure 2. Furthermore, light emitted from a particular axial location is to some degree dependent on delta rays created at a different axial position. Thus, the spatial dependence of the emission intensity is highly dependent on the spatial distribution of delta-ray secondaries, which tends to mask the correlation with primary beam excitation. Finally, the weakly-ionized channel electrons can contribute strongly to the observed light; as a result of high E/p (electric-field to pressure ratio) distortion of the channel-plasma electron distribution, there may be a significant number of electrons with energies greater than the threshold or near the peak of the excitation

cross section. As seen in Figure 3, without the high E/p effects the overlap of the plasma electron distribution and the excitation cross-section is inconsequential for temperatures less than 1 eV. These secondary electrons can produce a light intensity competitive with that produced by primary beam excitation and correct interpretation of visible observations thus depends on an understanding of these effects.

Thus, the problems of interpreting measurements of visible light emission are somewhat analogous to the problems that arise in attempts to interpret measurements of currents using Rogowski belts or B-dot probes. These inductive current diagnostics are sensitive only to the net current (sum of primary beam and secondary return currents) and additional diagnostics must be employed to resolve each component. The light emission diagnostics are, in turn, also sensitive to a weighted net current (sum of primary beam and secondary currents weighted by effective excitation factors).

There are two steps in unfolding beam parameters from the observed emission. The first is to determine the position dependent excited state population density from the given visible intensity. The intensity of visible radiation emitted by an optically-thin line radiator with thickness z is

$$I = \frac{h\nu}{4\pi} A \int_0^z N_{ex} dz, \quad (1)$$

where $h\nu$ is the photon energy, $A(s^{-1})$ is the spontaneous emission transition probability, and $N_{ex} (cm^{-3})$ is the position dependent excited state population density. The spatial variation of N_{ex} can be obtained by tomographic inversion techniques (eg. Abel inversion for cylindrically symmetric systems such as beams). Photography can thus provide an accurate measurement of the time-integrated spatial distribution of excited states if an optical filter at wavelength $\lambda = c/\nu$ is used. Time resolution can be obtained with a streak or framing camera. The remaining question is that of establishing beam parameters through a knowledge of N_{ex} .

For the optically thin radiator, radiative excitation can be neglected, and the excitation to the upper state by collisions occurs at a rate given by $\langle \sigma n_e v \rangle$, where σ is the (velocity dependent) excitation cross section. The average is taken over the electron distribution in velocity space, n_e . The total density distribution is composed of n_b (primary-beam electrons), n_δ (delta-ray secondary electrons) and n_p (ionized-channel plasma electrons); each has a very different velocity distribution. The upper state of the transition can be de-excited collisionally (in addition to radiating) and the rate for this process is $q_0 N_0$, where N_0 is the density of air molecules, and q_0 is the quenching coefficient in air.

Including these processes and neglecting other means of populating the upper level (such as recombination) one gets the rate equation for the excited state population,

$$\dot{N}_{ex} = \langle \sigma n_e v \rangle N_0 - A N_{ex} - q N_{ex} N_0 \quad (2)$$

Equation (2) can be rewritten as

$$\dot{N}_{ex} + N_{ex}/\tau = \langle \sigma n_e v \rangle N_0, \quad (3)$$

which has the solution

$$N_{ex} = \exp[-t/\tau] \int_0^t \exp[t'/\tau] \langle \sigma n_e v \rangle N_0 dt' + C \exp[-t/\tau], \quad (4)$$

The time constant, τ , in equations (3) and (4) is

$$\tau = [A + q N_0]^{-1} \quad (5)$$

Several features of Equations (2)-(5) that relate to the applicability of optical emission diagnostics are worth pointing out. The lower pressure

for practical use of this radiation diagnostic is the pressure at which quenching first dominates τ . For pressure greater than this minimum and time variations of the electron density much larger than τ , the density of excited states is independent of air pressure and is given by

$$N_{ex} \sim \langle \sigma n_e v \rangle / q \quad (6)$$

As an example, we will use the first negative emission of $N_2(3914 \text{ \AA})$; for this transition the spontaneous emission coefficient is $A = 1.24 \times 10^7 \text{ s}^{-1}$ and the quenching coefficient in air is $q = 5.1 \times 10^{-10} \text{ cm}^3 \text{ s}^{-1}$ (Ref. 10). Therefore, quenching dominates τ for air densities $N_0 > A/q = 2.4 \times 10^{16} \text{ cm}^{-3}$ ($p_0 > .74 \text{ Torr}$ at 20°C). For full atmospheric pressure, $\tau = 78 \text{ ps}$, which is much faster than the time variations in present experiments. For comparison the second positive emission of $N_2(3371 \text{ \AA})$ ($A = 1.1 \times 10^7 \text{ s}^{-1}$ and $q = 6.6 \times 10^{-11} \text{ cm}^3 \text{ s}^{-1}$)¹¹ has a minimum useful pressure of $\sim 5.1 \text{ Torr}$ ($\tau \sim .60 \text{ ns}$ for 3371 \AA emission in full density air).

Equation (5) can be solved for N_0 , the minimum neutral number density required to assure a required response time t_r .

$$N_0 = \frac{1}{qt_r} - \frac{A}{q}$$

For $N_2^+(1-)$ and $N_2(2^+)$ this becomes, respectively,

$$p = \frac{59.4}{t_r(\text{ns})} - .74 \text{ Torr} \quad (7a)$$

$$p = \frac{459.}{t_r(\text{ns})} - 5.05 \text{ Torr} \quad (7b)$$

Equations (7) are plotted in Figure 4. This figure is useful for the determination of the minimum pressure for which the emission intensity can be expected to faithfully follow an experimental density variation.

Furthermore, this figure indicates the expected delay time between the onset of a rapid electron density increase at low pressures (where the density rise time is much less than t_r given by Eq. (7)) and the appearance of the optical emission. For example, at pressures less than 1 Torr, the emission from density increases occurring in less than ~ 10 ns would have a rise time of $\sim 20 - 30$ ns. This lack of temporal fidelity is a further limitation on the pressure range for use of emission diagnostics.

To summarize, to be assured that the emission intensity faithfully reproduces the electron density variation, one is restricted to pressures greater than given in Fig. 4 for any expected time variation of the electron density, and to insure independence of the emission from the neutral gas density the pressure must be greater than 0.74 Torr (for 3914 Å light) or 5.1 Torr (for 3371 Å).

Assuming that the density variations in the experiment satisfy the foregoing restrictions, then the observed emission intensity will be proportional to $\langle n_e v \rangle$ (Equation (1) and Equation (6)). However, n_e is composed of n_b , n_s and n_p ; the beam, secondary and plasma electron distributions; each with its own widely differing energy distribution. The observed fluorescence is a combination (both temporally and spatially) of these, and any information about n_b (or $j_b = \langle n_b v \rangle$) must be further unfolded.

To unfold the observed fluorescence first consider the plasma electrons. At the higher pressures a significant fraction of the plasma electrons result from direct ionization and, therefore, have a density proportional to the beam density. These electrons cannot distort the optical measurements unless there exists a mechanism for locally distorting the light intensity resulting from their excitation of the molecular levels. Such a mechanism is found in high E/p effects. For high electric field-

to-pressure ratios (E/p) a large number of particles go into the high energy tail of the distribution raising the effective temperature of the electrons.¹² For $E/p = 10 \text{ V cm}^{-1} \text{ Torr}^{-1}$ in air, $T_e^{\text{eff}}/T_{\text{gas}} \sim 50$ (Ref. 13). Because of high effective temperature electrons with more than the threshold for excitation ($\sim 11 \text{ eV}$ for $\text{N}_2(2^+)$) will be present. The large number of plasma electrons relative to the beam electrons ($\sim 10^3$) could contribute greatly to the observed emission. Because of the time dependent fields and skewed distribution, a simple but accurate estimate of these effects cannot be made here.

However, a rough estimate of $\langle n\sigma v \rangle$ can be made for both the plasma and the beam. The ratio of these gives the relative amount of excitation due to both sources. The average for the plasma electrons can be done by using a Maxwellian distribution and a linear fit for the excitation cross section near its threshold, if the Maxwellian temperature is much less than the threshold energy. Then,

$$\begin{aligned} \sigma &= aE + b & E > E_0 \\ &= 0 & E \leq E_0 \end{aligned} \quad (8)$$

For $\text{N}_2^+(1-)$, $E_0 \sim 18.8 \text{ eV}$ and $a = 10^{-18} \text{ cm}^2 \text{ eV}^{-1}$ and $b = 1.88 \times 10^{-17} \text{ cm}^2$. The average for beam electrons was calculated from a monoenergetic distribution. The result is

$$\frac{\langle n\sigma v \rangle_p}{\langle n\sigma v \rangle_b} = \left(\frac{n_p}{n_b} \right) \left(\frac{8kT}{\pi m_e} \right)^{1/2} \frac{a(E_0 + 2kT)}{\sigma(E_0)} e^{-E_0/kT} \quad (9)$$

where the subscripts p or b refer to plasma or beam electrons, n is the particle density, kT the plasma temperature, E_b the beam electron energy, mc^2 the electron rest mass, $\sigma(E_b)$ the excitation cross section at the beam energy, E_0 the threshold energy for excitation, and b is the slope of the cross section at threshold. For the $N_2^+(1-)$ band, assuming that $n_p/n_b = 10^3$ and 1.5 MeV beam electrons,

$$\frac{\langle n\sigma v \rangle_p}{\langle n\sigma v \rangle_b} = 37.2(kT)^{1/2} (18.8 + 2kT) e^{-18.8/kT} \quad (10)$$

For 20 MeV beams

$$\frac{\langle n\sigma v \rangle_p}{\langle n\sigma v \rangle_b} = 27.9(kT)^{1/2} (18.8 + 2kT) e^{-18.8/kT} \quad (11)$$

The 1.5 MeV result is plotted on Figure 5. For plasma temperatures greater than 2.6 eV, the excitation from plasma electrons is greater than from beam electrons. The curve is very steep between 1 and 3 eV and probably quite sensitive to the model. The curve is, therefore, intended only as a rough guideline and an indication of the magnitude of possible plasma electron effects. What is clearly evident is that the light resulting from the plasma electron distribution can equal that resulting from beam primaries if the effective plasma temperature is only slightly increased by high E/p effects. That is, the emission resulting from plasma electrons is greatly and non-linearly enhanced in regions of high E/p. A 20 MeV curve could be similar to the 1.5 MeV curve only scaled in magnitude by .75. On the scale of Figure 5 the two would be almost indistinguishable.

Next we examine the delta-ray (knock-on) secondary electrons. Bombarding N_2 with 1.5 MeV electrons and monitoring the $N_2^+(1-)$ emissions, Hirsch, et al., found that roughly 1/3 of the emission was due to primaries and 2/3 due to secondaries. A theoretical estimate of $\langle n\sigma v \rangle_\delta / \langle n\sigma v \rangle_b$ can be made to compare to the experimental results. Again $\langle n\sigma v \rangle_b$ is calculated by characterizing the distribution as monoenergetic and using the cross section evaluated at the beam energy. The number of particles, n , is left unspecified,

$$\langle n\sigma v \rangle_b = 1.8 \times 10^{-19} n_b \quad (12)$$

For every n_b that forms N_2^+ , there are n_b delta electrons formed and a total of secondaries, tertiaries, etc. of $\sim 3 n_b$. By integrating over the electron distribution and cross section

$$\langle n\sigma v \rangle_\delta = 3.9 \times 10^{-19} n_b \quad (13)$$

This gives 32% of the emission due to primaries and 68% due to secondaries, in very close agreement with experimental results. At 20 Mev these fractions are 38% and 62%, respectively.

Considering the case of a 20 MeV beam of .1 cm radius in full density air, neglecting the fields gives half the energy of the secondaries deposited within a radius of .1 cm (in the beam) and half outside of the beam. Considering only primaries and secondaries, 1/3 of the $N_2^+(1-)$ emission is due to primaries, 1/3 due to secondaries in the beam and 1/3 due to secondaries outside the beam. The effect of the delta-ray secondaries is, therefore, to blur the radial spatial resolution. The time history of the total light from a region of limited axial extent will, however, not be significantly different than the time history of the beam current as a result of delta ray effects because of the proportionality of

n_b and n_g . Thus, an optical Faraday cup based on this principle should not be affected by delta-ray electrons. Indeed, the additional signal resulting from delta ray secondaries helps to enhance the wanted signal (proportional to n_b) compared with the "noise" (proportional to n_p , for example).

In summary, there are large contributions to the observed emission from both delta rays and the plasma electrons. The contribution from the plasma is very sensitive to the temperature and high energy tail of the distribution and the delta ray contribution differs spatially from the beam contribution. Although much information must be decoupled to obtain beam parameters from optical emissions, the emissions do appear to be good monitors of total energy deposition. In regions not dominated by high E/p effects, the total (radially integrated) light from a region of limited axial extent can probably be used as an "optical Faraday cup" to measure $I_b(t)$ because of the proportionality of the descendent electron density to n_b . The temporal response of such a diagnostic can be expected to follow I_b only at pressures higher than a minimum determined by the most rapid fluctuations of I_b .

III. EXPERIMENTAL RESULTS AND DISCUSSION

To this point the discussion has centered on the interpretation of observed emissions, primarily $N_2(2^+)$ and $N_2^+(1^-)$. Also important, and of future diagnostic use, is the understanding of the gross features of open shutter and high-speed photographs. In this section we will attempt to understand some of these features by examining optical measurements made during the course of propagation experiments using the AFWL FX-100 accelerator. The parameters of these experiments appear in Table 1.

Two striking features on some open-shutter photographs are color changes (red and/or green-blue) and feathering (see Figure 6 for this effect). Time integrated spectra were obtained to identify the source of this emission. Streak and framing photographs give both a temporal history of the emissions and an indication of feathering.

Spectral measurements were taken at 0.35 Torr (near the 0.5 Torr air pressure for maximum energy transport; i.e., "middle" of the propagation window). Because of time constraints spectra at other pressures could not be taken. The spectra were taken after propagating 4.5 m. They were integrated over 10 shots. The dispersing instrument used for these data was a Jarell-Ash 1/2-meter Fastie-Ebert spectrometer with a 1200 groove/mm (5500 Å blaze wavelength) grating. The recording medium was Polaroid type 47 film.

Figures 7-11 display densitometer scans of the photographs of the spectral lines, and Table 2 lists the identified lines and bands and their designations. There are three major wavelength regions where emission are observed: 3750-4450Å, 4600-4710Å, and 6157Å. Lower wavelengths were not recorded because the acrylic windows used have a sharp cutoff at

- 3500Å. The lowest wavelength region is the characteristic purple-blue emissions and is dominated by N_2 and N_2^+ . The band emission intensity in these regions was probably sufficient to saturate the film response. The wavelength region 4600-4710Å is dominated by singly ionized atomic nitrogen (N^+). Emission in the red wavelength range is dominated by a line at 6157Å.

The red (6157 Å) emission appears only in a narrow range of pressures. In the FX-100 experiments the red emission is observed between - 0.1 + 0.8 Torr, and is not observed at any pressure in pure N_2 experiments. At higher and lower air pressures the emission is the characteristic purple-blue from N_2 and N_2^+ .

The 6157Å emission line is from atomic oxygen, and was the only neutral atomic emission observed. The oxygen transition is $4d^5D - 3p^5P$ while the ground state is $2p^3P$. Although forbidden transitions such as $3p \rightarrow 5D$ frequently occur through scattering, it seems unlikely that for the most intense oxygen transition the upper state would be populated in this manner. Probably, the beam produces O^+ , which recombines with electrons to form oxygen in the $5D$ state. This interpretation is also consistent with no emission being observed at higher pressures. O^+ would be lost through charge exchange to O_2 which is exoergic, so there would be no recombination to form $O(5D)$. Similarly, at very low pressures, recombination would not be as likely because of the reduced collision frequency. Figure 12 is a more detailed densitometer scan for this oxygen line, actually 3 lines at 6156.0, 6156.8 and 6158.2Å corresponding to $J = 1, 2$ and 3 .

Figure 13 shows two densitometer scans over the same portion of the spectra. The bottom one was taken along the axis of the beam as were all the earlier scans. The upper scan corresponds to a radial position 0.63 cm off axis. At this radial position the atomic nitrogen (N^+) lines were no longer apparent. This was a general characteristic of the

spectra. The spatial extent of the atomic lines was much smaller than for the molecular lines. The molecular emission had a radius of ~ 30 mm, the atomic emission ~ 2.4 mm, and the radius of the beam was ~ 30 mm. This is indicative of a very high electron-distribution average energy near the axis, because the electron energy needed to dissociate and ionize the N_2 molecules is ~ 24.3 eV.

An Imacon 790 image-converter camera was used to obtain streak and framing pictures of the emission. These observations were made through the same window used for the spectrometer but were not simultaneous with spectral measurements. The image-converter camera had a rather long delay after triggering, and in order to record the head of the beam it was necessary to delay the emission light by folding the optical path through 2.2 m and locating the camera next to the FX-100 output switch. The camera trigger was derived directly from the light emitted by the FX-100 output switch. This physical arrangement provided the required delay of the beam emission signal through the beam vacuum-diode delay, beam-propagation delay, and optical-path delay. A 1200-mm Questar collection lens used at the camera provided adequate magnification and light intensity without the use of intermediate field or relay lenses.

Figure 14 is a streak photograph taken at 0.35 Torr. The abrupt decrease in the diameter of the emission is at ~ 120 ns, the length of the beam pulse. It is clear from this photograph that the intense emission near the axis persists in stationary patterns for long times after the beam has passed through the region. The radial contraction is probably due to the collapse of the magnetic field set up by the beam. Because the spectra had shown the spatial dependence of the atomic and molecular emissions to be different, streak photographs were made with wavelength filters with passbands at typical molecular and atomic emission wavelengths. One filter had a passband centered at the N^+ band at 4278Å and these photographs showed that the molecular emission turned off at 120 ns (at the same time that the beam turned off). This light was observed to originate over the larger

radial extent previously observed in the time-integrated spectral measurements. The other filter allowed for the transmission of the atomic nitrogen lines between 4607Å and 4643Å. In agreement with the spectra, the atomic emissions were of limited radial extent. Unfortunately, the intensity of the atomic emissions was low and the starting time for these could not be accurately determined. They appear to start ~ 100 ns after the beam head and continue for more than 800 ns after the beam passage.

Although plasma currents continue to flow in the gas long after the beam passage, the L/R decay of these currents is too rapid (100 - 200 ns) to explain the observed afterglow emission from excited atomic states, which persists for more than 800 ns. Another possible mechanism for the continued excitation of these states is the collisional transfer of energy initially stored as molecular vibrational energy (T_v) by beam or delta-ray electron excitation. However, the most likely explanation for the persistence of atomic states such as N^+ after their initial formation is simply the extremely slow deionization rate at the low air pressures of these experiments. To show this, the deionization times for the various collisional reactions¹⁴ as well as radiative recombination¹⁵ are graphed for a wide range of dry air pressures in Fig. 17. Also given is the scaling of this time with neutral gas and electron density and temperature.

For calculation of the N^+ deionization times that are graphed in Figure 17 the gas temperatures (T_g), electron temperature (T_e) and electron density, n_e , were chosen to give the fastest rates for realistic values of these parameters. That is, it is unreasonable to assume that the N^+ concentrate could be depleted more rapidly than indicated by the graph. It is clear from this figure that the observed afterglow from N^+ states for > 500 ns in 0.35 Torr air is not surprising. Note that, although deionization of high pressure and weakly ionized air is controlled by neutral association, deionization at pressures higher than ~ 2 Torr

can be dominated by three-body recombination if the fractional ionization ($f = n_e/n_a$) is great enough. However, at the pressures relevant to the FX-100 experiments reported here the rate determining reactions for N^+ deionization are $N^+ + O_2$ reactions. All deionization times increase with temperature and even with an air temperature as cold as 1/40 eV, deionization by these reactions in 0.35 Torr air is slow enough that N^+ ions would persist in the afterglow for several hundred ns, in agreement with the observations.

Framing photographs are shown in Figures 15 and 16. Each frame is integrated over 10 ns and the interval between frames is 40 ns. The sequence in which the frames were taken alternates between the lower and upper rows, left to right (in the N shaped sequence characteristic of the Imacon camera). These photographs clearly show the formation of the feather patterns seen earlier in the open shutter photographs (Fig. 6). The feathering appears to occur at the end of the beam (Frames 3 and 4), possibly as the fields (and thus E/p) are rapidly changing. However, the feathering may be present at all times and masked by other intense emissions. As the region of emission collapses at the end of the beam, the vertices of the feathers remain in the same location and continue to radiate for long times (the last frame is ~ 600 ns in Fig. 16, and ~ 700 ns in Fig. 17). The integration of the radiation from these vertices is responsible for the intense exposure previously seen near the axis of the open shutter pictures. Thus, the "hot spots" previously seen in open shutter photographs do not result from extremely intense emission for a short duration, but rather are the result of long time exposure compared with the remainder of the emission.

In summary, from the spectral measurements we have identified the observed red emission to be atomic oxygen at 6157Å, we have identified a large number of N_2 , N_2^+ and N^+ emissions, and we have shown the

atomic line radiation to emanate from a region of limited radial extent. In the streak photographs we have seen some results of the magnetic field collapse at the end of the beam. We have observed that the molecular emissions temporally track the beam and that the atomic emission persists at late times, after the beam has passed. The framing photos give the first hint of the feathering process, show the collapse of the field and radiating volume, and the long time history of the atomic emissions. Further development of these techniques (i.e., time-resolved spectroscopy) holds great promise for providing much information on beam-air chemistry (and hence conductivity) and on basic beam parameters.

This research was sponsored by the Air Force Office of Scientific Research (AFSC) under contract F49620-81-C-0016. The authors wish to acknowledge the assistance of Winston Bostick in performing these experiments. Professor Bostick was a senior research physicist in the University Residency Program sponsored by the Air Force Office of Scientific Research under IPA-905-79-01016C. Finally, the authors are deeply indebted to the following members of the Dynamic Testing Division (M Division) at Los Alamos National Laboratory for the time-resolved photography of the FX-100 propagation experiments: Lee Builta, Dave Moir, and Steve Schmidt. Starke.

TABLE 1. FX-100 BEAM PROPAGATION EXPERIMENT PARAMETERS

Maximum Beam Energy,	$E_b = 1.5 - 2.0 \text{ MeV}$
Maximum Beam Current,	$I_b = 35 - 40 \text{ kA}$
Beam Pulse Duration,	$\Delta t = 120 \text{ ns}$
Beam 1/e-radius at injection,	$r_{bo} = 3 \text{ cm}$
Propagation Chamber Radius,	$R_w = 10 \text{ cm}$
Observation Port Position,	$z_o = 4.5 \text{ m}$
Air Pressure,	$p_o = 0.1 - 20 \text{ Torr}$

TABLE 2. IDENTIFICATION OF OBSERVED LINES AND BANDS.

WAVELENGTH Å	ATOM/MOLECULE	TRANSITION (band) (v', v'')
3755	N ₂	(2+) (1,3)
3805	N ₂	(2+) (0,2)
3858	N ₂	(2+) (4,7)
3884	N ₂ ⁺	(1-) (1,1)
3914	N ₂ ⁺	(1-) (0,0)
3943	N ₂	(2+) (2,5)
3998	N ₂	(2+) (1,4)
4059	N ₂	(2+) (0,3)
4095	N ₂	(2+) (4,8)
4142	N ₂	(2+) (3,7)
4167	N ₂ ⁺	(1-) (3,4)
4200	N ₂	(2+) (2,6)
4236	N ₂ ⁺	(1-) (1,2)
4270	N ₂	(2+) (1,5)
4278	N ₂ ⁺	(1-) (0,1)
4344	N ₂	(2+) (0,4)
4417	N ₂	(2+) (3,8)
4433	N ⁺	3d 3p ^o -4f D(5/2)
4447	N ⁺	3p 3D - 3d 3D ^o
4490	N ₂	(2+) (2,7)
4530	N ⁺	3d 1F - 4f G(9/2)
4554	N ₂ ⁺	(1-) (3,5)
4574	N ₂	(2+) (1,6)
4600	N ₂ ⁺	(1-) (2,4)
4607	N ⁺	3s 3p ^o - 3p 3p
4614	N ⁺	3s 3p ^o - 3p 3p
4621	N ⁺	3s 3p ^o - 3p 3p
4630	N ⁺	3s 3p ^o - 3p 3p
4643	N ⁺	3s 3p ^o - 3p 3p
4652	N ₂ ⁺	(1-) (1,3)
4678	N ⁺	3d 1p ^o - 4f D(3/2)
4709	N ₂ ⁺	(1-) (0,2)
4803	N ⁺	3p 3D - 3d 3D ^o
4860	N ⁺	3p 3D - 3d 3D ^o
5001	N ⁺	3p 3D - 3d 3F ^o
5005	N ⁺	3s 5p - 3p 5p ^o
		3p 3D - 3d 3F ^o
5667	N ⁺	3s 3p - 3p 3D
5680	N ⁺	3s 3p - 3p 3D
5686	N ⁺	3s 3p - 3p 3D
5711	N ⁺	3s 3p - 3p 3D
6157	O	3p 5p - 4d 5D ^o

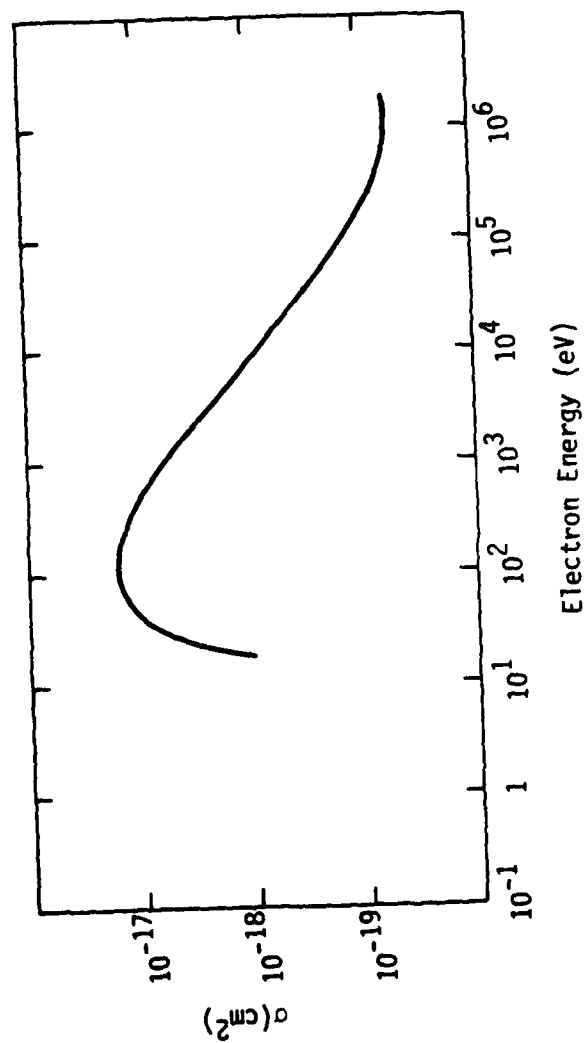


Figure 1. Excitation cross section for $\text{N}_2^+(1-)$.
(Data from Ref. 8)

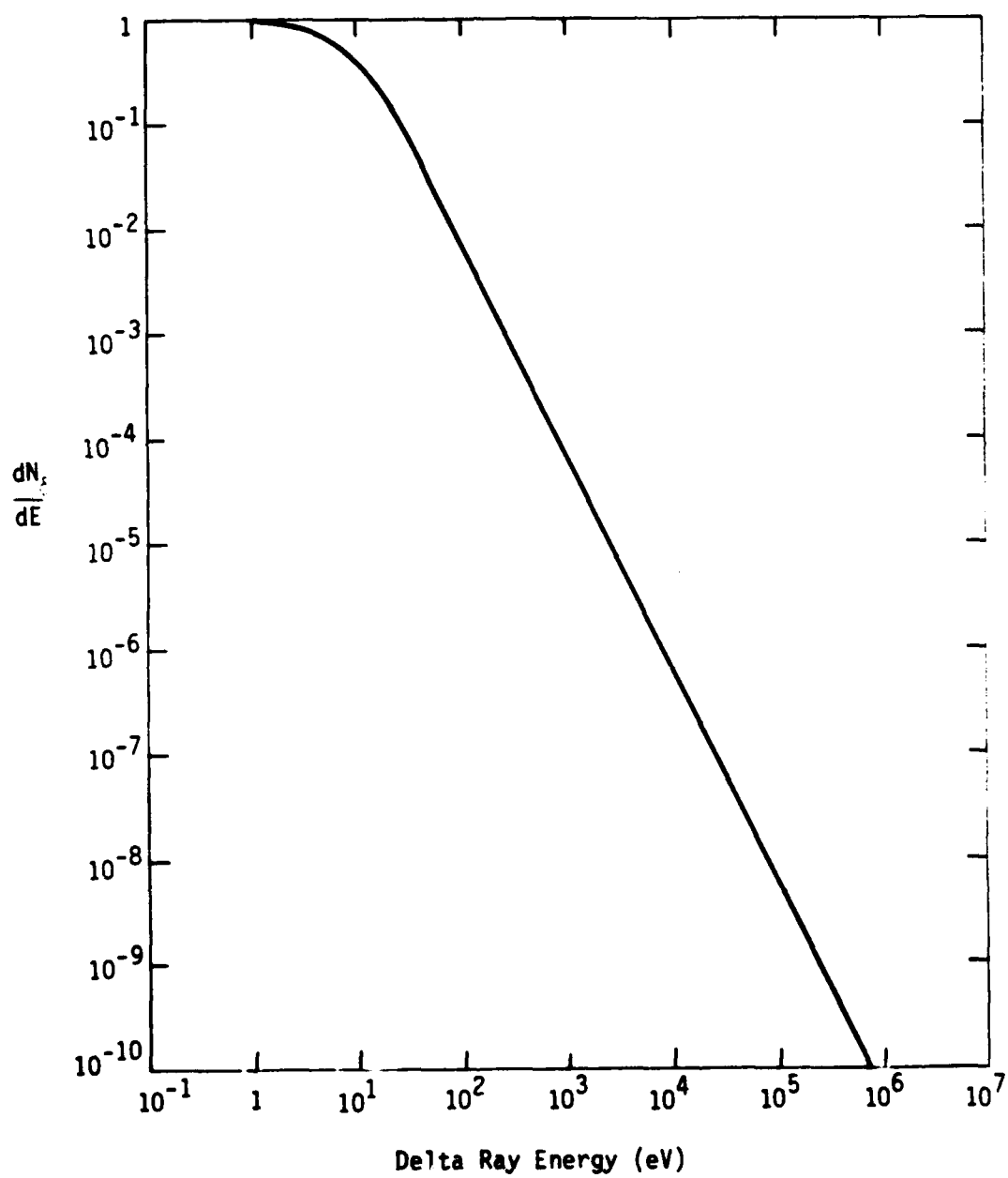


Figure 2. Distribution of delta rays with energy.
(Calculated for $\gamma \geq 4$)

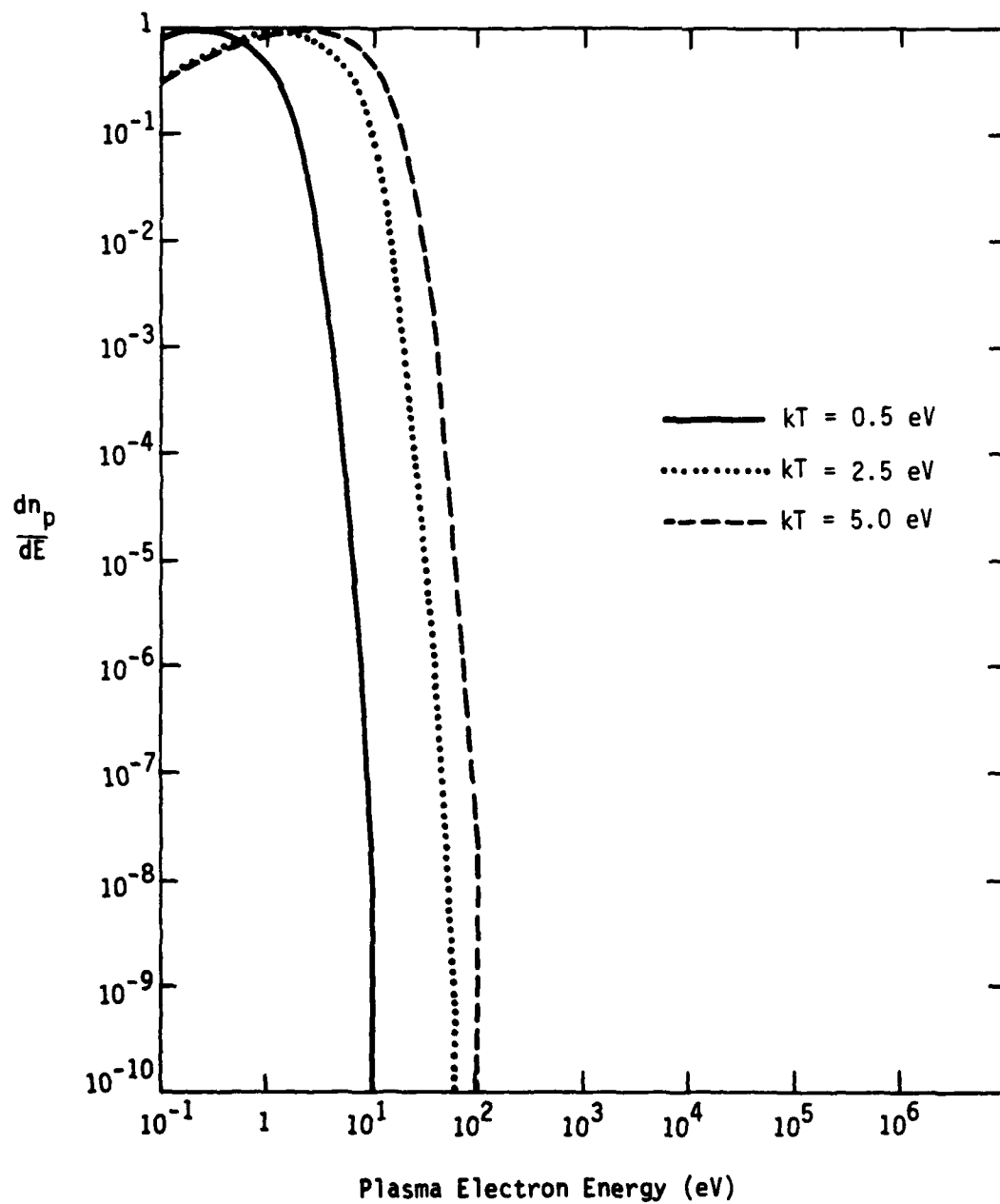


Figure 3. Distribution of plasma electrons with energy for three Maxwellian temperature distributions.

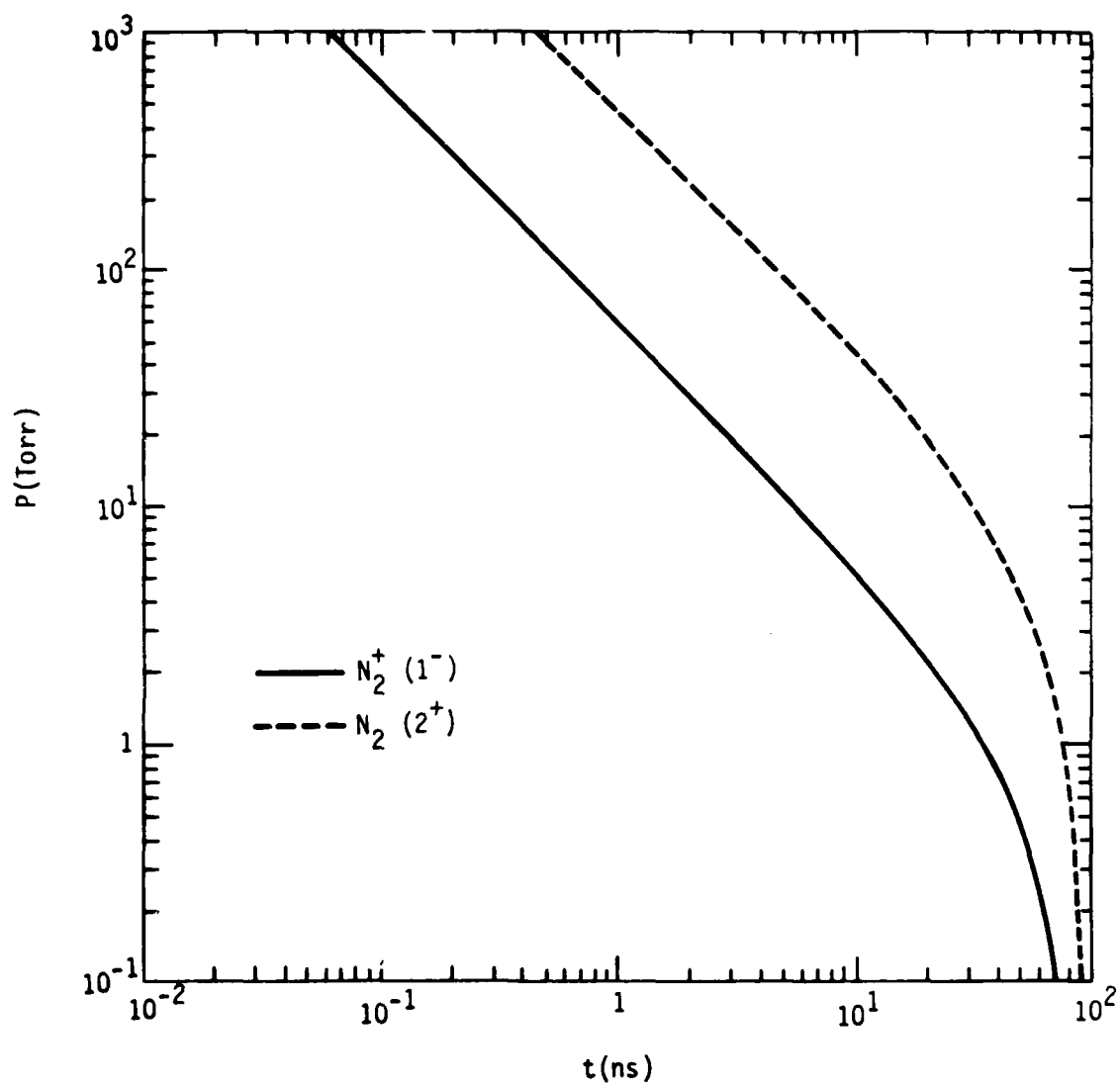


Figure 4. Pressure required for a given response time for two nitrogen bands.

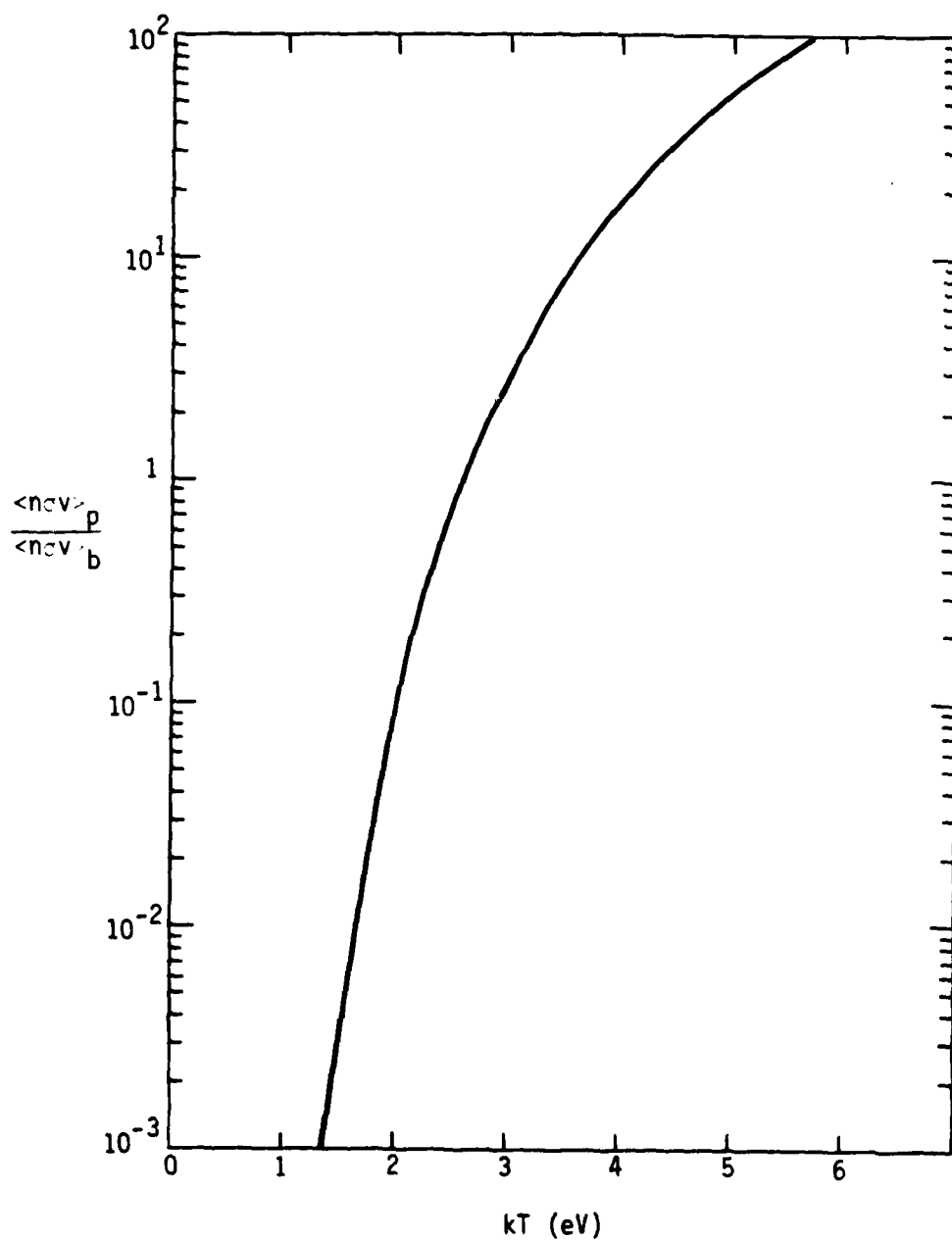
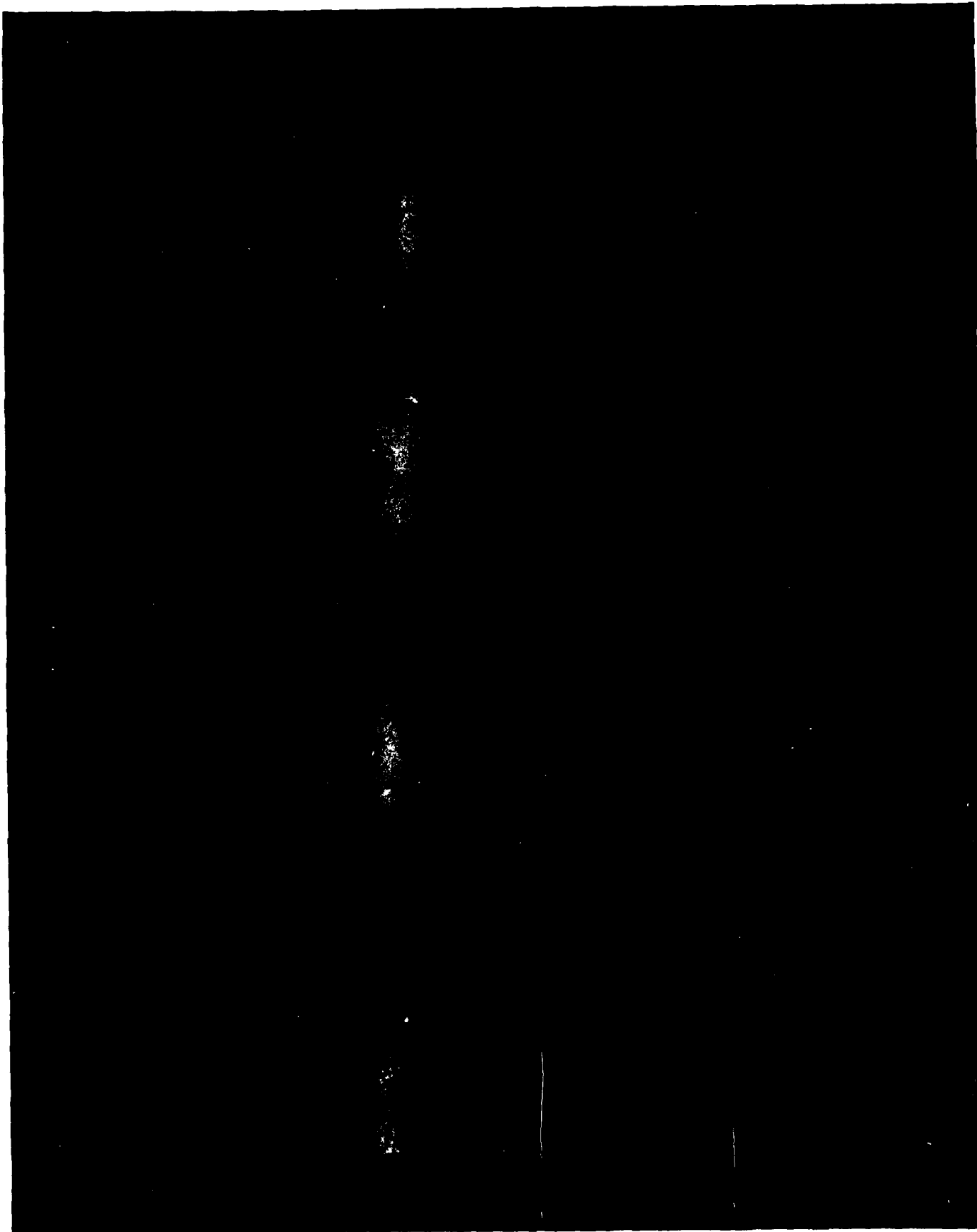


Figure 5. Ratio of $N_2^+(1^-)$ excitation caused by plasma electrons to beam electrons as a function of plasma temperature, assuming $n_p/n_b = 10^3$ and $E_b = 1.5$ MeV.

Figure 6. Open shutter photograph of FX-100 beam showing feathering.
(Beam propagates from right to left.)



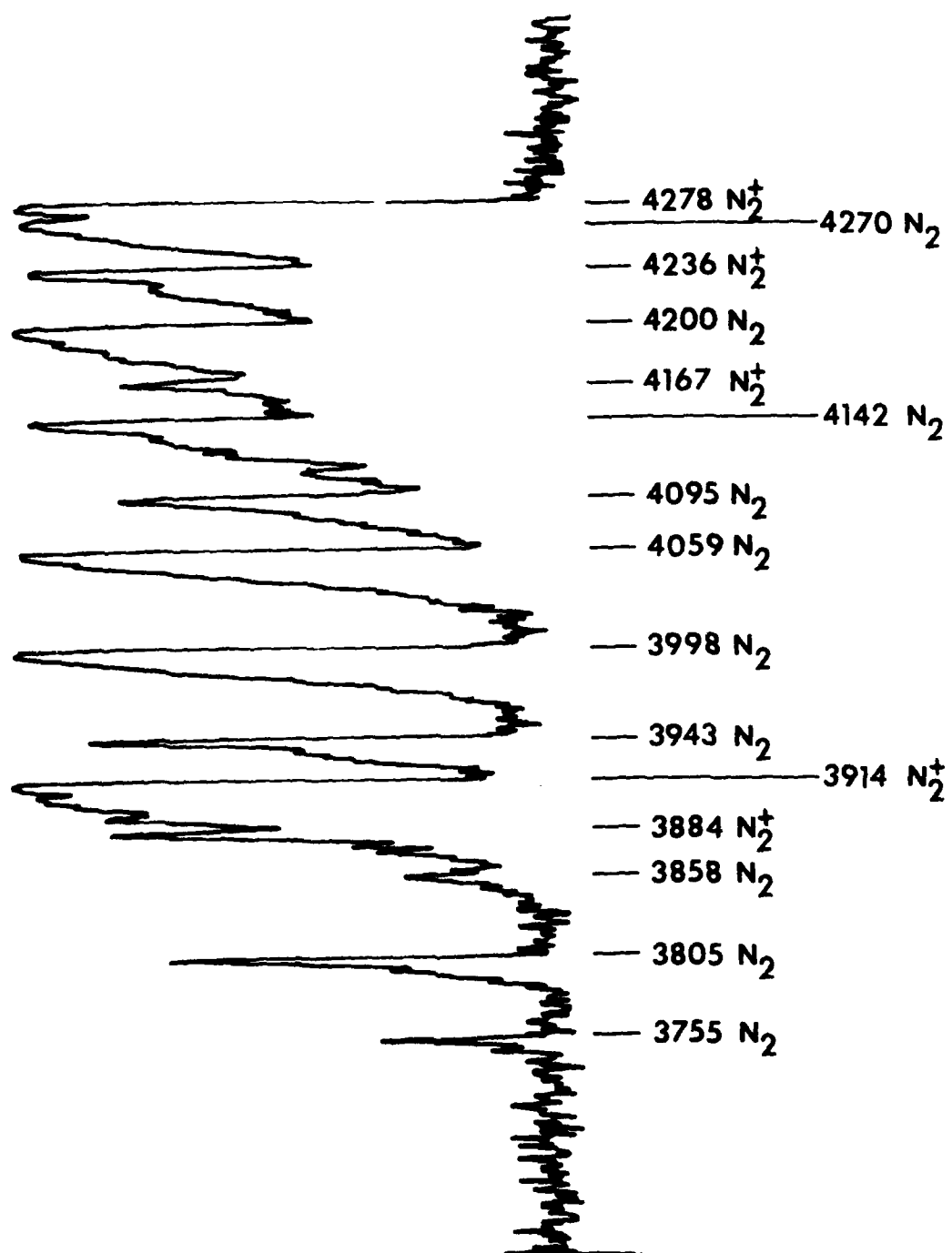


Figure 7. Densitometer scan of FX-100 spectra.

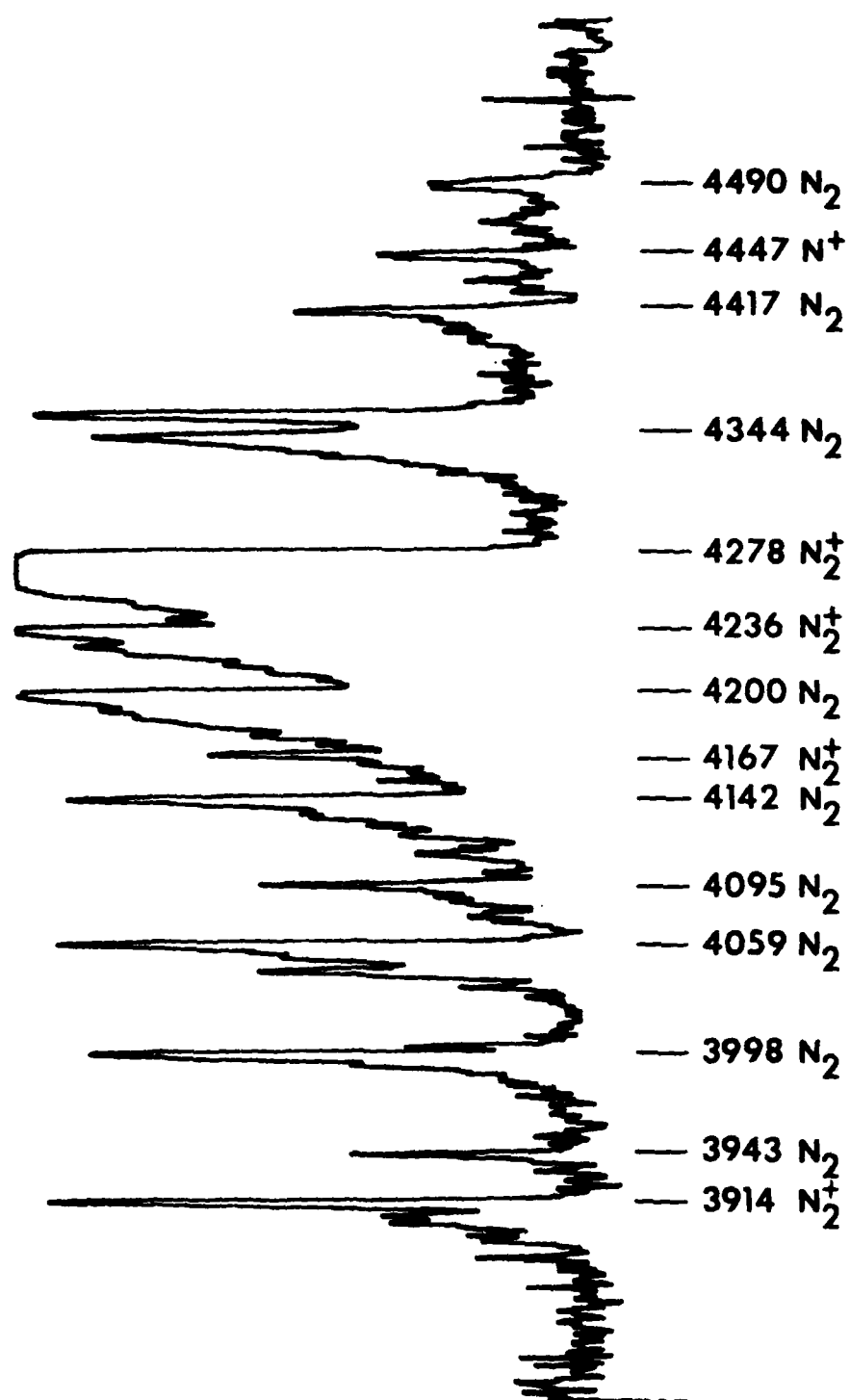


Figure 8. Densitometer scan of FX-100 spectra.

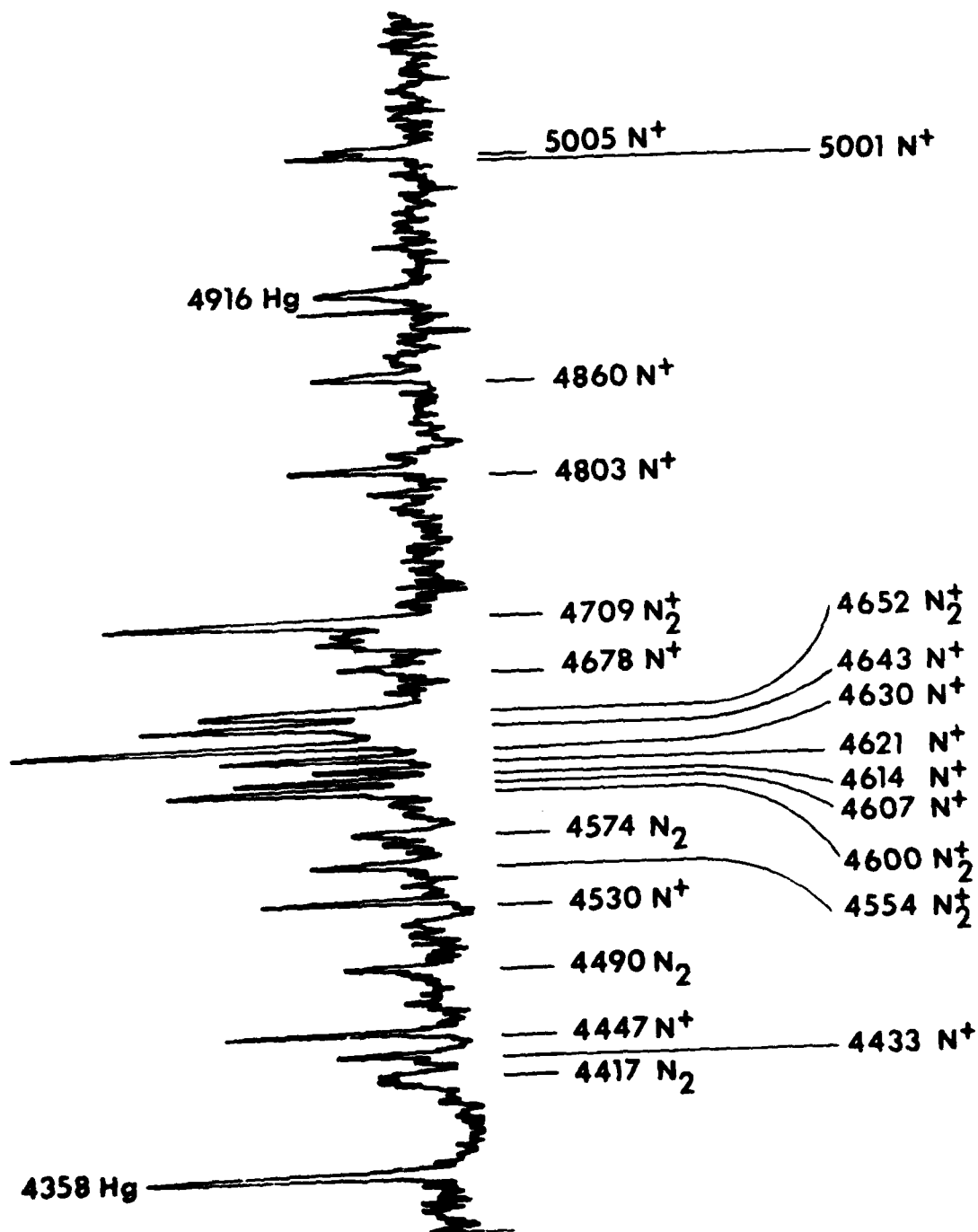


Figure 9. Densitometer scan of FX-100 spectra.

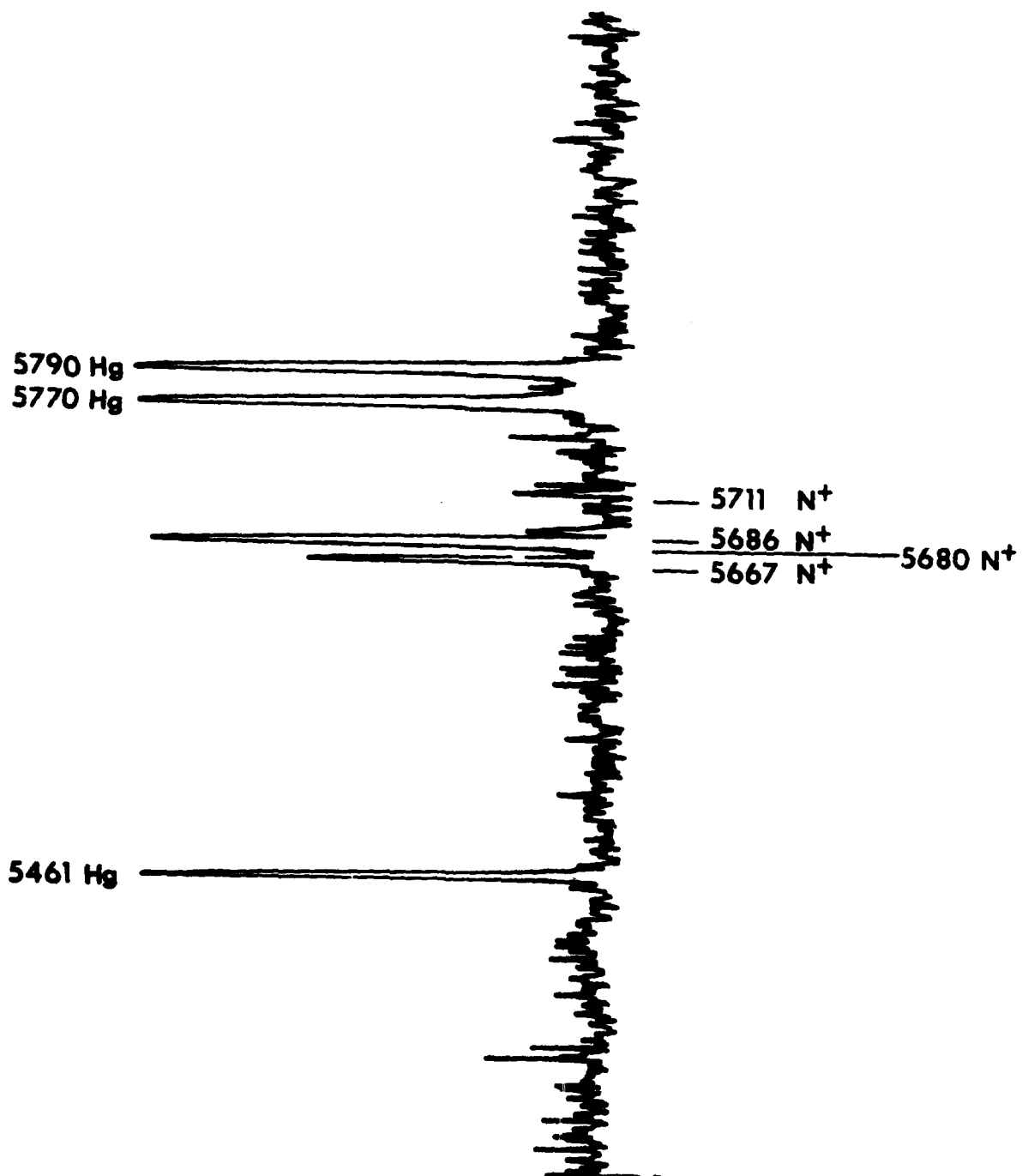


Figure 10. Densitometer scan of FX-100 spectra.

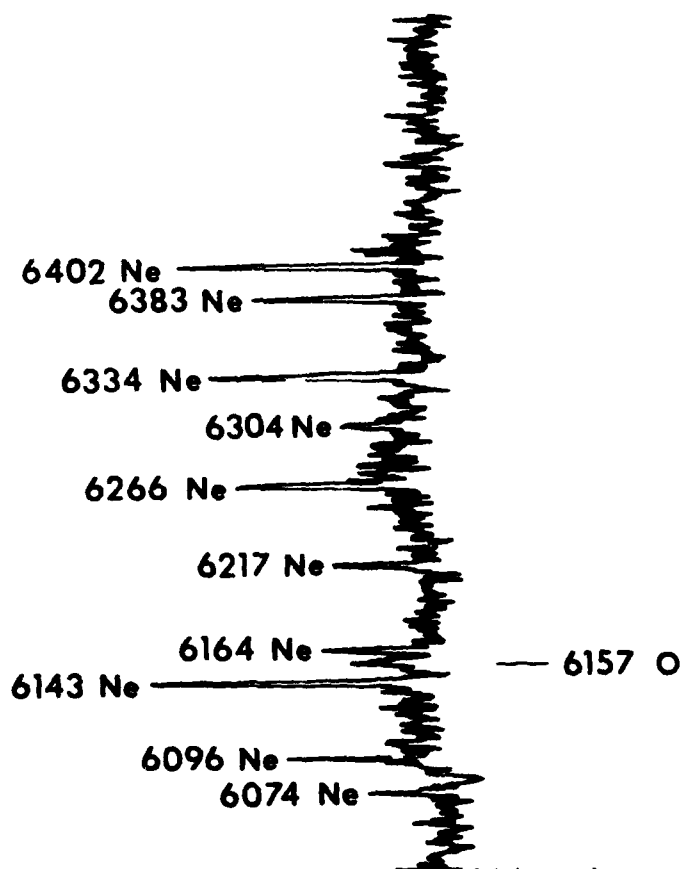


Figure 11. Densitometer scan of FX-100 spectra.

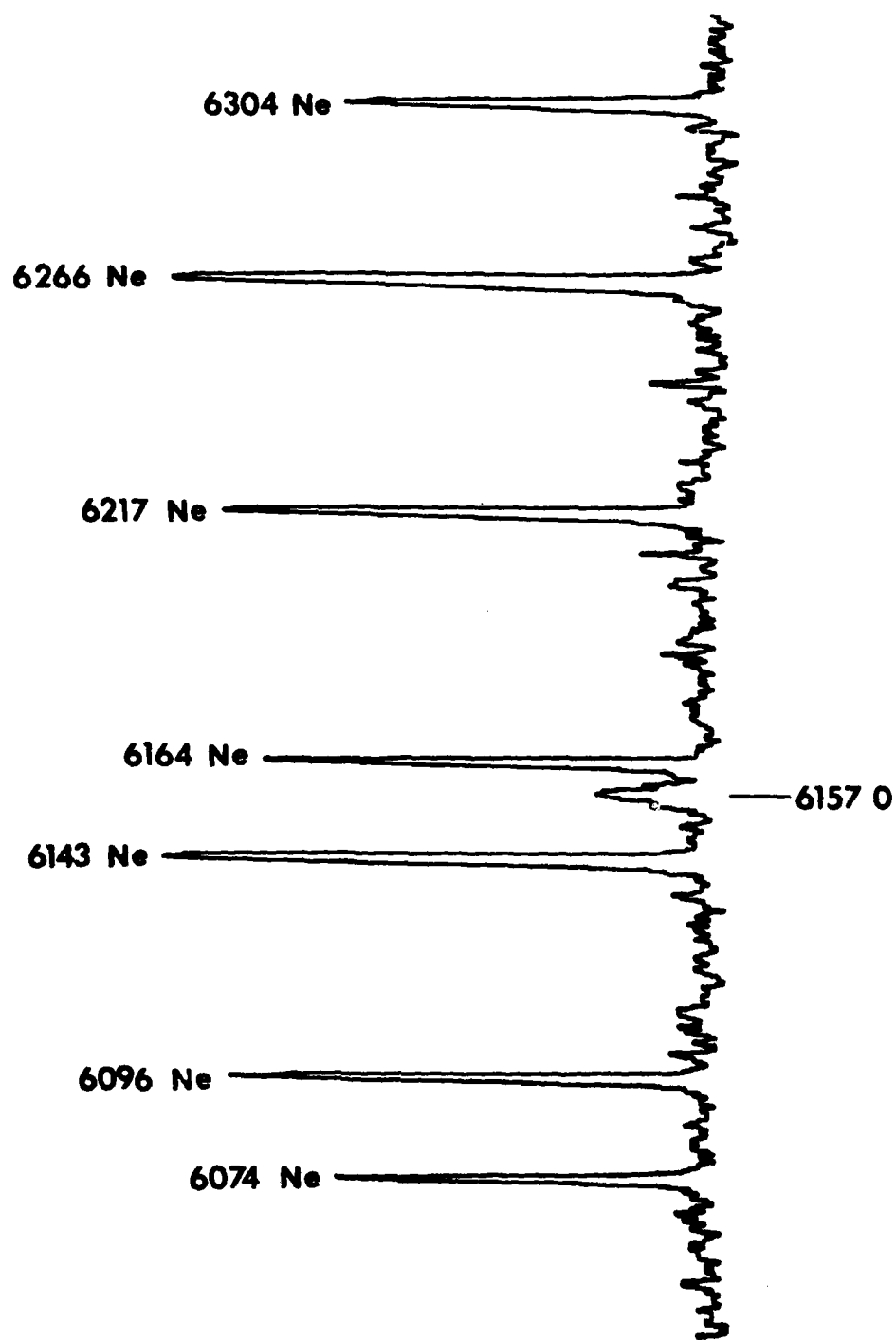


Figure 12. Detailed densitometer scan of oxygen line.

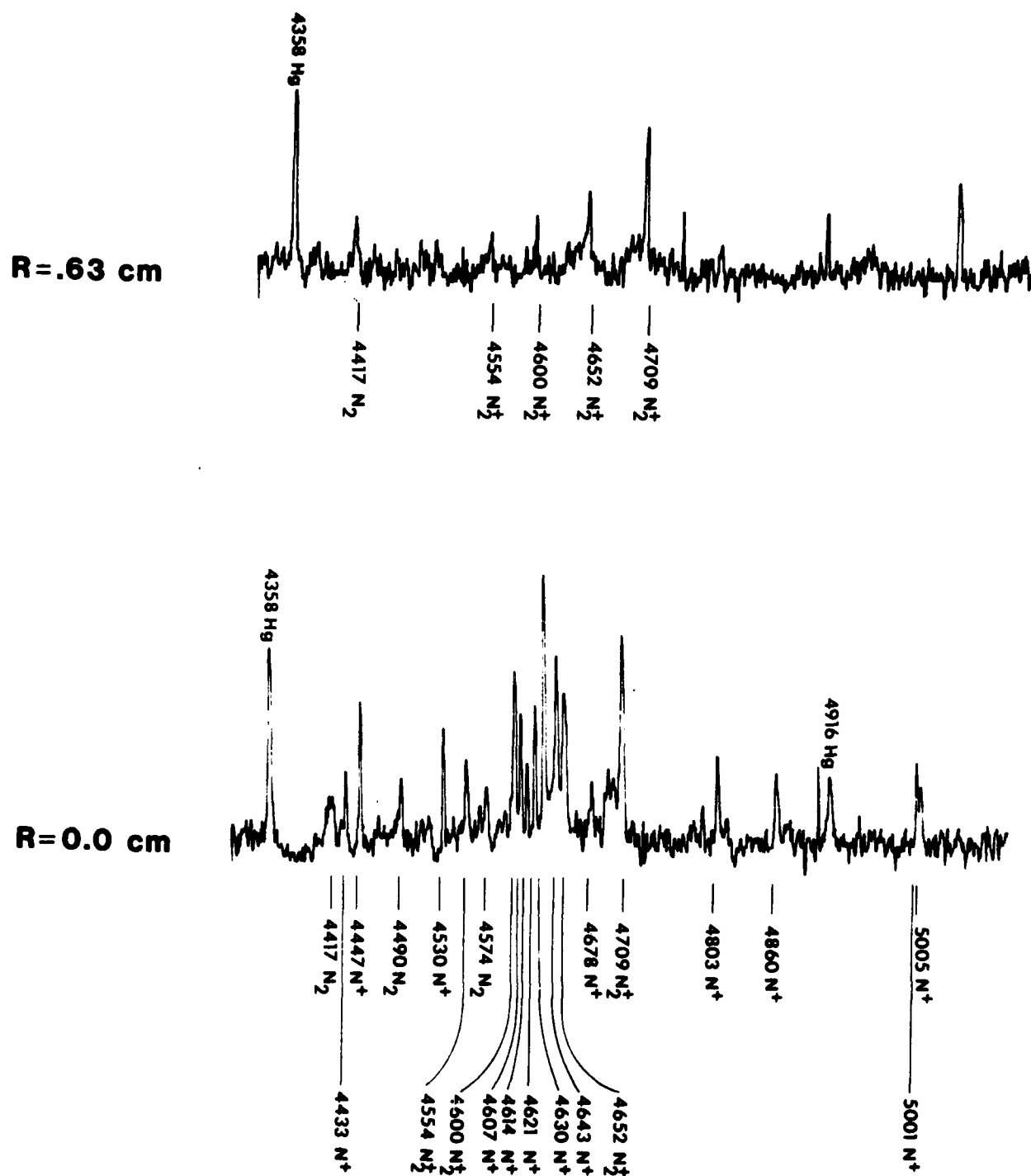


Figure 13. Densitometer scan of FX-100 spectra off axis and on axis.

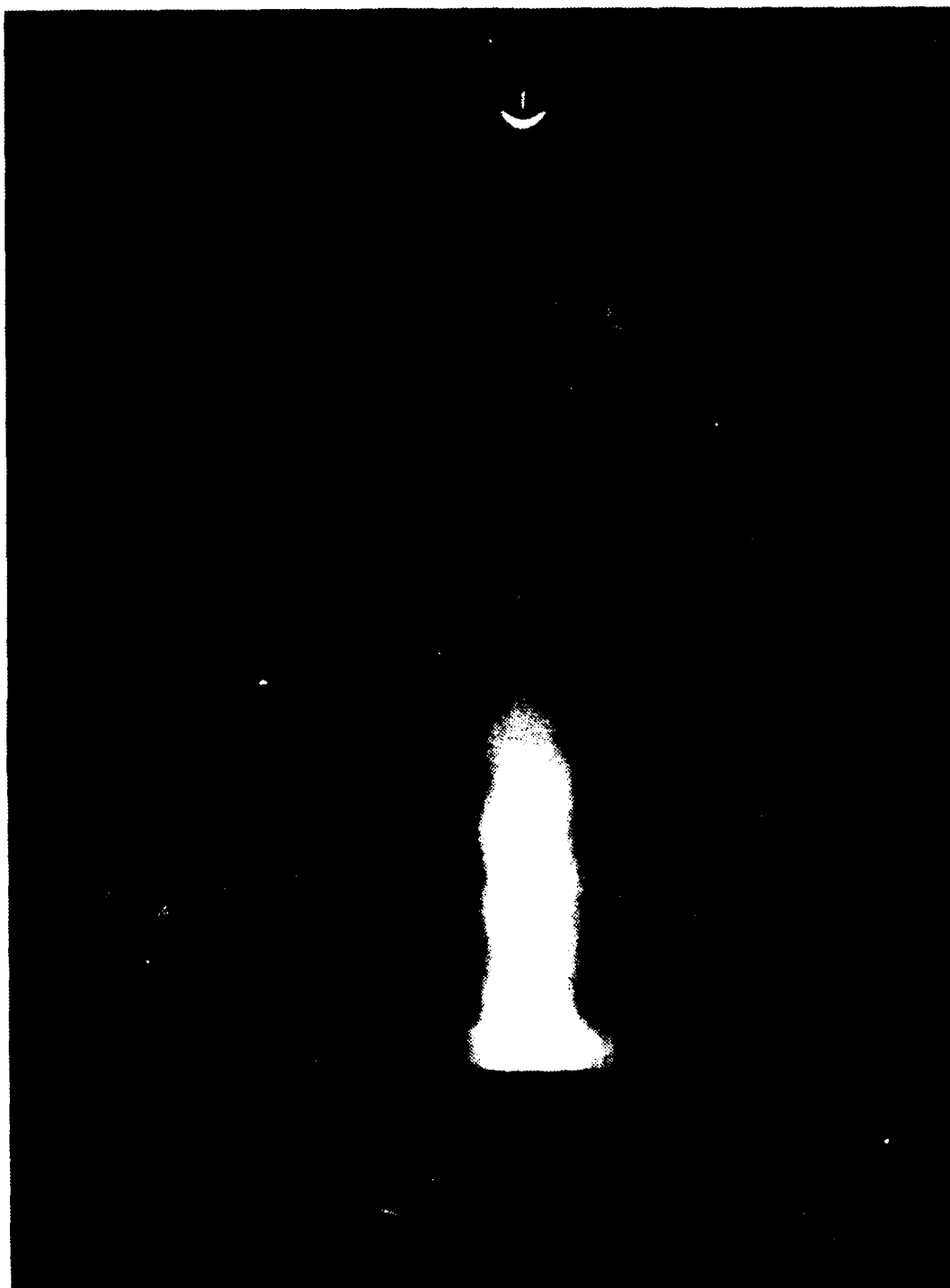


Figure 14. Streak photograph of beam at .35 Torr.

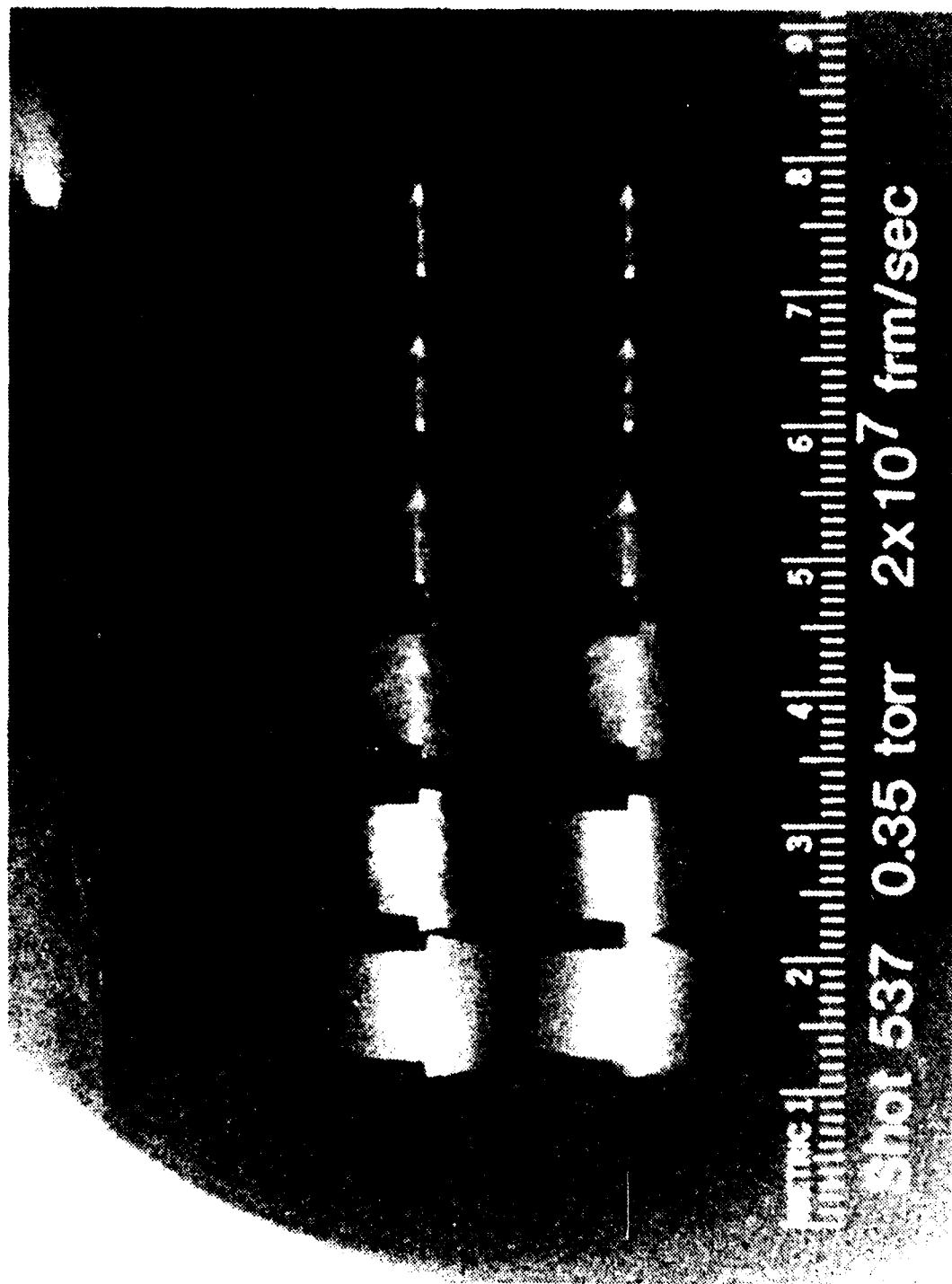


Figure 15. Framing photograph of FX-100 beam at .35 Torr.

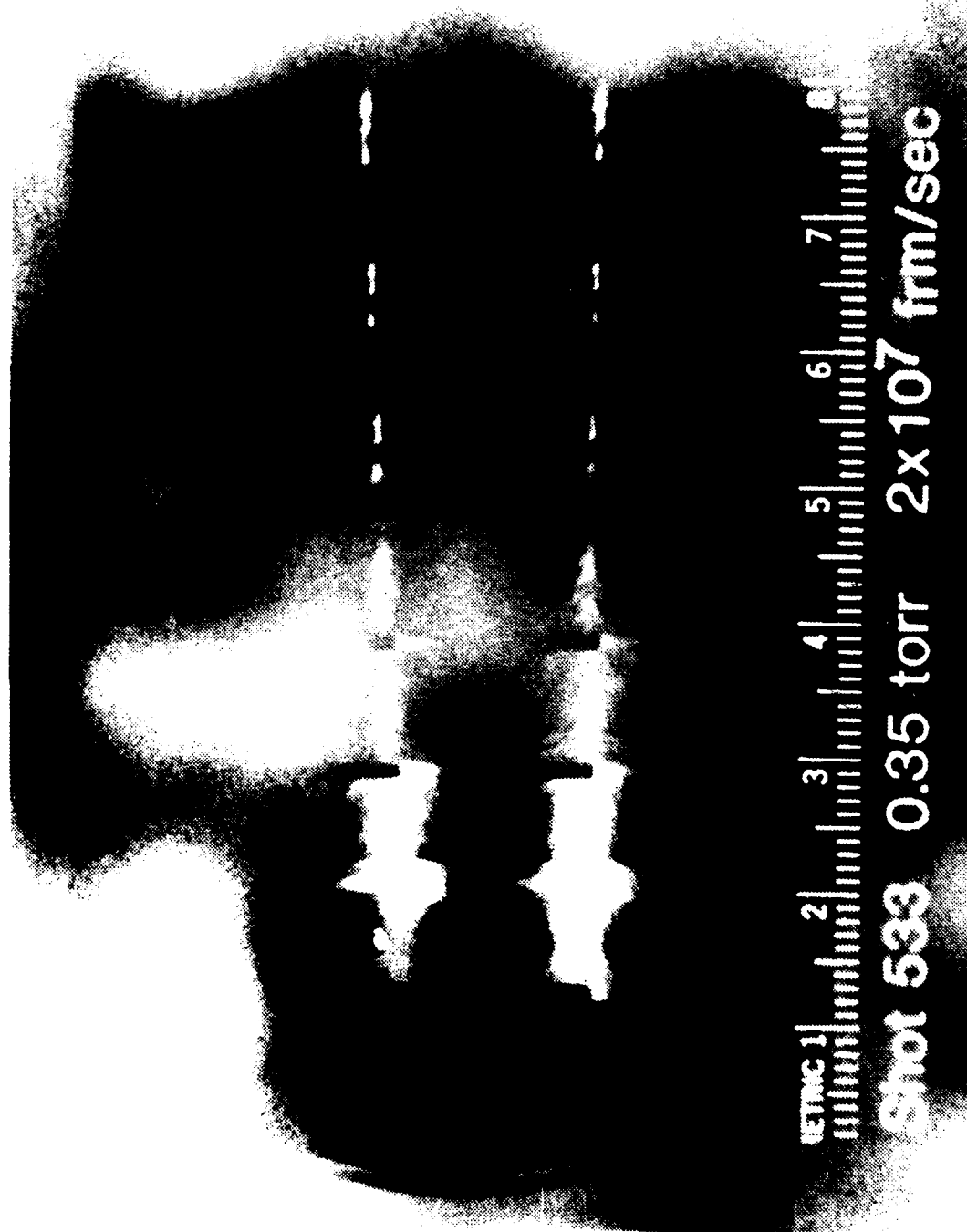


Figure 16. Framing photograph of FX-100 beam at .35 Torr.

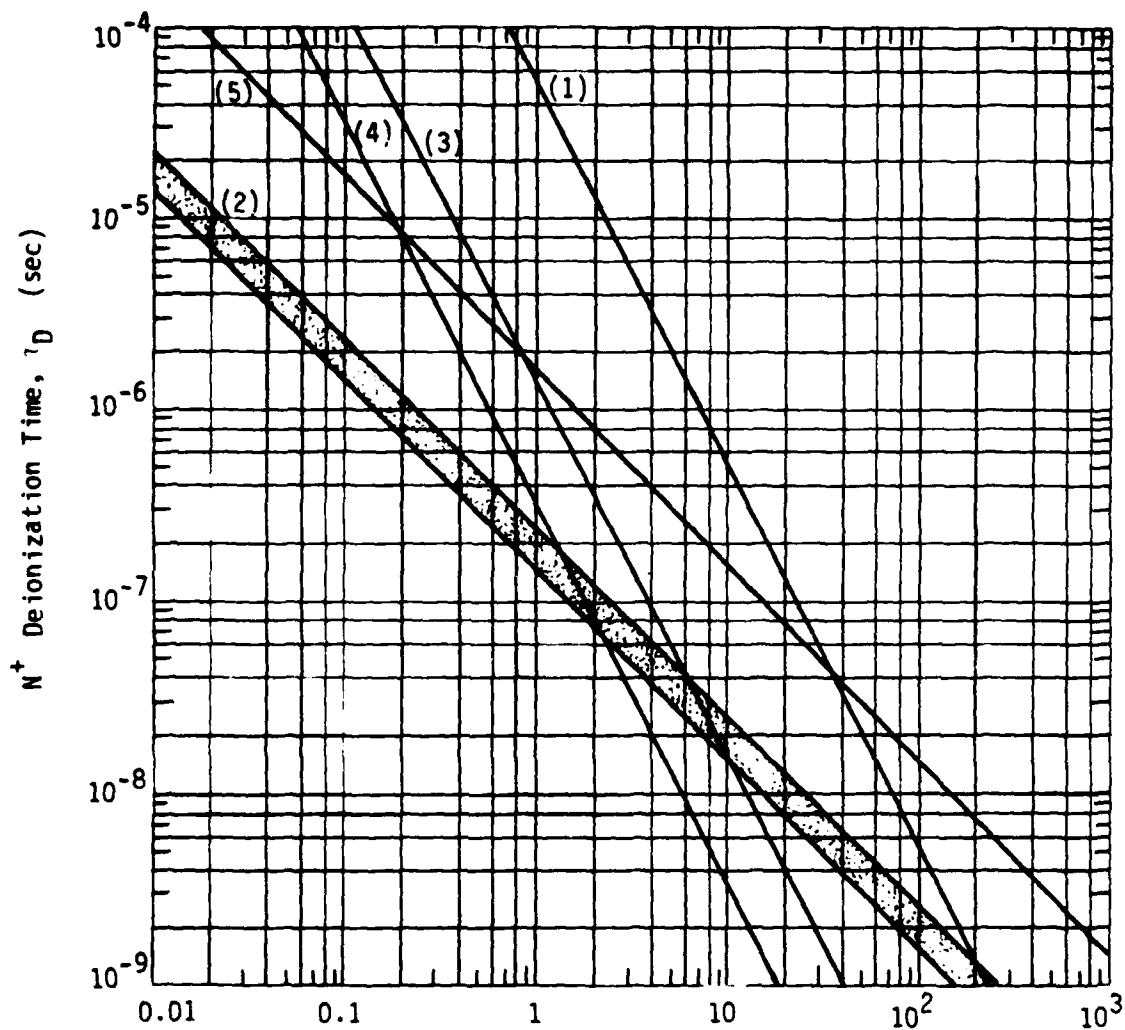
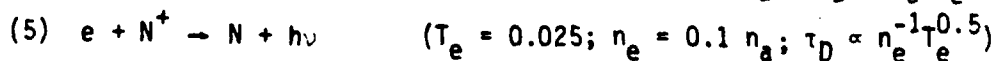
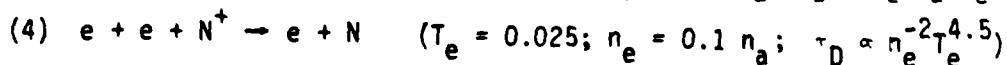
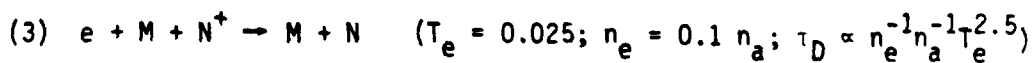
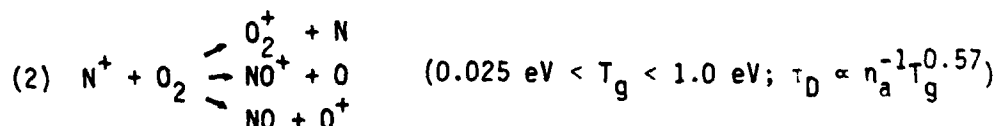
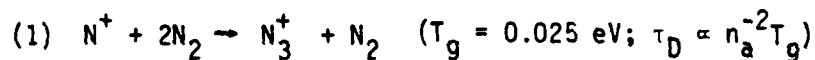


Figure 17.

Persistence of N^+ ions in air resulting from the following deionization reactions:



REFERENCES

1. T. J. Fessenden, R. J. Briggs, J. C. Clark, E. J. Lauer, and D. O. Trimble, Lawrence Livermore National Laboratory Report UCID-17840 (1978).
2. R. B. Miller, Sandia National Laboratory Report SAND-79-2129 (1979).
3. R. B. Fiorito, E. W. Fordham, J. R. Greig, R. E. Pechacek, J. D. Sethian, R. Fernsler, and J. Halle, Naval Research Laboratory Memorandum Report 4557, (1981).
4. R. M. Hill, K. Y. Tang, B. E. Perry, D. J. Eckstrom, and D. L. Huestis, SRI International Report MP80-41 (1980).
5. A. M. Frank, S. S. Yu, and J. M. Masmitsu, Lawrence Livermore National Laboratory Report (1982).
6. T. J. Fessenden, W. L. Atkinson, W. A. Barletta, J. F. Campbell, J. C. Clark, L. D. Clendenen, R. B. Fiorito, A. M. Frank, F. D. Lee, H. A. Koehler, and K. W. Struve, Lawrence Livermore National Laboratory Report UCID-19245 (1981).
7. G. Davidson and R. O'Neil, J. Chem. Phys. 41, 3946 (1964).
8. M. N. Hirsch, E. Poss, and P. N. Eisner, Phys. Rev. A1, 1615 (1970).
9. H. A. Bethe and J. Ashkin, in Experimental Nuclear Physics, Vol. 1, ed. by E. Segre, (1953).
10. P. Millet, Y. Salamero, H. Brunet, J. Galy, D. Blane, and J. L. Teyssier, J. Chem. Phys. 58, 5893 (1973).
11. G. A. Baraff and S. J. Buchsbaum, Phys. Rev. 130, 1007 (1963).
12. G. W. Sutter and A. Sherman, Engineering Magnetohydrodynamics, (McGraw-Hill, N.Y., 1965), pp. 125-210.
13. S. Brown, Basic Data of Plasma Physics, (Wiley, N.Y. 1959).
14. A. W. Ali, Naval Research Laboratory Memorandum Report 4619, (1981) and references therein.
15. R. W. P. McWhirter, in Plasma Diagnostic Techniques, ed. by R. H. Huddleston and S. L. Leonard, (Academic Press, N.Y., 1965), pp. 208-214 and references therein.

ENV